High resolution imaging observations of exoplanet host stars

Kaltrina Kajtazi

Lund Observatory
Lund University

2020-EXA167

Degree project of 15 higher education credits
June 2020

Supervisor: Sofia Feltzing

Lund Observatory
Box 43
SE-221 00 Lund
Sweden

High resolution imaging of exoplanet host stars

Bachelor Thesis

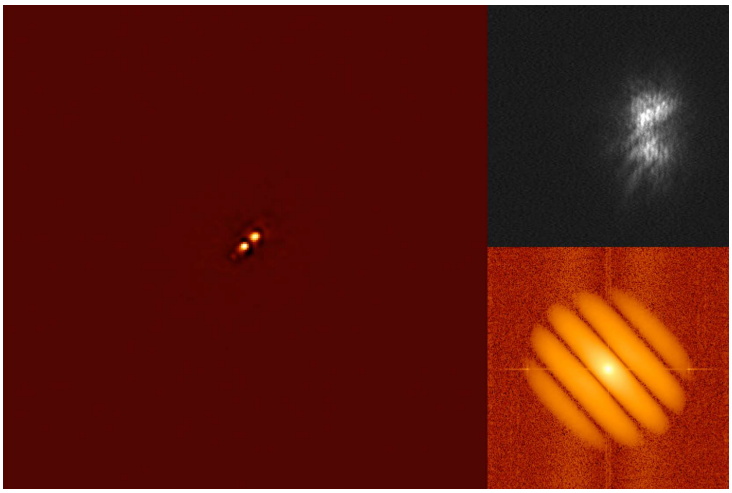

Source: Scott et al. (2018)

Author: Kaltrina Kajtazi

Supervisor: Rachel A. Matson

Co-Supervisor: Sofia Feltzing and Dainis Dravins

Lund University

NASA Ames Research Center

June 11, 2020

Abstract

This is a thesis project, analysing data from high-resolution imaging observations, specifically speckle imaging, as a follow up study of exoplanet host stars observed with K2, the second operational phase of the space telescope Kepler. The project was accomplished at NASA Ames research center under the guidance of Rachel A. Matson, during an internship in collaboration with the Swedish National Space Agency. The speckle imaging data is from observations with the instruments DSSI and NESSI conducted at the twin telescopes Gemini, in Chile and Hawaii, and WIYN in Arizona. The main goal of these observations is to identify possible binary or multiple stellar systems. Scientists have long been interested in binary systems mostly because they are not well understood and are a good laboratory for interesting phenomena such as planet formation. In this sample there are only binaries.

With speckle imaging we can resolve stellar companions with angular separation less than $1.2''$, by taking 40ms images. From these images we can resolve all the stars and extract the following parameters; the position angle, the magnitude difference and the angular separation between the two stars. These parameters are then used to estimate properties for each system studied in this project, aiming to better understand properties of binary stellar systems in our Galaxy.

In this project I have determined the following properties; The physical separation, the masses of the individual stars and the orbital period. Out of the total 100 potential stellar binaries 26 are most likely bound. The stars in the sample have masses in the range $0.2 - 2M_{\odot}$. The systems consist of components that are usually far from each other, up to 850AU and the closest pair at about 7AU. The orbital period ranges from 15 to over 10000 years, most of them being within 3000 years. These calculations are at best good estimates of reality. However, this sample still provides a worthy sample of stellar binaries to study further. The results were also compared in detail to a study of the stellar binaries in the solar neighbourhood, (Raghavan et al., 2010), looking into similarities and differences. It was found that the distributions and trends of the properties agree well with Raghavan et al. (2010) and other work.

I find that in my sample the fraction of detected companions is roughly 14%. Because the telescopes have different detection limits the observations were also separated according to telescope; the fraction for Gemini is 15% and for WIYN 8%.

Populärvetenskaplig beskrivning

Stjärnor sägs vara astronomins tidskapsel, genom att studera stjärnor kan vi bättre förstå många fenomen. Stjärnor är en viktig del av vårt universum från det att de skapas till det att de dör. De berikar vårt universum med olika grundämnen som krävs för att planeter ska bildas och för att liv ska uppstå. Det verkar då självklart varför man vill undersöka och förstå alla aspekter kring stjärnbildning, stjärnornas livsutveckling och olika stjärnsystem.

Stjärnor bildas från gasmoln, som består av mestadels väte och helium. Ur ett sådant moln kan många stjärnor i olika storlekar bildas. I den enklaste mening är en stjärna en gas boll, som lyser tack vare förbränning av väte till helium i dess kärna. Under en stjärnas liv förbränner den tyngre och tyngre ämnen hela vägen till järn innan den dör. Exakt hur en stjärna dör ser olika ut beroende på storlek, men en sak gemensamt är att det bildas grundämnen tyngre än järn under den stunden.

Att förstå dessa processer är viktigt för att kunna förstå andra relaterade fenomen så som olika stjärnsystem och planetformation. Till exempel, är det vanligare att stjärnor bildas i par eller ensamma? Den här frågan har länge studerats främst i solens närhet, då det är enklare att observera och se båda stjärnorna i ett stjärnpar, binärt stjärnsystem, som enskilda stjärnor när de är närmare oss. Det dröjde fram till 70-talet innan en observations metod som kunde särskilja båda stjärnorna i kompakta stjärnpar längre bort kom till. Denna metod kallas "Speckle interfotometri", den bygger på att fotografera stjärnsystem med hög optisk upplösning och kort exponeringstid. Från dessa bilder kan man få ut magnitudsskillnaden hos stjärnorna i det dubbla stjärnsystemet, positionsvinkeln för den sekundära stjärnan i jämförelse till huvudstjärnan och vinkelavståndet mellan dem. Idag kan man med ett stort teleskop särskilja båda stjärnorna i ett stjärnpar som är så när som 1.2 bågsekunder ifrån varandra.

I detta arbete har data från speckle interfotometri analyserats. Med syftet att hitta följande egenskaper från de observationer där en stjärngranne till huvudstjärnan har hittats; fysiskt avstånd mellan stjärnorna i systemet, massan hos varje stjärna och omloppstiden. Resultatet från dessa beräkningar kan användas för att förstå vad det finns för slags binära stjärnsystem i Vintergatan, hur många binära stjärnsystem det finns procentuellt och om de är lika de binära stjärnsystem i närheten av Solen.

Acknowledgements

The writer of this thesis gives big credit to the Swedish national space agency for their work and established opportunities for students to gain experience in their field through different internships such as the one at NASA. Where I completed this project in wonderful supervision of Rachel Matson, a scientist at NASA, whom I am very grateful to. She was a great help, gave clear instructions and room to test the knowledge I have gained in my studies by letting me try to solve problems myself before answering any questions thoroughly. From this experience I have learned many new things about speckle imaging and other parts of a science carrier, such as improved skills in Python and information research.

Another thank you goes to Steve B. Howell, chief of division at NASA Ames and head of the Speckle group, for all his help, support and ideas/tips for the project. Furthermore, I would like to thank my thesis supervisors at Lund university professor Sofia Feltzing and Dainis Dravins, for their help to proof read this report and tips until the report was satisfying.

I also wish to thank my family for their support during application for and during the internship and thesis writing. Lastly, thank you to the four people that wrote amazing recommendation letters for me to use in my application for the NASA internship.

Contents

List of Figures

List of Tables

1 Introduction

The existence of stellar binary systems has long been known. In fact it is believed that most stars are not born single. Rigorous statistical studies of the solar neighbourhood[1] have investigated this idea to give a better picture of the fraction of stellar binaries. The percentage of stellar binaries in the solar neighbourhood is $40 - 50\%$, which is consistent with studies of samples of stars outside the solar neighbourhood as well (Raghavan et al., 2010; Matson et al., 2018). This will be shown to be true for the sample studied in this project.

The definition of a stellar binary system is as follows; two stars that are bound to each other through gravity and orbit around a common center of mass. Stellar binaries as those detected in this sample usually consist of a more massive, brighter target star, which is easier to detect and a smaller, less bright companion. Moreover, it is worth noting that there are many types of binary systems, in this project we are only interested in binary systems with members that are still on the main sequence and are believed to have planets. For reference other binary systems can consist of stars in other stages of their evolution such as neutron stars. All of these are interesting in different ways and are laboratories for different aspects of fundamental astrophysics. It is thus clear that the interest for all known types of binaries has long been thriving and is well founded, it is indeed a part of the universe which needs more exploration and understanding.

Binary systems of stars on the main sequence became more important to pay attention to from the moment we started searching and detecting planets outside of our solar system. Because there are many questions to be answered about planet formation in general, but especially planet formation in stellar binary systems which we know little about. By studies of stellar binaries such as this one, we want to, amongst other aspects, better understand the main properties of the systems such as the orbital period and the stellar masses, to see if trends that have been proven to hold for stellar binaries without known planets in the solar neighbourhood are also visible in stellar binaries with planets in other parts of the Galaxy.

More specific examples where exoplanet[2] follow up programs such as speckle imaging have been useful are the following: Identifying false positives, which refers to stellar companions (especially eclipsing[3] ones) that in planet detection methods, such as the transit method[4], mimic a planet. A companion can as it moves along its orbit give rise to

1 In the papers mentioned and compared to in this thesis, the solar neighbourhood is defined to be out to 25 pc from the Sun.

2 Exoplanet is the term assigned to a planet not in the solar system.

3 For eclipsing binaries the orbital plane that they move in, is close to the line of sight. Therefore the stars obscure each other as they move in their orbit.

4 The transit method is based on continuous measure of light from a star of interest. The measurements are plotted as a so called light curve, presenting the change in brightness of the star over time. Decrease in the brightness is called a dip.

periodic dips in the light curve as it passes in front of the observed star in the same way as a planet would. By identifying such companions, scientists will be able to distinguish real planets from false positives in their data. Moreover, detecting companions and knowing their properties can help to correct the planet radius of any planet in a stellar binary system by using relation formulas such as those in Teske et al. (2018). The planet radius is underestimated due to that the flux from the companion is collected as part of the light of the target star. Not correcting for this leads to an overestimation of small (rocky) planets, Hirsch et al. (2017).

These are just some examples of why stellar binary systems in particular are of interest to study. Binaries have many fundamental astrophysical properties yet to be understood, not only planet formation but also more underlying physics: How do stars interact in a binary? What are the conditions and consequences of stellar mergers at different evolutionary stages in binaries? What happens to the system as the stars evolve? How does that impact any existing planets? How do these systems compare to the solar neighbourhood? What type of stars are usually found in binaries? The two later questions can be addressed by looking at the K2 sample as done in this project. A sample of stars that were first observed by K2, the second operational phase of the space telescope Kepler in search for exoplanets. The main goals of this project are; to understand and characterize binary stars with exoplanets outside of the solar neighbourhood in terms of stellar properties and frequency. The results are then compared to a study of nearby stellar binary systems in Raghavan et al. (2010). From this we hope to learn what type of stellar binaries have planets and how the distribution of their properties compare to the solar neighbourhood.

This thesis report will begin with a description of the K2 mission in Section 2.1. A thorough explanation about speckle imaging in Section 2.2; its theory, usage and limitations including a brief introduction to observations in Section 2.2.1, a presentation of the instruments in Section 2.2.2 and an introduction of data reduction in Section 2.2.3. The last three sections mentioned contain a literature review of parts of speckle imaging that are only meant as context and a brief presentation of the full picture of speckle imaging, thus are not actually performed by the student and writer of this report. The data used were already reduced beforehand and loaded into ExoFOP.[5] The observations were done by the NASA speckle imaging group over the years 2016-2018. The theory of calculations and other methods used is given in Sections 3.1 through 3.3. Moreover, the extra step for a quick check of the derived masses; aperture photometry on adaptive optics images, is briefly explained in Appendix C. In Section 2.3 the full sample is presented and the results are presented in Section 4. Furthermore, a discussion about the method, how the project has gone, what the future goals are and the conclusions, are given in Section 5.

5 ExoFOP is a NASA database for Kepler, K2 and TESS exoplanet follow-up imaging and spectroscopy observations. `https://exofop.ipac.caltech.edu/k2/edit_target.php?id=201089381`

2 Background

2.1 The K2 mission

As aforementioned K2 is the second operational phase of Kepler, a space telescope launched by NASA in 2009, which was re-purposed due to a failure in two reaction wheels used to align the telescope. This problem meant that the space craft could not maintain a steady pointing. This was solved for K2 by using solar radiation to balance the space craft. However, this fix also meant that the field of view needed to shift every 80 days, so that after every 80 days the telescope observed another part of the sky. Such a set of observations for 80 days is referred to as a campaign.

In this way K2 observations include different types of targets and environments than first intended with Kepler (see Figure 1 for a schematic view of the spacecraft). Furthermore, K2 (and Kepler) were not intended to look for stellar binaries in particular, therefore the samples from these missions are not only randomized but also unbiased towards stellar binaries (Howell et al., 2014). Moreover, the K2 samples studied by speckle imaging and added to ExoFOP, have previously been shown to host exoplanet candidates, using transit observations, and for some cases planets have indeed been confirmed (Horch et al., 2012).

The Kepler spacecraft orbits in a heliocentric orbit at 0.5AU away from Earth, carrying a Schmidt telescope of 0.95m with a 110 degree field of view. The large field of view makes it possible to observe many targets at the same time, with high precision photometry (Howell et al., 2014). However, this also means that it cannot resolve any close companions, due to its low spatial resolution and large pixel scale; any close companions fall within the same camera pixel as the targeted star (Hirsch et al., 2017). Henceforth, speckle imaging is an important follow up program, for finding and resolving any companions to the targeted stars and study them further (for more detailed reading about K2, see Howell et al. (2014)).

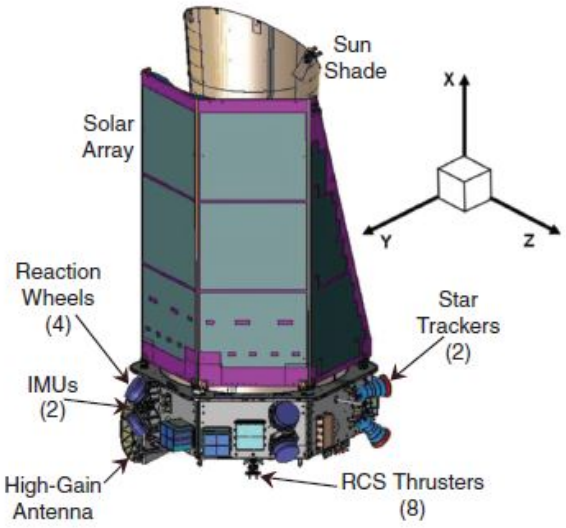

Figure 1: An illustration of the Kepler/K2 space craft. Source: Howell et al. (2014)

2.2 Speckle imaging

The most challenging problem with ground based telescopes is the disturbance and limitations caused by Earth's atmosphere and weather conditions. However, there are ways to optimize the surroundings in order to get better results, such as choosing a good position; high grounds where air, humidity and weather conditions are at best many days of the year. Nevertheless, the effects from the atmosphere cannot be excluded completely. However, in attempts to minimize the loss of spatial resolution due to atmospheric disturbances and quality, a new method based on short integration time and small field of view was explored in the 70s. Although, at that time due to technical limitations the method was only applicable to bright stars. Nevertheless, in the 90s, technology such as better cameras and telescopes made this method possible to use on faint stars too.

It turns out that by taking images with short integration time, 40ms-80ms, and high spatial resolution, the disturbance from the atmosphere is "frozen" in time resulting in a clean and high quality image, where only a few photons are collected per position (snapshots). These images can then be processed to, for example, find nearby companions. With longer exposure times the collected light tends to merge into a big blob of photons all falling at different positions in the camera, leading to loss of information and inclusion of too much background noise from the atmosphere. It is also necessary to understand that the longer the exposure the more elongated and blurred will the speckles be until they are no longer separated. Thereby, with this method of short exposures new useful information is brought to light about the objects observed that is not visible in long exposures. Figure 2 illustrates how the speckle pattern looks like and how it compares to a long exposure image (the middle pictures).

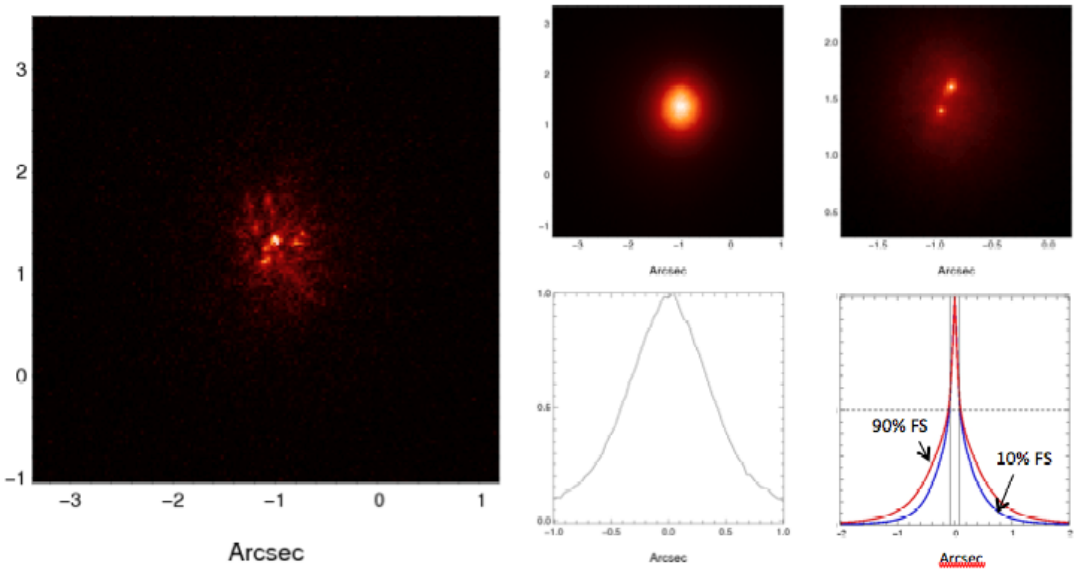

Figure 2: An illustration of the speckle pattern and image processing that leads to one signal for each star in a reconstructed image (to the right). Source: Labadie et al. (2010)

This method is called "Speckle imaging" or "Speckle interferometry" due to the pattern seen on the images of a light source, which resembles many small speckles. This pattern is visible for any point source, for which light is collected with short integration time, due to fluctuations caused by the seeing, which is how much the turbulence of Earth's atmosphere distorts an image (which is the reason why stars appear to twinkle on the night sky). Single light sources will show a collection of many identical single speckles closely spaced. While multiple stellar systems, such as binaries, give rise to pairs of identical speckles. This is mainly how targets with companions are directly distinguished from single stars.

One can compare speckle imaging to Young's double slit theory, where waves or particles (that also behave as waves in certain cases) always show a fringe pattern as they enter through two slits, because the waves interfere with themselves. The fringe pattern in Fourier space (the frequency plane) of speckle images, is simply a result of self-interference of the photons as they fall through the atmosphere similar to that in the double slit experiment. In speckle observations the speckle pairs act as "the slits" which in Fourier space give rise to a fringe pattern. Moreover, since the field of view is small the speckles (slits) are closely spaced. That is the photons that are collected from the two sources in principal fall through the same position in the atmosphere, which results in identical speckle pairs. This characteristic is important because it gives a clean fringe pattern, which is vital for high precision in the resulting parameters extracted from the images. The fringe pattern, how the waves self-interact similar to Young's double slit experiment, can be demonstrated easily for the naked eye by stacking a couple of speckle images and shining monochromatic light through the speckles onto a blank background. Or it can even be visible directly through a telescope (using real time video mode), when the seeing is exceptional and the telescope's spatial resolution is good. Thereby, it becomes clear why the pattern with speckle pairs is visible only for systems with two stars not for single stars.

This powerful observational method began as a way to resolve very close-by companions to any star of interest in order to understand multiple stellar systems. Later when exoplanets became a hot topic with the initiation of many missions to search for them such as Kepler, follow up speckle imaging programs were conducted both for Kepler and K2 (and other missions) stars in search for false positives; A dip in the light curve of the observed star that indicates a planet but is caused by a background star or a physical companion.

Moreover, as mentioned it was soon understood that a companion, background star or binary companion, can cause us to underestimate the radii of exoplanets. A larger radius translates into higher density, meaning rocky planet, thus leading to an overestimation of that planet category. Therefore, it is vital for accurate characterization of all exoplanets to correct the radius. It is also interesting to find correlations between stellar and exo-

planet properties and better understand planet formation and evolution in stellar binaries.

Even though speckle imaging is used in many studies with different purposes, sometimes just as a method of fast, high spatial resolution imaging, the method has limitations, some being enforced by observing conditions and others by the method itself. The main one is the detection limit on the magnitude of the companion, which depends on the telescope parameters. There is a strong correlation between how faint the companion can be and the size of the telescope mirrors that determines if a companion is detected. Moreover, the ability to detect a companion can be decreased by bad seeing conditions. In occasions with bad seeing, for example 1.4″, companions at a separation of less than roughly 1.3″-1.2″ , or very faint (larger than ≈11-10 magnitude) will not be clearly or at all resolvable, even if the same companions would be possible to see with that telescope otherwise. This problem can be worked around by observing the same targets another night with better atmospheric conditions. The speckle imaging method's limitations, such as lower limit on resolvable angular separation, can only be improved by new and better instruments.

In order to account for these limitations for each observation, the minimum brightness for a companion to be detected at different distances from the target star, are put together into a detection limit curve that is calculated for each target, filter and telescope at every observing run. From many such curves one can derive an average for each telescope and get a better view of what is the typical range of magnitude difference at different angular separations that can be detected at that telescope (Matson et al., 2018; Howell et al., 2011). This is important to understand, because it shows what observers need to know before hand and how far the method can be pushed without compromising the data.

Another constraint on the method involves angular separation between the target star and its companion. The detectable range of angular separations is usually set at between 0.02 -1.2″. The lower limit is enforced by the telescope parameters. That is the diffraction limit of the telescope, which depends on the wavelength of the light collected and the diameter of the mirror, constraining how small angular separations we can resolve in the images. The upper limit can be increased to 2″, however, the data is not reliable at such large separations. The reason being that the speckles get more elongated and the fringe pattern more blurred as light does not fall through the same patch of the atmosphere, thus the speckles are no longer correlated. Moreover, sometimes speckle pairs can fall outside the field of view of the instrument. In both cases the fringe pattern in Fourier space is not as clear or focused, resulting in unreliable parameters (Horch et al., 2012; Howell et al., 2011).

In conclusion speckle imaging is a powerful tool for observations which has opened up many new fields of astronomy and is widely used.

2.2.1 Observations

Firstly, the observations of the sample in this project were not done by the student. Thus this section consists of a brief literature study of the main parts of speckle imaging observations to give context and a complete picture of the subject.

All speckle imaging observations, that are done by the science group at NASA Ames Research Center, are done at the Gemini-telescopes and WIYN using the instruments DSSI, Alopeke, NESSI and the newly commissioned Zorro instrument. The data used in this thesis come from observations done at these telescopes using the instruments DSSI and NESSI.

The Gemini-telescopes are two twin telescopes located in Hawaii (Gemini-North) and Chile (Gemini-South). These have 8.1m primary mirrors and secondary mirrors of 1m diameter.[6] The WIYN telescope is smaller, it consists of a primary mirror of 3.5m diameter and a 1.2m in diameter secondary mirror, located in Arizona USA.[7]

In short the observing procedure includes software such as the image/video display program SAOImageDS9, a telescope and a speckle instrument. Nowadays, the observations can easily be done remotely, but even on site it usually consists of computer work. The science target is viewed as an image or in real time using video mode in SAOImageDS9. To determine or change how much light is collected per image the parameter "gain" is adjusted manually. The parameter "gain" determines how much the signal is magnified by controlling the multiplication register in the detector before read out, so that the signal gets stronger. The goal is to collect enough light for a good signal without saturating the detector (which means photons "run over" into another pixel giving bad read outs, this happens at too large gain). For fainter targets the "gain" used must be higher, in this way there will still be a useful signal even with few photons. The necessary amount of photons is around 10000 counts and no higher than roughly 30000, with a saturation limit at roughly 65000 (Everett et al., 2015; Labadie et al., 2010).

Once the gain is set to the desired value different number of sets of 1000 frames are saved per target, reading out only 256x256 pixels of the full frame of the EMCCD (electron multiplying CCD) camera each time, because it is less time consuming and takes less storage space (Howell et al., 2011). The number of sets is determined by how faint the target and the companion are, if faint then the number of sets is increased but is always within the range of 3-12 sets (Everett et al., 2015; Horch et al., 2012).

The integration time for each image can be 40-80ms depending on which is best for the instrument and telescope used. For the observations of this sample the integration

6 See more about the Gemini telescopes on the official telescope website: `https://www.gemini.edu/observing/telescopes-and-sites/telescopes`

7 See more about the WIYN telescope on the official telescope website: `https://www.wiyn.org/About/overview.html`

time was 40ms per image. In Howell et al. (2011), this was found to be best for speckle imaging observations with their instruments and is not varied with seeing.

2.2.2 Instrumentation

This section is also a literature study to show briefly the main parts of the speckle imaging instruments. There are four speckle instruments, DSSI, NESSI, Alopeke and Zorro. All have the same basic structure and main components as shown in Figure 3. They each have two filters 562 and 832nm or 692 and 880nm with a width of 40nm (Howell et al., 2011). For more details on each instrument structure and function refer to Howell et al. (2014), Horch et al. (2009) and Scott et al. (2018).

In short, the function of the instruments is as follows: Light passes through the telescope mirrors which is then focused and sent through a focal length lens in the speckle instrument, where the light is collimated.

In front of each camera there is a filter with narrow bandpass that the light passes through before reaching the cameras.

The EMCCDs on DSSI have a 512x512 frame with 16μm pixels (the other instruments have similar numbers). It then travels further to the galvanometer mirrors where it is directed to a dichroic beamsplitter via reflection. At this position the light is divided into two paths leading to the two cameras respectively (Horch et al., 2012).The cameras are optimized to be sensitive to low levels of light (Howell et al., 2011). The CCD pixels collect the photons, which are read out by converting the counts of each pixel into electrons (Horch et al., 2012; Howell et al., 2011).

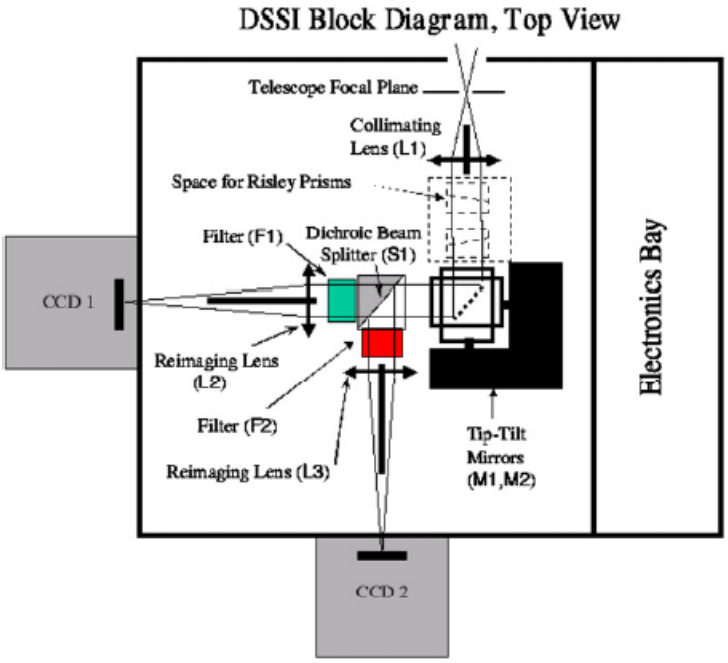

Figure 3: A layout of the instruments. Source: Horch et al. (2009)

2.2.3 Data reduction and processing

At the end of an observing run the data needs to be reduced. Today most instruments have a dedicated pipeline for this. The data from the different filters is processed separately. The reduction of the data used in this project was done by Mark Everett at National Optical Astronomy Observatory. Thus this section is included here only to give context and a brief description.

In the first step the frames are looked through and removed if the pattern is unclear or has any other imperfections, such as too few photons. The pipeline then searches each frame to identify those with the same speckle separation, all these frames are then stacked together for each set and averaged over all sets for better results and higher signal to noise ratio. This average is then Fourier transformed to its power spectrum; a spatial frequency function in Fourier space (Horch et al., 1996; Horch et al., 2010). The resulting fringe pattern of the science target is then fitted to a fringe model, which finally gives the separation between the stars and the magnitude difference (Horch et al., 2010).

To find the position angle[8] of the companion, bispectral analysis is applied. Moreover, from this information a reconstructed image where both stars are visible as two light sources can be reconstructed (Horch et al., 2012).

2.3 The sample

The sample for this project consists of stars with a mass range of 0.2-2$M_{\odot}$, assumed to be on the main sequence. The speckle imaging observations were done with the instruments DSSI at Gemini north/south and NESSI at WIYN, where the aim was to look for close companions. These stars are KOI (K2 objects of interest) from the K2 mission, which are believed to be exoplanet candidate hosts. Actually for this sample some systems do have confirmed planets and some have confirmed candidates which is interesting, but in this project the focus is on the stars in the system. We need to understand the stars first, then study aspects and questions related to the planets in stellar binaries.

8 The position angle is defined as the position in the sky of the companion compared to the targeted star and us. Note that this parameter was not necessary for my calculations of the properties.

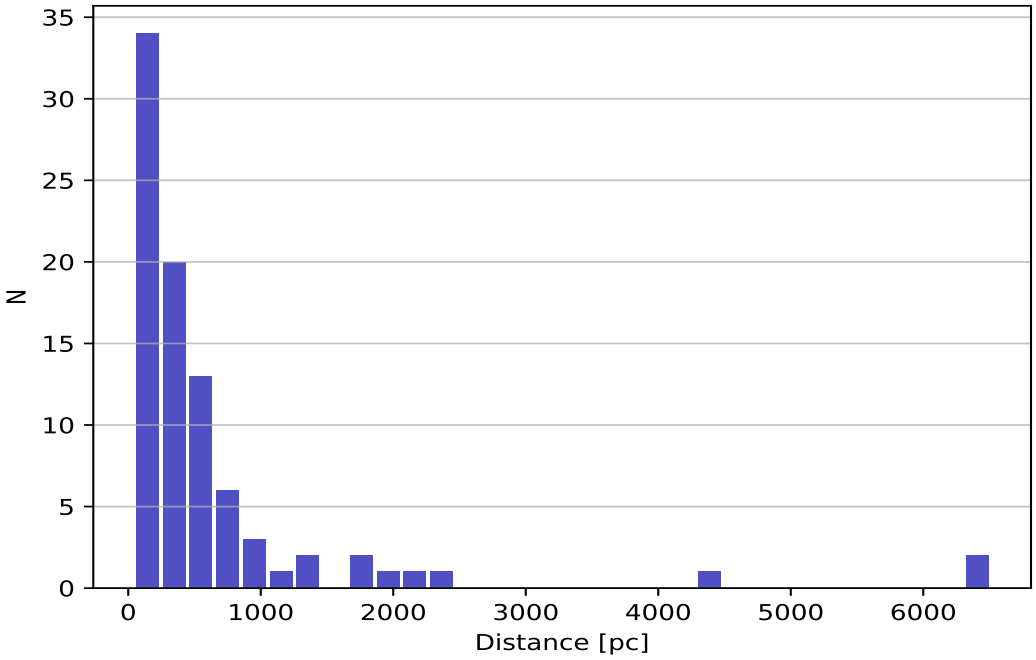

Figure 4: Distribution of distances to all the primaries in the sample. Most of the systems are within 1000 pc which is expected due to the limitations of the method: Further away means smaller angular separation and harder to resolve.

The sample consists of low-mass stars and bright solar-like stars found on a wide range of latitudes which have one companion. Note that from now on the target star is always referred to as the primary and the companion is referred to as the secondary. Figure 4 shows the distances of the primaries, there are 11 systems out of the 100 in total missing in this plot, because those did not have distances determined. The distances were inferred according to Bailer-Jones et al. (2018) by Megan Bedell.[9] The furthest away systems lacked information necessary to find the masses of the components and the orbital period, they were thus excluded from the main study. Moreover, distant systems can have very small angular separations that cannot be resolved by speckle imaging even at good seeing (lower limit is at $0.02''$).

Furthermore, the primaries of this sample have relatively small apparent magnitudes and companions with, in most cases, small magnitude differences. It is difficult to observe and resolve companions with higher magnitude difference even more so at larger distances. Because speckle instruments in general reach maximum sensitivity before that (limitations of speckle imaging were discussed in Section 2.2). This is demonstrated with plots of the visual apparent magnitude as a function of the distance to the system in Figures 5 and 6, which are consistent with findings in other papers such as Matson et al. (2018). They show

9 The distances to the primaries in the sample, have been inferred from Gaia parallaxes by Megan Bedell according to Bailer-Jones et al. (2018). These distances were extracted from a data file, found on Megan Bedell's website; `https://gaia-kepler.fun/`

that for systems further away we usually find brighter stars (less than 16 magnitudes) and the errorbars are large, while opposite holds for close by systems which have a larger range of magnitudes and small errorbars.

In total there are 100 systems in my study, however only 72 are included and studied here. For the remaining 28 systems there is not enough data to carry out a full analysis. For example, as it became clear in earlier sections, if there is no distance to the system, the orbital period and the physical separation cannot be found.

Most of the stars in the sample have speckle observations in two filters. Although four of these systems have results from all four filters. Moreover, if the companion was too faint in one filter (larger apparent magnitude in these bands than detectable by the instruments) or fell outside of the field of view, the images are unreliable and the resulting parameters were not given on ExoFOP.

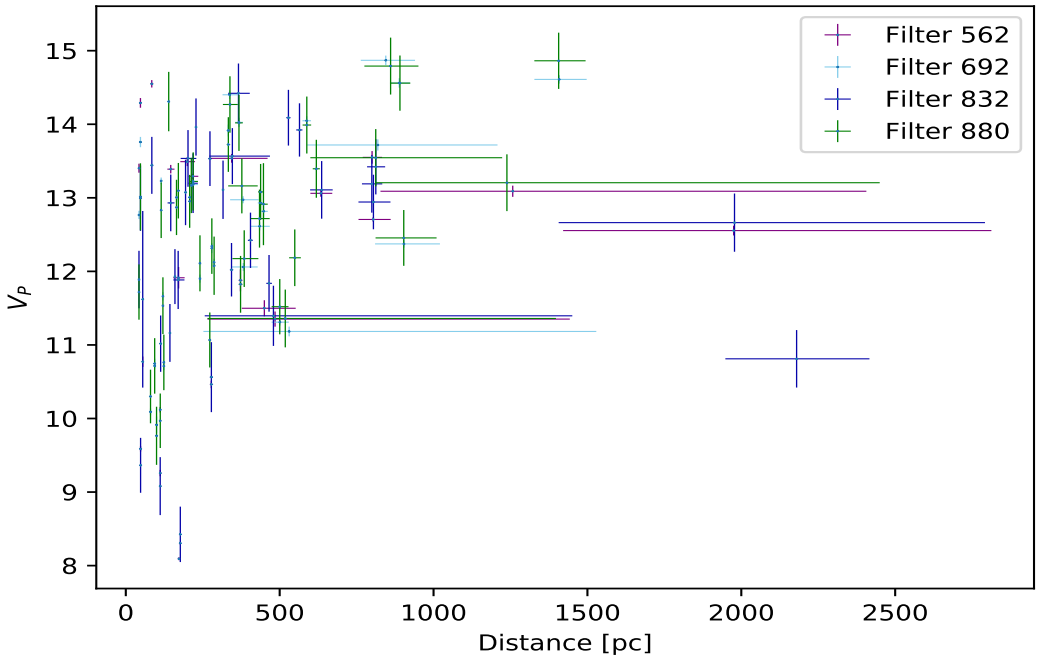

Figure 5: The visual apparent magnitude as a function of the distance to the system, for all the primaries in the sample. Filter wise colour coded, see legend. Most primaries have magnitude brighter than 14.

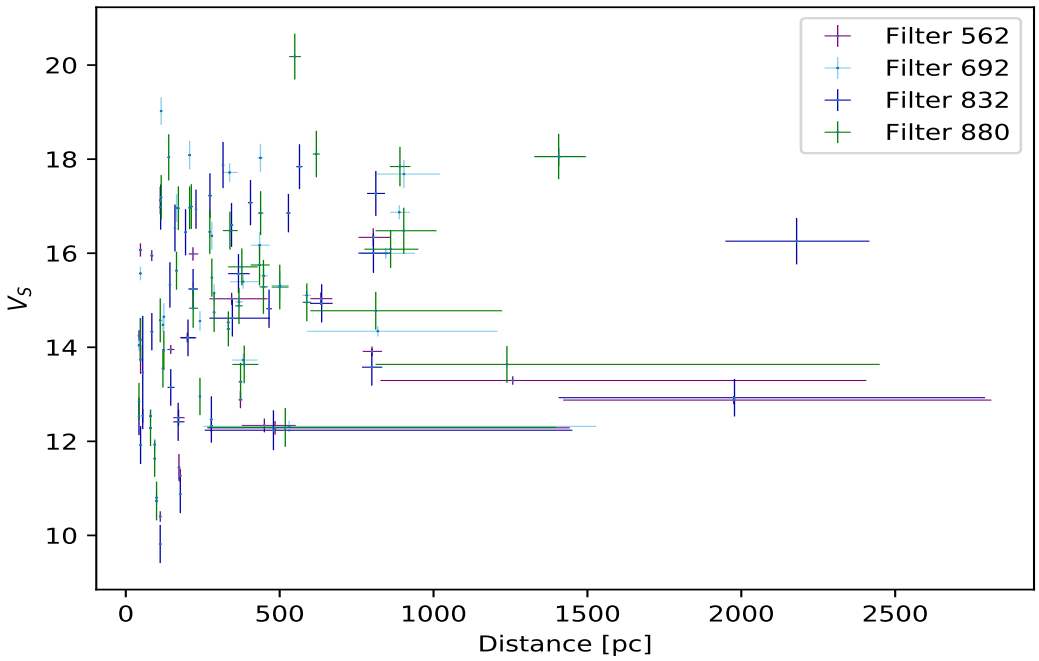

Figure 6: The visual apparent magnitude as a function of the distance to the system, for all the secondaries in the sample. Most systems are at short distances from the solar system. Note that the scale of this plot is different from that in Figure 5 because the secondaries have larger magnitudes.

3 Estimation of stellar properties

The properties to be estimated are masses of and physical separation between the system components and the orbital period. The starting point of the project was to retrieve data from ExoFOP. Data retrieval was done manually due to lack of a better method to extract specific information, and time to find one. The speckle imaging information extracted from ExoFOP was the magnitude difference and the angular separation between the stars (see tables in Appendix B).

The next step was calculations of properties, which were performed according to the theory and steps explained in the sub-sections to follow.

3.1 Physical separation

The first property to be calculated was the physical separation between the two stars in the system, using the angular separation between the stars and the distance to the primary. As it is not possible to tell the positions of the stars exactly compared to each other and us, the problem is simplified into a regular right angle triangle as shown in Figure 7. Moreover, we know that the distance to the primary, a, is much larger than the distance between the primary and the secondary, b. Therefore, we can make the approximation shown in Equation (1) and find a lower limit of the physical separation.

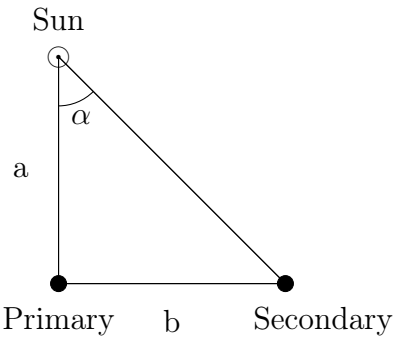

Figure 7: The right angle triangle setup used to find the physical separation. Where a is the distance to the primary, b is the physical separation and α is the angular separation.

$$b = a \cdot \tan(\alpha) \tag{1}$$

3.2 Masses

The next property to be estimated was the mass of each star in the system and their mass ratio (the mass of the secondary divided by the mass of the primary). For this step the estimations were done using the magnitude difference and mass-luminosity relations, MLR. The relations used came from a study by Henry and McCarthy (1993). These relations are in V-, K-, J- and H-band and only hold for stellar masses below $2.5\mathrm{M}_{\odot}$ (see

Equations (2) through (7)).

$$\log(M/M_\odot) = 0.002456M_V^2 - 0.09711M_V + 0.4365 \quad (1.45 < M_V < 10.25) \tag{2}$$

$$\log(M/M_\odot) = 1.4217 - 0.1681M_V \quad (10.25 < M_V < 12.89) \tag{3}$$

$$\log(M/M_\odot) = 0.005257M_V^2 - 0.2351M_V + 1.4124 \quad (12.89 < M_V < 17.59) \tag{4}$$

$$\log(M/M_\odot) = 0.3217 - 0.1048M_K \quad (3.07 < M_K < 5.94) \tag{5}$$

$$\log(M/M_\odot) = 1.1965 - 0.2521M_K \quad (5.94 < M_K < 7.70) \tag{6}$$

$$\log(M/M_\odot) = 0.5395 - 0.1668M_K \quad (7.70 < M_K < 9.81) \tag{7}$$

Where M_K is the absolute magnitude in the K-band, M_V is the absolute magnitude in the visual band and M is the mass of the star in question. Each MLR holds for a specific absolute magnitude range which is also indicated in the equations.

In order to use these relations to get the individual masses, the absolute magnitude for each star must be found by using the one available quantity from speckle observations, namely the magnitude difference, and the apparent magnitudes (in r-, i- and V-band) available on ExoFOP. The steps towards this were different and more or less complex for each filter.

Firstly, as done in previous papers using speckle imaging data, the filter 562 was assumed to be closest to the V-band, 692 to the R-band, 832 and 880 to the I-band, even though this is not quite accurate since these filters are much narrower than the usual V, R, I-bands. Nevertheless, as will be visible in the results, the masses are reasonable and agree within the errors with the masses found using aperture photometry. Moreover, as will be discussed in later sections the overall trends or correlations between the masses and the other properties, shown in other papers are also seen here.

To get the absolute magnitude one needs to find the distance to the system and the apparent magnitude, in this case in the V-band.

$$M_V = V - 5\log(d/10) \tag{8}$$

Where V is the visual apparent magnitude of the star in question and d is the distance

to the system. Note that extinction has been neglected because all systems are within 1000pc and most of them within even shorter distance than that. However, this will affect the mass estimates and the accuracy, resulting in smaller values, which we are aware of. Therefore, we see these masses as only estimates of a minimum and in the future for more accurate mass measurements the first step would be to include extinction.

For the 562 filter it was straight forward; use the magnitude difference between the two stars, (Δmag) and the magnitude on ExoFOP (both in V) to get the apparent visual magnitude of each star, see Equation (9).

$$\begin{aligned} V_S &= V_{ExoFOP(P+S)} + 2.5\log(1+10^{0.4\Delta mag}) \\ V_P &= V_S - \Delta mag \end{aligned} \tag{9}$$

Where the P and S indices designate the primary and the secondary, respectively.

As for the other filters the steps were more complex, because the magnitude difference in these filters is not in the visual band already as for the 562 filter and the available apparent magnitudes on ExoFOP are not in the same band as the magnitude difference. Therefore, there needed to be many intermediate steps of rigorous manipulation of magnitude transformation relations.[10]

The first steps for the three other filters was to use the r, i apparent magnitudes from ExoFOP to get R_{P+S} using Equation (10), which for the 692 filter was then directly inserted in Equation (9) to get the individual apparent magnitudes in R-band. For the filters 832 and 880 it is instead used to find I_{P+S} first, using Equation (11), which then together with the magnitude difference was inserted in Equation (9) to get the individual stellar magnitudes in the I-band. Then to get the visual apparent magnitude, Equation (13) was used for the filters 832 and 880, whereas for the 692 filter Equation (12) was used.

$$R_{P+S} = (-0.153)\cdot(r_{ExoFOP} - i_{ExoFOP}) - 0.117 + r_{ExoFOP} \tag{10}$$

$$I_{P+S} = \frac{i_{ExoFOP} - 0.247R_{P+S} - 0.329}{0.753} \tag{11}$$

Where the index P+S refers to the total magnitude of the system.

$$V = \frac{R + 0.508B + 0.040}{1.508} \tag{12}$$

10The magnitude conversion relations were found on the following two websites and were a summary of the findings in Jordi et al. (2006) and Natali et al. (1994):
`http://www.sdss3.org/dr8/algorithms/sdssUBVRITransform.php`
`http://www.aerith.net/astro/color_conversion.html`

$$V = \frac{1.36B + I}{2.36} \tag{13}$$

Where the letter B is the magnitude in B-band. Although there has not been any mention of B-magnitudes before now, this must also be found for each star using Equation (14) for the filter 692 and Equation (16) for the filters 832 and 880 (found using the equation system in Equation (15)).

$$\begin{cases} V - g = h(g - r) - i \\ r - R = j(V - R) + k \\ B - g = l(g - r) + m \end{cases} \Rightarrow B_{692} = \frac{l+1}{h+1}\left(\frac{r+R(j-1)-k}{j}\right) + \frac{rh(l+1)}{h+1} + \frac{i(l+1)}{h+1} - lr + m \tag{14}$$

$$\begin{cases} V - g = h(g - r) - i \\ r - R = j(V - R) + k \\ R - I = q(r - i) + w \\ r - i = a(R - I) - b \\ B - g = l(g - r) + m \end{cases} \tag{15}$$

$$\Rightarrow B_{832/880} = \frac{(l+1)(r + qr(j-1) + w(j-1) + I(j-1) - k)}{j(h+1)} + \frac{(l+1)(hr+i)}{h+1} \\ \frac{q(l+1)(j-1)(r(1-aq) - aw + b)}{j(h+1)(1-aq)} - lr + m \tag{16}$$

Where V,g,r,R,B,I are the magnitudes in respective band, and h,n,j,k,q,w,a,b,l,m are the constants in the magnitude conversion relations.

As one can see, the equations above to find B also require the r-magnitude for each star. Note that we are now working with the individual stars in the system aiming to find the apparent magnitude for the primary and the secondary, respectively. Therefore the r-magnitude given on ExoFOP cannot be used, because that magnitude is not corrected for another star, instead it is the magnitude for the whole system. Thus the individual r-magnitudes must be found by solving yet another set of equations; Equation (17) for the filter 692 and Equation (18) for the filters 832 and 880.

$$\begin{cases} r - i = a(R - I) - b \\ R - r = c(r - i) - d \\ R - I = e(r - i) + f \end{cases} \Rightarrow \quad r_{692} = \frac{R(1-ae) - acf + cb + d(1-ae)}{(1-ae)} \tag{17}$$

$$\begin{cases} r - i = a(R - I) - b \\ R - r = c(r - i) - d \\ R - I = e(r - i) + f \end{cases} \quad \Rightarrow \quad r_{832/880} = \frac{eaf - eb + f(1-ae) + I(1-ae) - acf + cb + d(1-ae)}{(1-ae)} \tag{18}$$

Where c,d,e,f are also constants of the magnitude conversion relations.

Finally, the visual apparent magnitude was found using Equations (12) and (13), which was inserted into Equation (8) to get the visual absolute magnitude. The visual absolute magnitude values were then inserted into the correct MLR to find the individual masses for each filter.

3.3 Orbital period

It is difficult to wait for observations to show the orbit of a star so far away and accurately determine the orbital period, it can take a long time. Therefore, we simplify the problem by assuming circular orbits and using the physical separation between the stars as the semi-major axis, which is a valid approximation in the center of mass reference frame. Nonetheless, due to the approximation, the values found are only estimates of a lower limit of the orbital period. For this task Kepler's third law of motion was used:

$$P^2 = \frac{4\pi^2 a^3}{G(M_P + M_S)} \tag{19}$$

Where P is the orbital period, a the semi-major axis, M_P is the primary mass and M_S is the secondary mass. Casting the equation into units of years rather than seconds gives the following:

$$P = \frac{(1.16 \cdot 10^{17})\pi a^{3/2}}{(1.178 \cdot 10^{21})(M_P + M_S)^{1/2}} \cdot \frac{1}{3.2 \cdot 10^7} \tag{20}$$

3.4 Error estimation

The last step of the project was to calculate the errors of all the properties. For this a simple form of Monte Carlo simulations was used. The main idea is to generate a random distribution for the mean/median of each variable with given error as standard deviation.

This new array of the parameter, with 1000 generated values, was then inserted in the different equations, instead of just inserting the given mean/median of the variable. This way we work with the full distribution of the involved variables throughout every equation, thus propagating all the errors in every step. Then every property; the masses, the orbital period and the physical separation, are given as a distribution, from which one can extract the average and the estimated errors.

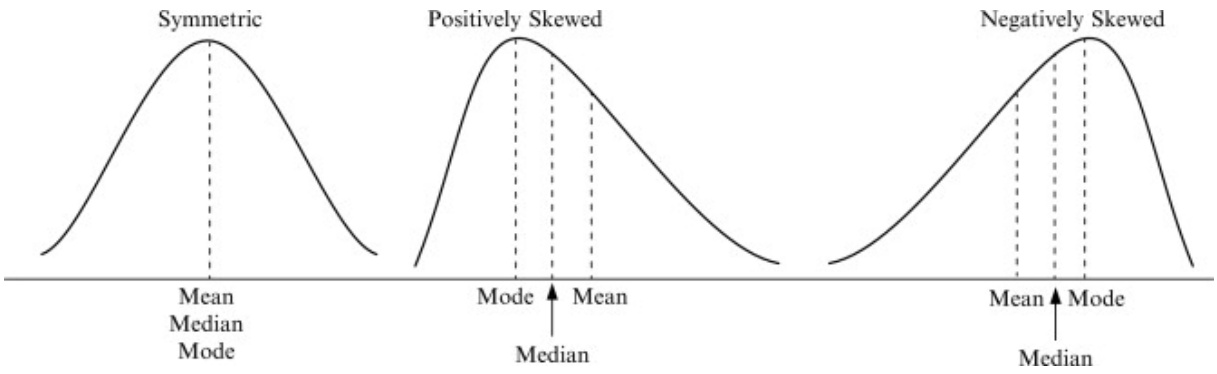

Figure 8: Skewed distribution. Source: Siegel (2016)

Most of the variables used in the equations have a normal distribution, except the distance to the primary. The distance to the primary was inferred according to Bailer-Jones et al. (2018) by Megan Bedell, in a more accurate way but in principle still as the inverse of the parallax. Which results in a skewed distribution, not a normal distribution, and has asymmetric errors (see Figure 8 for an illustration of the different distributions). Thus all the properties where this variable was involved such as the visual absolute magnitude will also have asymmetric errors. But that is not a problem since we are constantly working with the full distribution; the mean/median and errors are extracted only at the end of each calculation. For skewed distributions the value is now the median and the error is divided into two different numbers, one sigma to the right and one sigma to the left of the median. The errors of an asymmetric distribution are found using 15:th and 84:th percentile of the distribution.

4 Results

We now turn to a presentation of the results obtained using the methods of estimating the properties explained in the preceding sections, which were implemented by the student using Python.

The first plot, Figure 9, shows the magnitude difference as a function of the angular separation. This is a useful way to see how many systems are likely bound. Studies such as Hirsch et al. (2017) and Matson et al. (2018) have shown that two stars in a system with a separation within $0.4''$ are $89-99\%$ bound, forming physical binaries. The probability for actual binaries decreases significantly with larger separation. Those systems are then more likely chance alignment, meaning they seem to be in the same system as viewed from us but are not in reality. In the plot the probabilities for the different ranges of separation are marked with dashed lines and the percentage is given for each region. It is possible then to see that many of the systems are within $89-99\%$ probability to be actual binaries. I found that there are 26 unique systems with an angular separation less than $0.4''$, i.e are potentially actual binaries. Note that counting the systems on the plot will give a higher number because there are systems that have measurements in more than one filter, thus not all those points represent unique systems.

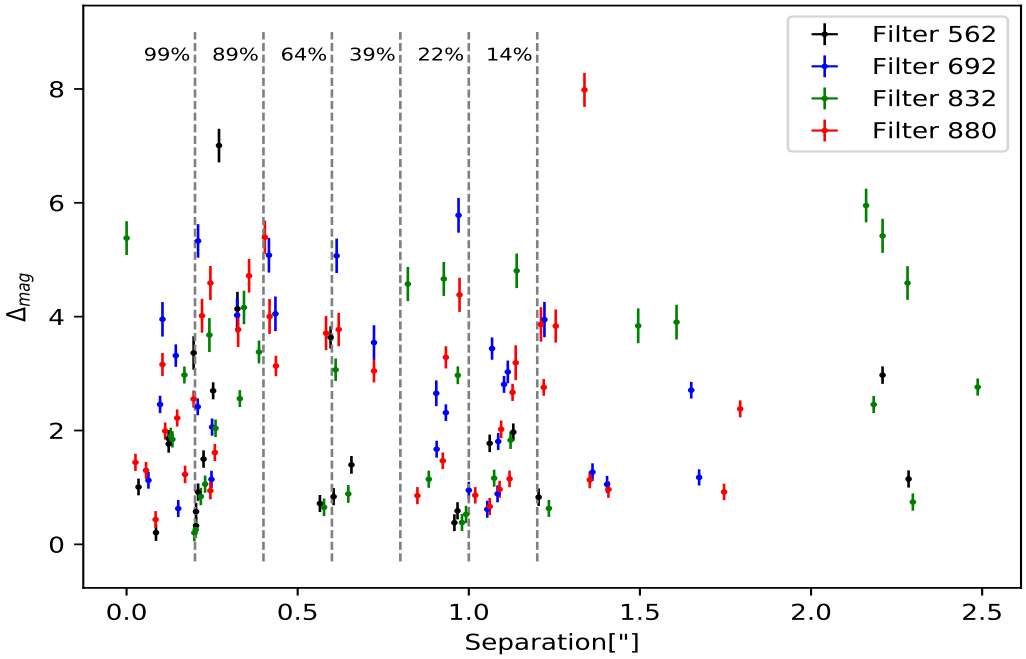

Figure 9: A plot of the magnitude difference as a function of the angular separation. The four filters are shown with different colours (see legend). The vertical dashed lines are at the angular separations $0.2''$ to $1.2''$ with step size of $0.2''$, the percentages show the probability for bound stars at each region.

In the plots below, Figures 10 and 11, the systems with detected companions were separated according to which telescope they have been observed with. As explained earlier speckle imaging has detection limits which depend on the size of the telescope mirror and the conditions of the observations. In the plots these are presented as detection limit curves for the telescope, the observation date and the filter used. These are included to demonstrate the limitations of the speckle imaging method based on the telescope and are randomly chosen examples from observations of the system with epicname 228920801.[11] The measurements above the limit curve and at larger angular separation than 1.2″ are real observations even if they are not below the detection limit curves. These systems can still be detected in very good observing conditions.

Using these plots the companion fractions discussed below are found and compared to Matson et al. (2018) and Horch et al. (2014), where they also compare their observational fractions with predictions from simulations. Their simulations are done based on the total binary fraction of $40 - 50\%$, taken from Raghavan et al. (2010), and the speckle imaging detection limit curves.

In order to find the fraction of binaries at each telescope the total number of unique observations is needed. At the time of extracting the data from ExoFOP, there were 690 unique observations and 100 with companions, which is 14%. However, I did not make notes about the total number of observations at each telescope at that time. Thus I first recounted the total number of observations, but the number is higher, 732, meaning new observation must have been added. Using these new numbers would give inconsistent fractions. To solve the issue I choose to count the total unique observations at each telescope today (262 systems observed at Gemini and 548 at WIYN), then use the percentage they correspond to get what the number of observations at each telescope would have been at the time of extraction (March 2019). We then get $262/732 = 0.36 \rightarrow 0.36 * 690 = 246$, so 246 unique observations at Gemini, and $548/732 = 0.75 \rightarrow 0.75 * 690 = 516$, 516 unique observations at WIYN. Moreover, there are 38 unique observations with companions at Gemini and 41 at WIYN. With these numbers we get the fractions $38/246 = 0.15$, that is 15% for Gemini and $41/516 = 0.08$, which is 8% for WIYN. The fractions presented here agree within error with other work such as Matson et al. (2018) and Horch et al. (2014). If we now exclude those systems that are not below the detection limit curves in both plots, leaves us with 27 unique observations at Gemini and 25 at WIYN. The fractions then change to 11% for Gemini and 5% for WIYN, these also agree within error to Matson et al. (2018) and Horch et al. (2014).

11The epicname is a long number-name assigned from the EPIC catalogue

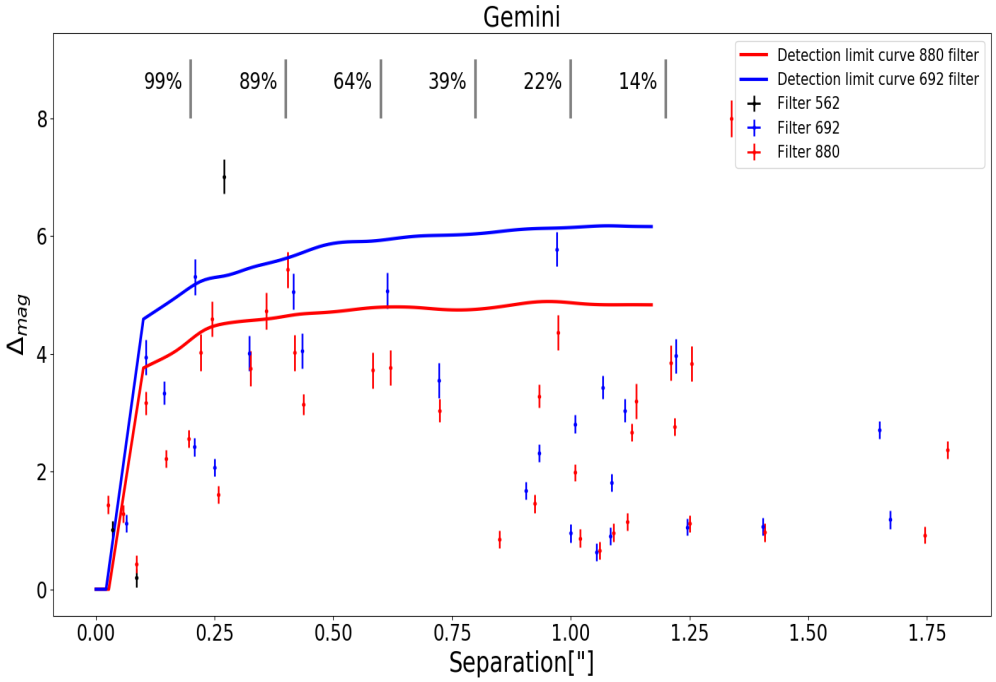

Figure 10: The magnitude difference as a function of the angular separation for observations at the Gemini telescopes. Example of detection limit curves and the probability of being bound based on Matson et al. (2018) are included here, see legend.

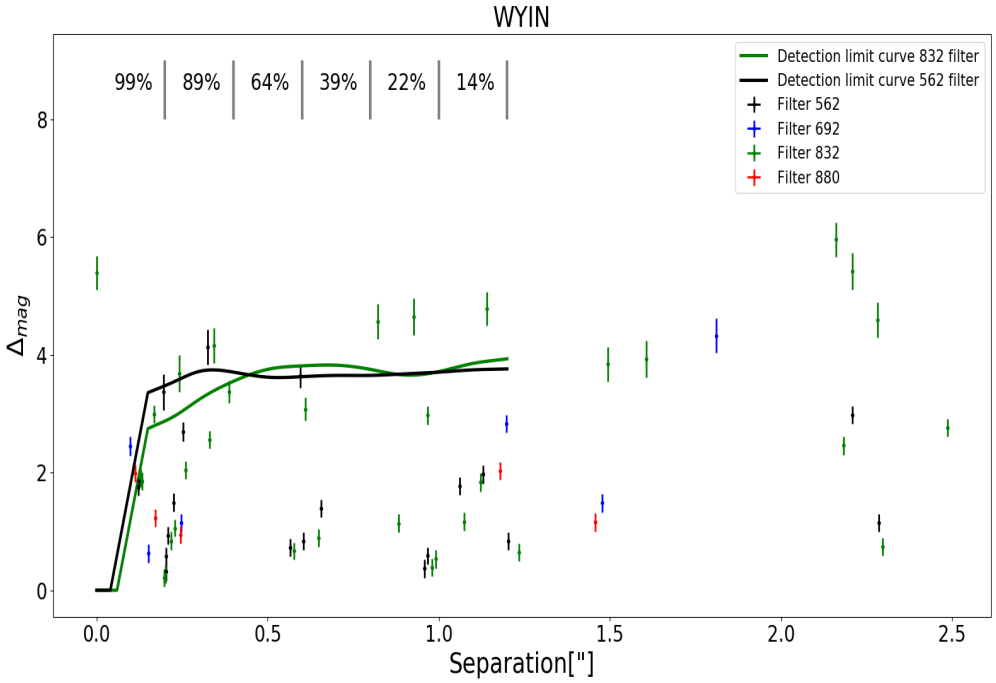

Figure 11: The magnitude difference as a function of the angular separation for observation done at the WIYN telescope. The probability for bound stars at each region is marked out and two detection limit curves are included, see legend.

The epicnames, the angular separation and the magnitude difference of the 26 unique bound systems are found in Table 1. The values in this table have been averaged. That is if the system was observed more than once in the same filter an average was found in order to give one value for each of the filters. Note however, that there are more than 26 rows in the table, that is because many of these systems were observed in more than one filter. They must all be included since we cannot average the magnitude difference over different wavelengths.

Moreover, note that the angular separation agrees well in the different filters, which is important because the filter in itself should not affect the resulting parameters when the observation technique is the same. This gives a good ground to work on as we estimate other properties.

Table 1: The table below shows the information for the 26 potential bound systems (within $0.4''$ angular separation). The information consists of the epicname, the magnitude difference with errors, the angular separation (which has a given error of $0.002''$) and the physical separation in units of AU with asymmetric errors.

Epicname	Δmag	Angular separation ["]	Physical separation[AU]
211439059	1.50±0.15	0.23	78^{27}_{17}
211439059	1.05±0.15	0.23	78^{27}_{17}
211941472	0.33±0.15	0.20	399^{166}_{115}
211941472	0.26±0.15	0.20	401^{162}_{113}
212138198	2.69±0.15	0.25	$55^{4.1}_{4.0}$
212138198	2.06±0.15	0.25	$55^{4.0}_{3.0}$
212138198	2.05±0.15	0.26	$57^{4.1}_{3.8}$
212138198	1.61±0.15	0.26	$56^{4.3}_{4.0}$
212703473	0.93±0.15	0.21	102^{205}_{49}
212703473	1.15±0.15	0.25	124^{228}_{62}
212703473	0.84±0.15	0.22	106^{203}_{47}
212703473	0.94±0.15	0.24	119^{234}_{56}
214889247	7.01±0.30	0.27	$30^{0.4}_{0.3}$
214889247	4.59±0.30	0.24	$27^{0.4}_{0.3}$
216050437	0.20±0.15	0.09	106^{97}_{37}
216050437	0.45±0.15	0.08	102^{100}_{37}
218711655	1.01±0.15	0.03	$13^{\{0.7}_{0.8}$
218711655	1.44±0.15	0.03	$10^{0.8}_{0.7}$
220492184	3.36±0.30	0.20	$34^{0.9}_{0.8}$
220555384	0.57±0.15	0.20	$30^{2.4}_{2.3}$
220555384	0.21±0.15	0.20	$29^{2.4}_{2.2}$
247002634	4.15±0.30	0.32	$16^{0.2}_{0.3}$

Table 1 continued from previous page

247002634	2.55±0.15	0.33	$16^{0.3}_{0.2}$
247452471	1.87±0.15	0.12	$34^{0.8}_{0.9}$
247452471	1.90±0.15	0.13	$36^{0.9}_{0.8}$
247611242	1.76±0.15	0.12	$7^{0.2}_{0.1}$
247611242	1.86±0.15	0.13	$7^{0.1}_{0.2}$
201352100	3.36±0.20	0.39	$75^{1.4}_{1.5}$
201392505	3.70±0.30	0.24	$66^{1.7}_{1.6}$
212619190	5.38±0.30	-	-
220725183	2.98±0.15	0.17	$79^{1.7}_{1.9}$
246920193	4.15±0.30	0.34	$49^{0.4}_{0.5}$
211886472	4.01±0.30	0.32	$162^{9.0}_{8.5}$
211886472	3.78±0.30	0.33	$163^{11}_{8.8}$
212066407	5.32±0.30	0.21	190^{25}_{20}
212066407	4.02±0.30	0.22	199^{24}_{22}
212099230	3.94±0.30	0.11	$13^{0.2}_{0.3}$
212099230	3.17±0.20	0.10	$13^{0.3}_{0.2}$
212303338	2.45±0.15	0.10	$8^{0.1}_{0.2}$
212303338	1.99±0.15	0.11	$9^{0.1}_{0.2}$
212315941	1.12±0.15	0.06	$55^{6.9}_{5.7}$
212315941	1.30±0.15	0.06	$48^{6.0}_{5.0}$
212534729	0.63±0.15	0.15	126^{56}_{33}
212534729	1.23±0.15	0.17	142^{67}_{40}
218131080	2.42±0.15	0.21	$79^{10}_{8.9}$
218131080	2.55±0.15	0.20	$73^{10}_{7.6}$
229002550	3.33±0.20	0.14	$49^{3.8}_{3.5}$
229002550	2.22±0.15	0.15	$50^{4.0}_{3.4}$
228920801	4.74±0.30	0.36	$222^{4.2}_{4.3}$

We now turn to look at how these properties correlate. Starting with a plot of the magnitude difference as a function of the physical separation in astronomical units (Figure 12, which is similar to the plot in Figure 9). This shows the distribution of the physical separation. All systems fall at separations within 2000 AU. Moreover, most of these systems are within 500 AU, which is mostly due to the detection limits of speckle imaging; a balance between the distance to the system and the width of the field of view of the speckle instruments and the brightness of the stars in the system. Furthermore, this plot shows how big the errors are, which in general says that the errors are larger the further apart the stars are, due to less reliable speckle imaging measurements, as expected and explained in Section 2.2. Some exceptions to this exist, there are points at small separation

with quite big error bars, which most likely is due to poor observing conditions that automatically increase the errors on the involved variables and the end result, the physical separation.

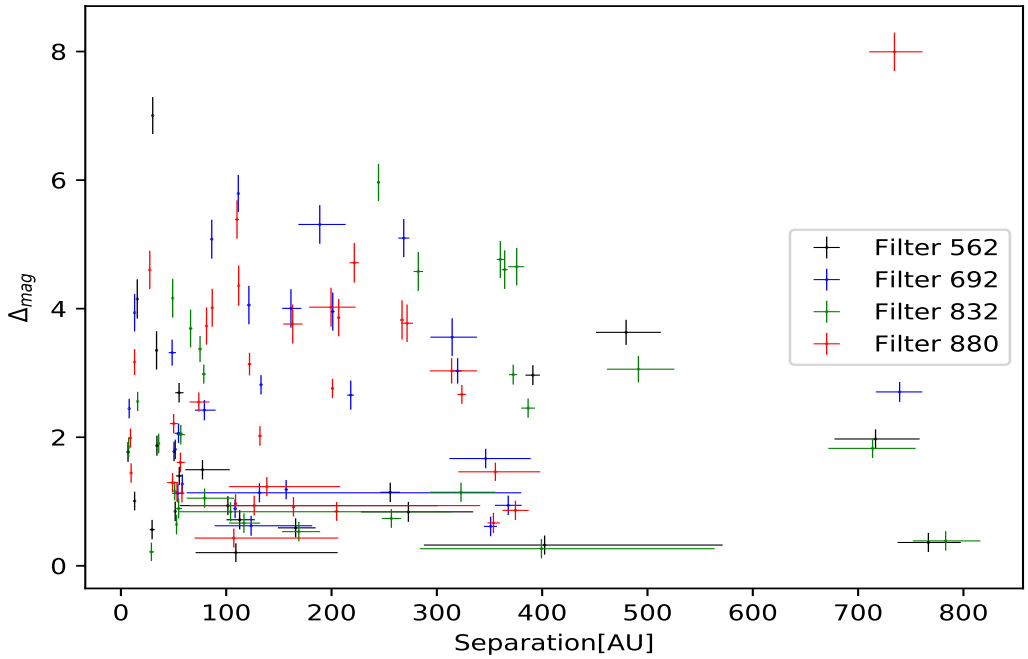

Figure 12: The magnitude difference as a function of the physical separation. The plot is the same as the one in 25 in Appendix A, but here optimized to include values less than 1000 AU so that the clump at short physical separation is easier to see.

Figures 13 and 14 are plots of the physical separation as a function of the distance to the system. Staring with the empty region to the left, large separations and closer to us, which is explained by the limitations of speckle imaging; larger physical separation at small distance from us means larger angular separation, the upper limit is set at $1.2''$. The empty region extends down to roughly 400 AU in the physical separation and roughly 600 pc in the distance from the solar system. Within this region there are also values that correspond to too small angular separation to be resolved by speckle imaging; close by and compact stellar binaries. Furthermore, there is an empty region to the right, see Figure 13, which is also due to the limitations of the method. It is difficult to observe and resolve systems at such large distances, the stars will be too faint or the angular separation will be too small. This difficulty is reflected in the errorbars of the few systems that were resolvable at large distances. Nevertheless, in a positive note, the errorbars for systems closer to us are on average quite small in both measurements.

Looking at the optimized plot, see Figure 14, at first glance the measurements seem to be spread out. But looking at the errors we can see that those measurements at distances larger than 600 pc (specifically those with smaller physical separation) have large errors.

That means that those points could be at smaller distance from us, as indicated by the errorbars. If those values are at smaller physical separation, we can then see a somewhat linear correlation between the properties, which most likely shows how speckle imaging works. We detect stellar binaries with short physical separation if they are close to us and larger physical separation if they are further away. Because the further away the smaller will the angular separation be (lower limit for speckle imaging is at 0.02″ for good observing conditions). Therefore, at distances further away stellar binaries must have larger physical separation, which results in a large enough angular separation to be resolved.

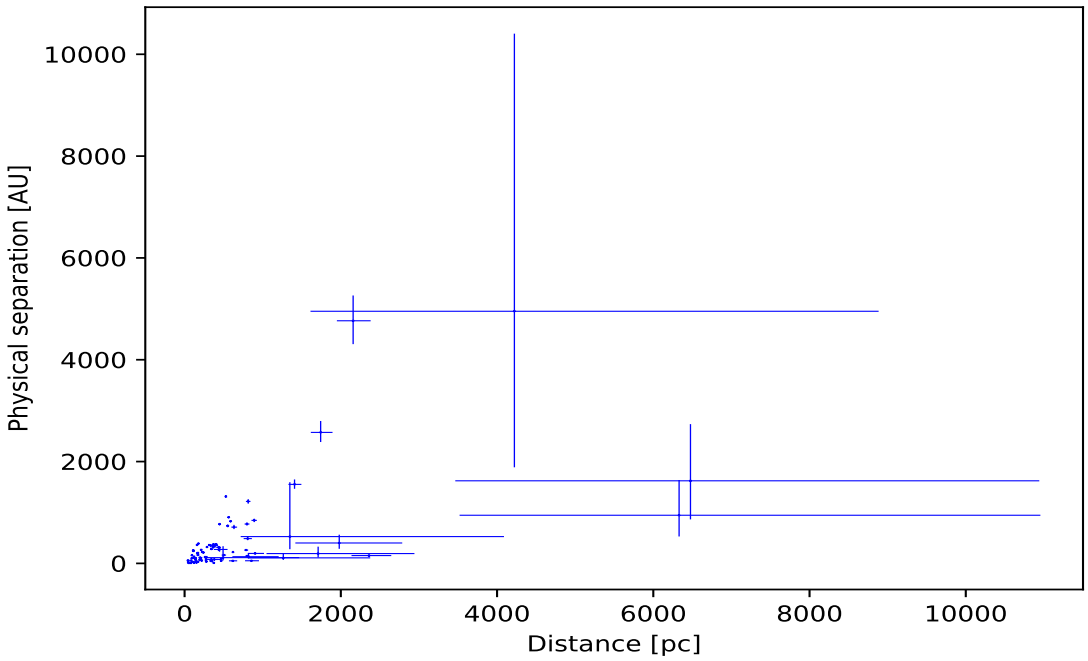

Figure 13: The physical separation as a function of the distance to the system. The plot shows the distribution of the physical separation at different distances and the quality of the measurements.

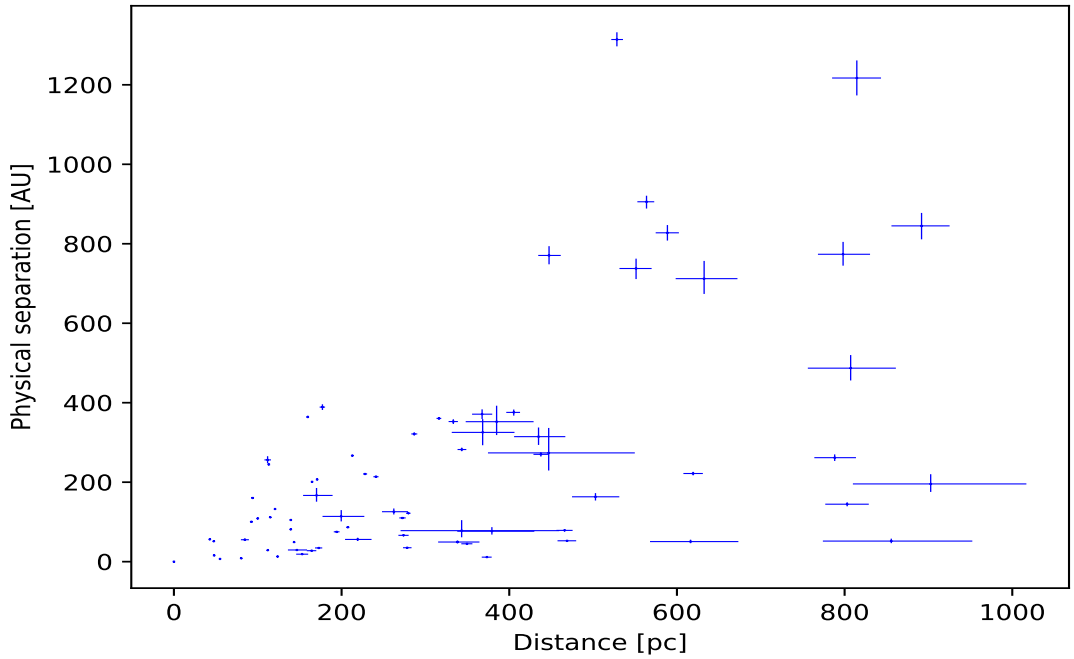

Figure 14: The physical separation as a function of the distance to the system. Showing distribution of the physical separation at different distance to the system. Note that this plot has been filtered to only include the range of shorter distances to the system with errors less than 200, in order to view the clump of points better.

Figure 15 presents a histogram for the physical separation in units of AU. Where the lower plot is in logarithmic scale which roughly follows a Gaussian fit (to see the fit refer to Figure 28 in Appendix A). The histograms are colour coded by filter in order to illustrate all points in each filter, although, note that some systems exist in more than one filter so there are not so many systems in total as it might seem from these plots. Moreover, some systems which do have enough data to find the physical separation but not the masses are not included in this figure (a plot where all systems are included is instead shown in Figure 27 in Appendix A). There are 88 unique systems for which the physical separations was found and only 72 for which the other properties were also calculated. It is clear from the upper plot in Figure 15 that the secondaries detected are usually closer than 400 AU to their primary, with a peak at roughly 160 AU. When including all the 88 systems for which the physical separation is known, the peak is then roughly at 166 AU, see the lower plot in Figure 27.

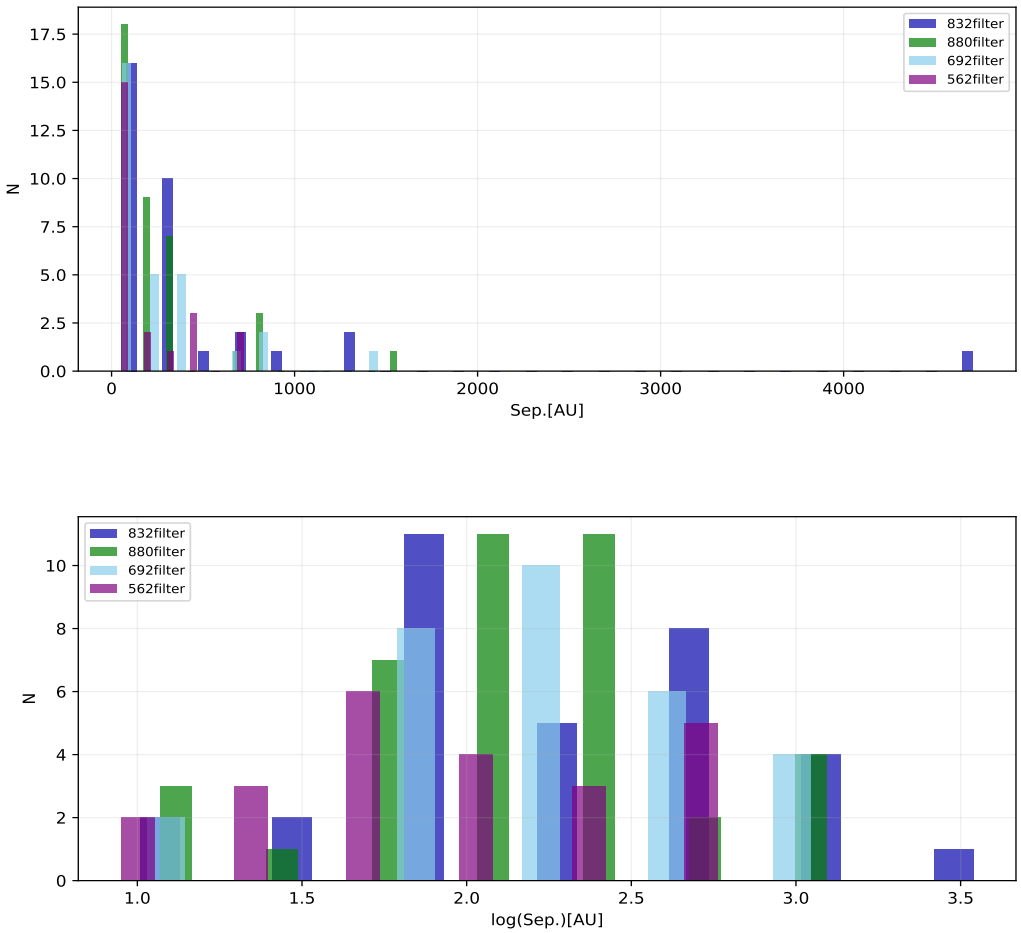

Figure 15: A histogram of the physical separation and its logarithm. The logarithm plot shows the spread of all values better. In the regular plot some values are much larger, making it harder to see most of the points that are within 2000 AU.

Figure 16 shows a histogram of the orbital period. In a similar way as for the physical separation the upper plot shows the extend of values. Since this plot is in days the values are much larger, however, the trend is similar: Most points are within $0.25 \cdot 10^7$ days, i.e short orbital periods, which correspond to smaller physical separation and are thus easier to detect. Putting the data from all the filters together, taking an average for those systems that have been observed in more than one filter, thus include only unique systems, gives a peak at 1430 years. This plot is in days in order to be able to compare directly to Raghavan et al. (2010) (see Section 5). A plot in units of years can be found in Appendix A, Figure 33. That plot shows that the orbital period ranges from as short as 17 years to 40000 years. The orbital period reflects the physical separation between the components. The more compact the binary is the shorter is the orbital period.

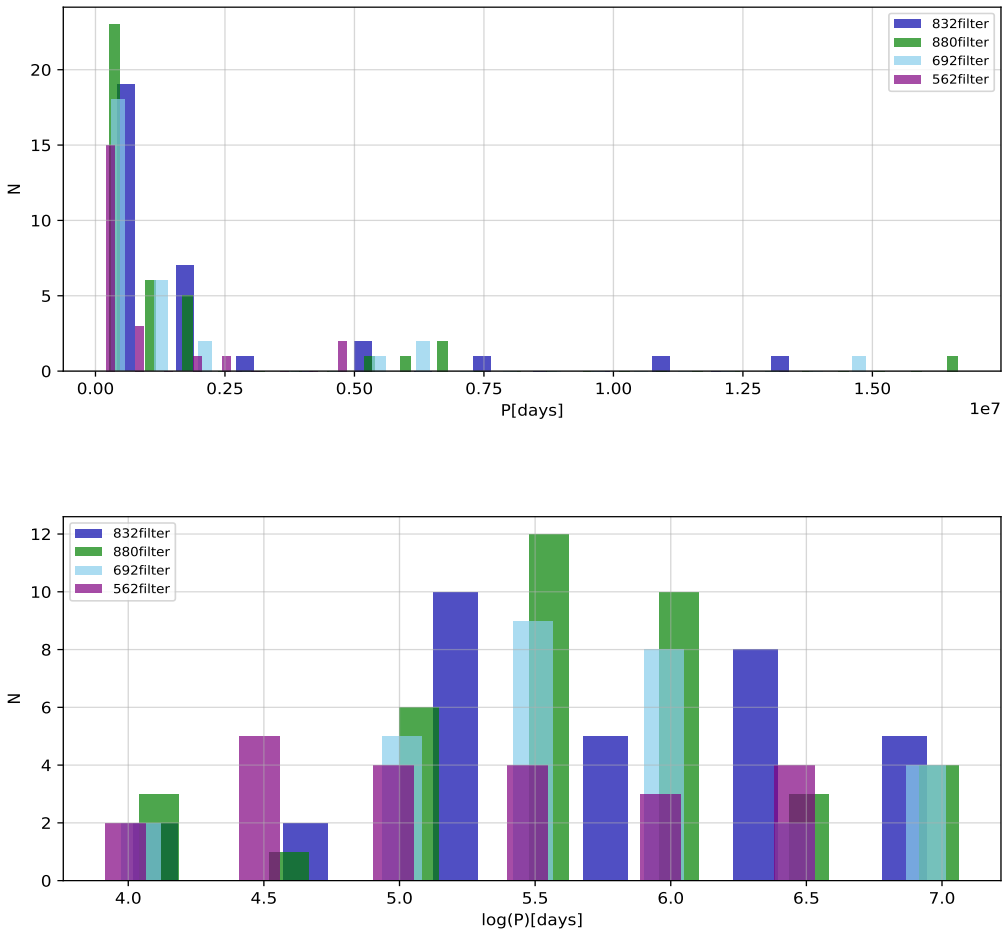

Figure 16: A histogram of the orbital period and its logarithm, in units of days. The logarithm plot shows the spread of all values better whereas the regular plot shows the extend of values. Most points are within $0.25 \cdot 10^7$ days.

The plot in Figure 17 shows the distribution of the mass ratio as a function of the primary mass. The shape of the distribution is spread over the whole graph in both axes, which is as expected, we have not selected stars with any particular mass range. The mass ratios range from 0.3 to roughly 0.9 and the masses from 0.4 to 1.9 solar masses. Again the respective filters follow the same shape of distribution, none of the filters give any different results or outliers. However, the filter K results from the aperture photometry, do differ from the filters used in speckle imaging in some cases. These points are at the left end of the graph in purple; at lower primary mass and larger mass ratio. These measurements seem to be of those systems that had stellar components of almost equal brightness resulting in similar mass or were difficult to see in the image, thus difficult to determine the center of the two light sources in the image. The aperture photometry was

done in order to check the masses found from speckle imaging data with another method, and is explained in Appendix C.

Furthermore, there are eight points in a band below the clump of points, which could be results from observations with good conditions. Better conditions means that systems with larger magnitude difference or smaller angular separation or a combination of both are detectable unlike in other observing runs when conditions are less good. That turned out to be exactly the case for these eight points, they have either a large magnitude difference or a small angular separation and were observed at very good observing conditions.

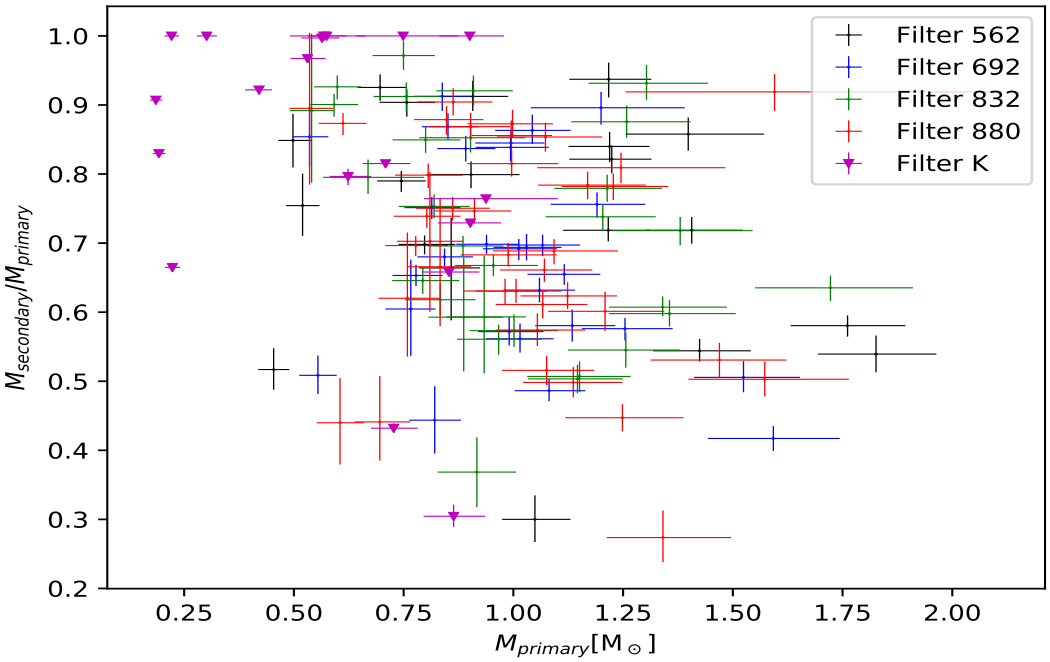

Figure 17: The mass ratio as a function of the primary star mass in the binary. This plot also includes the results from aperture photometry in the K-band, see legend.

The last figures of properties are Figures 18 and 19 where the mass ratio is displayed as a function of the orbital period. These plots show simple trends that agree with other papers such as Winters et al. (2019). That is, for shorter orbital periods there are values of the mass ratio from 0.3 and larger (see Figure 19, the zoomed version). However, for the points at longer orbital period the mass ratio is consistently large, this is clearly visible in the first plot. Those systems have larger physical separations. The formula used to find the orbital period includes both the masses of the two components and their physical separation; we see that larger mass ratio means shorter orbital period unless the physical separation is much larger, increasing the orbital period. Moreover, when the physical separation is small, as in some cases, then the range of the mass ratio can have a wide range of values and still result in a shorter orbital period. Furthermore, as a last

comment on the results; it is consistently visible in all plots, that systems with larger physical separation, or at large distance from us, or small mass ratio and large distance, or faint and small secondary, are harder to detect and study. Therefore, these are at a lower frequency in this sample and most other samples from imaging surveys, perhaps this will change somewhat with new and improved instruments such as Zorro.

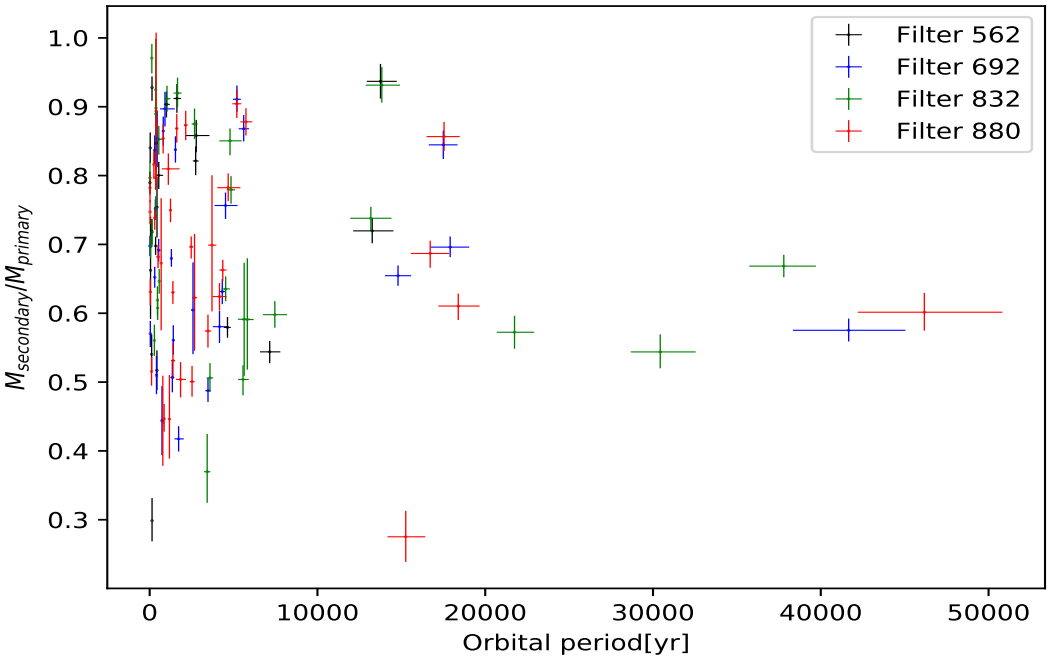

Figure 18: The mass ratio as a function of the orbital period. Colour coded according to filter used for the observation, see legend.

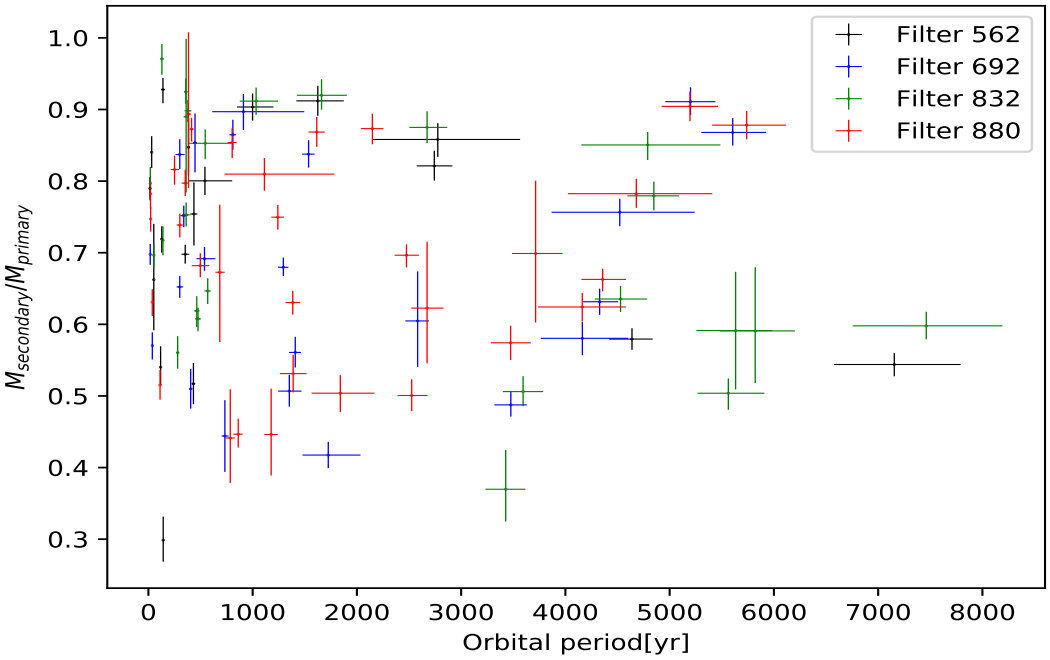

Figure 19: The mass ratio as a function of the orbital period. Same plot as the one above, but here the plot has been optimized in the x-axis, in order to give a better view of the range $0<P<1000$ where most points are.

5 Discussion and conclusion

5.1 Bound systems and fractions

It is difficult to determine which of the systems are actual binaries. An attempt as done here is to use a plot of the angular separation and the magnitude difference. According to other studies such as Matson et al. (2018) systems within $0.4''$ are likely bound and treated as such. For a more careful study of all systems even those outside the limit of $0.4''$, which could still be bound, one can apply stellar isochrones to see if one common isochrone goes through both the primary and the secondary, but that is outside of the scoop of this project, for details refer to for example Everett et al. (2015).

In this project the results from the plots in Figures 9, 10 and 11 will be satisfactory and the fractions found will be compared to Raghavan et al. (2010), Horch et al. (2014) and Matson et al. (2018). The two later ones are studies of Kepler and K2 exoplanet candidate host stars, respectively, similar to this project. The fraction of potential binaries found in this project for speckle imaging observations during 2016-2018 is 14% (100 binaries out of 690 unique observations) which agrees with Horch et al. (2014) and Matson et al. (2018). If we then look at the telescopes separately, because the telescope mirror determines the minimum angular separation resolvable and how faint the secondary can be. At Gemini the mirrors are larger, thus the minimum angular separation resolvable is smaller than at WIYN and the detection limit on the magnitude difference is larger, making it possible to detect more companions. Thus we expect to find more companions at Gemini than at WIYN, which is reflected by the fractions of binaries found in Section 4. The fractions from the papers we want to compare to are: $23 \pm 5\%$ for Gemini and $6 \pm 2\%$ for WIYN in Matson et al. (2018). Excluding any observations outside the limit curve they found fractions of; $19 \pm 5\%$ for Gemini and $5 \pm 2\%$ for WIYN, which are consistent with their simulated fractions, $24 \pm 7\%$ for Gemini and $8 \pm 3\%$ for WIYN. Horch et al. (2014) determine the fractions $22.8 \pm 8.1\%$ for Gemini and $7 \pm 1.1\%$ for WIYN after excluding observations outside the limit curve, with simulated fractions of $19.7 \pm 0.4\%$ for Gemini and $7.8 \pm 0.4\%$ for WIYN. Both papers thus agree. The fractions extracted in my project also agree within the uncertainties with both papers. Furthermore, since their simulations, which are based on the total binary fraction of $44 \pm 9\%$ for Gemini and $40 \pm 9\%$ for WIYN, based on findings in Raghavan et al. (2010), give the fraction for each telescope that agree within the uncertainties with the observed fractions in both papers and those found in my project. One can confidently say that the stellar binary fraction for K2 exoplanet host stars outside the solar neighbourhood (> 25 pc) is in the range $40 - 50\%$, which is consistent with the results in Raghavan et al. (2010); the study of the solar neighbourhood.

5.2 Discussion of the method

In this part the different aspects of the method used for finding the properties will be discussed shortly. Furthermore, short remarks on improvements for speckle imaging will be mentioned.

The method used for finding the properties was chosen according to examples in other papers that have been shown to work or that were the only possible choice with the limited information about the sample. The method included some valid and necessary assumptions and approximations, which means all the properties found in this project are estimates of reality.

The main general point to make about the method is about the errors. The first thought was that the errors would be large and get larger the more complex the calculations became, since more uncertainties were involved. Complex in the sense that more equations with their own uncertainties were used. This was a worry specifically for the mass calculations; for example for the data in the 562 filter the calculations were directly in the visual band with fewer variables thus less error accumulation. Whereas for the other filters especially the filters 832 and 880, there were more steps and equations involved with each errors of their own accumulating to larger errors. However, this does not seem to be the case, the errors for not just the mass, but all the properties seem small. The quality of the estimated properties (size of the error bars) appears more to depend on the limitations of the speckle method and the conditions/quality of the individual observing runs rather than the calculation method.

This is on second thought reasonable, even though it was not an optimal method to use when it comes to specifically the masses. Because all extra equations to find the visual apparent and the visual absolute magnitude came from well established magnitude conversion relations based on years of observations and were suitable for our stars. Moreover, the MLR, which also had uncertainties of their own, were well established and appropriate for the sample as well. Moreover, all those errors were taken into account and properly propagated through the calculations. Thus a more complex method with many more steps should in itself not dramatically increase the size of the errors, the size depends more on the observation quality and the observation technique. For example the further away the systems or the fainter the stars are, the harder it is to study them. Moreover, the poorer the observing conditions, no matter if the stars are faint or far away, the less reliable will the results be. This is what we see in general in all the plots. Nonetheless, as comparisons to papers of similar studies, as done above and as follows below, show that the results of this project are reasonable and useful for future reference.

In the future a better method for finding the properties can be stellar isochrones as done in papers such as Everett et al. (2015). If the information is as limited as in most cases in this sample or one wants to use something other than stellar isochrones,

a similar but better way to find the properties could be to use MLR as done here, but find a relationship for the filters. Such a relationship between the filters used in speckle imaging and the regular filters, such as the SDSS system, can then be used directly to find the individual visual apparent magnitudes instead of going through many conversion formulas. Moreover, we avoid assuming what regular magnitude band the filters used in speckle imaging roughly correspond to.

As for the speckle observation method, it is already an impressive and useful high resolution imaging method, which makes it possible to study and detect close companions that no other method is better at. However, it needs to be sensitive to even more compact binaries and larger magnitude differences, fainter companions. When that is possible multiplicity studies of stars as this one, corrections of planet radii and detection of false positives will be even more effective and accurate.

Moreover, choice of band-width is an important part of improving speckle instruments. A wider band-width makes it possible to observe fainter targets. However, it is a balance between wider band-width and increased atmospheric dispersion. The later also depends on the size of the telescope mirror, for a smaller mirror, wider band-width works better and can even be necessary. For bigger telescope mirrors however, wider band-width can only be used at low airmass if dispersion is kept low (Horch et al., 2012), but this is challenging since it is hard to build in many different filters of different band-widths in the same instrument. Another improvement would be to observe at even shorter wavelengths since the resolution power of a telescope depends on both wavelength and mirror diameter. Nevertheless, speckle imaging can be improved in other ways in the future as technology continues to evolve, making for example new more sensitive cameras available.

5.3 General conclusions from results

In this part some general comments on the results will be given.

Firstly, it is useful to look at the different filters and see if the resulting properties match across the filters. Tables for each property where each system is treated filter wise were made and can be found in Appendix E. For the masses a column with the K-band aperture photometry results has been included.

Starting with the mass tables, the first thing to note is that most systems have been observed with only two filters, which is how speckle imaging observations usually are done. Only four have measurements in all the filters and a few in only one filter. Moreover, remember that the filters come in the sets 562 and 832, 692 and 880, which is just how they are used when observing with speckle imaging. From the table of the mass of the primary star, Table 18, it is clear that in most cases the results match well or at least agree within the uncertainties. There are exceptions to this, for example system 2121381198 was observed in all the filters where 562, 692 and 832 match within the uncertainties but not

880. This is most likely due to observing conditions, that results in worse estimates of the speckle parameters in one filter than the other. The same reasoning applies to other cases where the results do not match even within the uncertainties or between, for example, the filters 562 and 832nm which are used simultaneously. Because the atmosphere behaves slightly different for different wavelengths or the secondary is fainter in one wavelength than the other; both cases result in not equally good images in both of the filters even if they were used simultaneously. This reasoning is enforced by looking at the detection limit curve for that observation and filter; smaller maximum magnitude difference detectable than 3-4 magnitudes, which is usual for speckle imaging, means worse conditions thus worse results. According to the points made here and in the previous subsection and taking into account the good agreement with other papers, the method used for calculating the properties does not seem to be a significant reason for disagreeing results across the filters. Therefore, this confirms further that the assumptions, the approximations and the overall approach in this project is acceptable. The same conclusions can be made for the other two mass-tables, of the secondary mass and the mass ratio, Tables 19 and 20.

Looking instead at the filters compared to the results from the aperture photometry, there are more disagreements. Firstly, it is worth noting that in most images from AO observations, to be used for the photometric study, the secondary was not visible making those images not usable. For those images that aperture photometry was performed, many disagree with the results from the speckle imaging data. At a closer look these were systems that had images where the secondary was barely visible in SAOImageDS9 and not at all visible on the Python plots of the image, making it difficult to give acceptable guesses of the center of the secondary, which was done manually. This is also the most likely explanation for the shape of the K-band results plotted in Figure 17; the points disconnected from the rest. As mentioned in Appendix C this could be solved using the position angle from speckle imaging observations to find the location of the secondary. But aperture photometry was an extra step only used to quickly check the masses, thus not important enough to look further into. Overall the results from aperture photometry show that when the images work the results agree within the uncertainties with the masses found from speckle imaging data. Having the two methods, which are different, agree in general is important, because that further strengthens the reliability of the method used to find the masses via speckle imaging data.

The same type of conclusions can be drawn and the same behavior is seen in the other sets of tables for the last two properties, the physical separation and the orbital period. Note that these properties were not estimated using the mass-results from K-band photometry, therefore such a comparison does not exist. Nevertheless, the comparison across the filters used in speckle imaging observations shows the same results as for the mass tables. There are mostly agreement within the uncertainties, as there should be since the only difference is the filter used, not the method of observation. However,

disagreements exist which are again most likely due to worse observing conditions and the same reasoning as mentioned above. In observations with bad seeing and windy weather, conditions can change significantly in a short time causing images to be worse in one case or filter compared to another.

More detailed discussion about each property and graph will follow below in Subsection 5.4 where the results are compared to Raghavan et al. (2010). However, looking in general at the plots, all of the properties seem reasonable and have a distribution as expected and seen in other work.

One last noteworthy general comment to make here is about the physical separations of the systems. Papers such as Kraus et al. (2016) have suggested, by looking at a sample of Kepler/K2 exoplanet host stars, that there is a suppression of companions with physical separations < 50AU for exoplanet host stars: There cannot exist such a close companion if there also is a planet, or in other words no planets can form in compact binaries where the physical separation is less than 50 AU. This was investigated in Matson et al. (2018) too, they could not find any such indications. Same as in those papers the sample of my project is considered to consist of exoplanet host stars. Looking then at the histogram plots of the physical separation in Figure 20, where the physical separations range from 0-300 AU with bin size of 12 AU (to the right) same as in Matson et al. (2018) (see their plots in figure 9) and 0-1000 AU (to the left) same as in Kraus et al. (2016) (see their plots and arguments in figure 7).

It is clear that there is no indication of any suppression in either of the plots. Moreover, unlike the Matson et al. (2018) paper, which only had 26 systems with detected companions, there is a large enough number of companions in my sample (100 primaries with one companion) to be able to say more confidently, that there is no such indication. However, same as for Matson et al. (2018), until all the binaries in this project have at least one confirmed exoplanet the statement in question from Kraus et al. (2016) cannot be properly disproved.

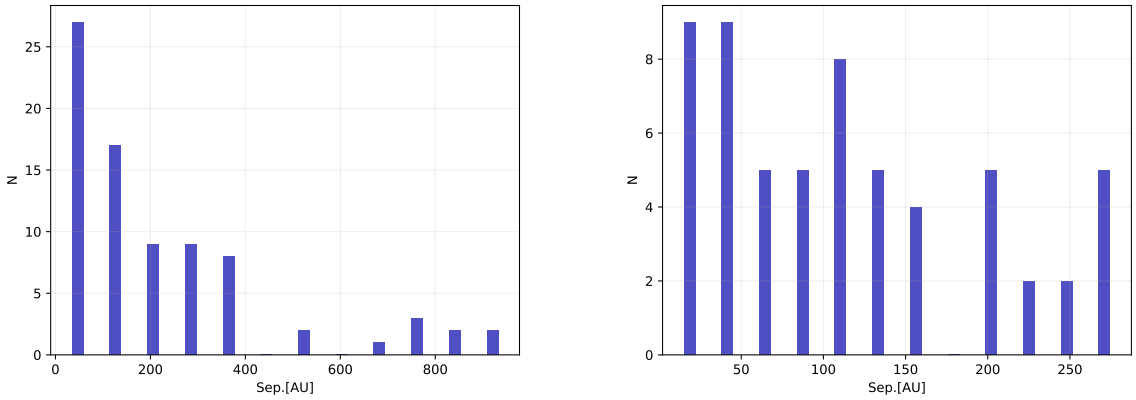

Figure 20: These two plots are a zoomed in version of the physical separation histograms shown in earlier sections and in appendices. The left one includes separations out to 1000 AU, while the right one shows separations up to 300 AU.

5.4 Comparison to Raghavan et al. (2010)

The long held belief that most stars are not born as singles was put to the test by multiplicity studies such as the one presented in Raghavan et al. (2010). That study used observations selected from the Hipparcos catalog, a sample consisting of 454 primary solar-type stars within 25 pc from the Sun, i.e the solar neighbourhood. The sample consists of stars on the main sequence (see figure 1 in the paper for their selection criteria), however, the type of stars are F6-K3, solar-type stars, unlike the sample in this project which also includes M-dwarfs and more K-dwarfs. Nevertheless, it will be an interesting comparison in terms of multiplicity and distribution of properties. Furthermore, the sample in Raghavan et al. (2010) was shown to be a complete sample for the distance out to 25 pc from the Sun with no magnitude limits, making it a useful paper to compare with. In Raghavan et al. (2010) different methods of finding the companions were used and for some stars they also used speckle interferometry. These different methods also serve as support for confirming companions, which is possible to do confidently for their sample, since those stars are nearby stars. In Raghavan et al. (2010) they extract most of the properties from many discovery sources. Thus the methods were not the same in the paper as used here.

Starting with the fraction of type of systems, in Raghavan et al. (2010) the following was found: single star systems are at $56 \pm 2\%$, binaries at $33 \pm 2\%$, triple star systems at $8 \pm 1\%$ and lastly higher order systems were found to be at $3 \pm 1\%$. The Raghavan et al. (2010) paper thus shows that in the vicinity of the Sun most systems consist of single stars. While the fraction for binaries is lower, but not by much. In the sample of my project out of all the systems observed with speckle imaging, 690 in total, only 100 systems have a detected secondary. Further, out of these 100 systems 26 are potentially

bound according to the probabilities shown in Figure 9. From these numbers the percentage is 14%, same as in Matson et al. (2018), where they show that using fractions from Raghavan et al. (2010) to simulate predicted fractions, results in fractions (both total and for each telescope separately) that agree within the uncertainties with the fractions found in my project.

As for the properties even though their methods are different all properties in general have similar distributions. Starting with orbital period; in Raghavan et al. (2010) this was presented as a histogram in units of days. Here the orbital period has been presented both in units of days and years; Figure 16 in Section 4 and Figure 33 in Appendix A. Focusing on the distribution in units of days in log-scale in comparison to Figure 13 in Raghavan et al. (2010), we see that the shape is similar and in the same manner roughly follows a Gaussian normal distribution (see Figure 34 for the fit). The differences are the location of the peak and the maximum period. In the paper they choose to show a Gaussian fit, which is not really explained why, but could be just to clearly illustrate or maybe to be able to get the standard deviation of the distribution. For my project the mean and standard deviation was found from the data directly, in log-scale. The peak of the orbital period for my project is at $logP = 5.72$ which corresponds to 1430 years, with a standard deviation of $\sigma_{logP} = 0.78$ corresponding to 0.016 years. This is slightly higher than the peak in Raghavan et al. (2010), which was at $logP = 5.03$ or 293 years.

Looking then at the same figure in the paper (figure 13) they also plot an axis for the physical separation in log-scale. The mean of the physical separation in units of AU was found to be at $\log(a) \approx 1.9$, corresponding to roughly 80AU. Doing the same with the physical separation as with the orbital period (see the distribution in Figure 15 and the Gaussian fit of it in Figure 28) gives a mean at $\log(a) \approx 2.2$ which corresponds to roughly 166 AU with a standard deviation at $\sigma_{\log(a)} = 0.58$ or 3.8AU (including all 88 systems as shown in Figure 27). The peak is thus further out for this study compared to that in Raghavan et al. (2010). Looking at other papers such as Winters et al. (2019) which is a study of only M-dwarfs in the solar neighbourhood, the peak for the physical separation is at 20AU. That does not agree at all with the sample in this project, but that could be since it is for only M-dwarfs. In my project the peak for the physical separation when only including M-dwarfs is lower than for the full sample, at 105 AU, but still much further out than in Winters et al. (2019).

Another study more similar to this project, where they also study stars within 25 pc, believed to have exoplanets and detect companions using speckle imaging, Ziegler et al. (2020). They found wider binaries than in Raghavan et al. (2010) with a peak at roughly 200 AU, which is in better agreement with the results from my project. This could mean that a peak further out simply is a feature of exoplanet host stars in binaries; a difference between stellar binaries in the solar neighbourhood and exoplanet hosting binaries, which

needs further investigation in the future. Furthermore, if the peak for the orbital period is further out so will the peak for the physical separation be, since the orbital period is a function of the physical separation.

A last interesting comparison with Raghavan et al. (2010) is the mass ratio distribution and the mass ratio as a function of the orbital period. Looking at the plot (to the left) in figure 16 in Raghavan et al. (2010), the mass ratio distribution is rather flat for ratios 0.2-0.9, and increasing as we reach ratio one. The same type of plot in Figure 31 shows roughly the same behaviour; the mass ratio increases slightly towards ratios of 1, these are easier to detect, but the increase is more significant than in Raghavan et al. (2010). This can be further investigated in the future with more accurate mass measurements to see if it is consistent and real for stellar binaries outside of the solar neighbourhood. Nevertheless, the overall behaviour is still similar and has been seen in other studies, e.g. Winters et al. (2019).

Looking at Figure 17 in Raghavan et al. (2010) which looks at the mass ratio as a function of the orbital period, it shows a lack of small mass companions. Figure 17 also shows a suggestion that the systems with shorter orbital periods also consist of smaller mass companions. This is seen as a lack of small mass - short period combination of systems, which as mentioned in the paper, is not due to incompleteness or any bias, lack of such companions is real. The same conclusion can be seen in the plots of my project: Figures 18 and 19 show similar distribution, small mass-short period companions are rare, while most systems have the combination short period-large mass. However, it is noteworthy that speckle imaging actually is not very sensitive to such systems, thus the number of those systems might increase with more complete samples and better sensitivity. For now the conclusion is that small mass-short period companions are rare same as in the solar neighbourhood. Moreover, the longer period systems seem to most often correspond to larger mass companions (larger mass ratios), most of them being at mass ratios of 0.6 and larger, exceptions exist but are rare. Furthermore, as mentioned in Raghavan et al. (2010), stellar binaries with like-mass components seem to prefer shorter orbital periods, that seems to be the case here too. However, this is harder to conclude from my results, since those systems are few and there are exceptions; there are systems with a mass ratio at 0.9 and a relatively wide range of periods out to 8000 years. However, there are no systems with a mass ratio above 0.9 and long orbital period.

5.5 Conclusion

In this project the main goal was to analyze systems with detected companions from follow-up observations with speckle high resolution imaging, and for each of these systems find the following properties; the masses of the stars in the system, the orbital period and the physical separation. The many assumptions and approximations associated with the

method used for finding the properties might seem worrisome, but the results from the calculations show trends that agree in general with other studies of similar type and results for the solar neighbourhood. Therefore, one can say with confidence that the method of calculations used in this project works well and can be applied to data from follow-up speckle imaging observations.

By including detection limits and plotting the parameters derived from speckle imaging, the magnitude difference and the angular separation, the fractions of companions detected at each telescope were found. The resulting fractions were 15% for Gemini and 8% for WIYN, which are in agreement within the uncertainties with Matson et al. (2018) and Horch et al. (2014) and their simulated predictions. Moreover, from the same plot a first suggestion of which systems are bound was made; 26 of the 100 are within $0.4''$, thus 99% likely to be bound.

This work also further suggests that there is no indication of suppression of compact exoplanet hosting binaries with separations less than 50AU as stated in Kraus et al. (2016). Furthermore, after having looked at all aspects and properties in detail and comparing to previous works the general trends agree with those papers. Specifically, it is clear that the spread of the orbital period is similar to that of nearby solar-type binaries just with a peak further out, which is within reason and could be a feature of exoplanet host stars in binaries. Further the same can be said for the distribution of the physical separation. Lastly, the mass ratio as a function of the orbital period also agrees with other papers and shows that systems with short period also prefer small mass companions, while systems with long orbital period most often consist of a larger mass companions.

The comparisons in general have shown that the findings from this sample agree well with other studies and are useful for future work. The results will provide hints on what to look for and focus on in future observations. Moreover, the agreement with studies of solar-type binaries, confirms that the same overall trends exist in systems of binaries with planets, outside the solar neighbourhood. Knowing properties such as the mass ratio and the orbital period gives an overview of the type of stars in binary systems that exist out there and helps improve or change formation and evolution models. An important example are very compact binaries ($<$1AU) that are sometimes detected (not present in this sample though), which cannot form that close instead they are examples of stars that formed further apart, but moved close during their life time evolution. Furthermore, those same properties give clues about the formation of planets in stellar binaries that need to be studied in detail in the future.

In conclusion, the overall trends and distribution of the properties, specifically compared to each other, give clues to formation of planets in stellar binaries and hints for improvements of formation and evolution models, and help us understand stellar binaries in general.

6 References

Bailer-Jones, C. A. L., Rybizki, J., Fouesneau, M., Mantelet, G., and Andrae, R. (2018). Estimating distance from parallaxes. IV. Distances to 1.33 billion stars in Gaia data release 2. *AJ*, 156:58.

Everett, M. E., Barclay, T., et al. (2015). High-resolution multi-band imaging for validation and characterization of small *Kepler* planets. *AJ*, 149:55.

Henry, T. J. and McCarthy, Donald W., J. (1993). The Mass-Luminosity Relation for Stars of Mass 1.0 to 0.08M(solar). *AJ*, 106:773.

Hirsch, L. A., Ciardi, D. R., et al. (2017). Assessing the effect of stellar companions from high-resolution imaging of *Kepler* objects of interest. *AJ*, 153:117.

Horch, E. P., Dinescu, D. I., et al. (1996). Speckle Interferometry of Southern Double Stars.I.First Results of the Yale-San Juan Speckle Interferometry Program. *AJ*, 111:1681.

Horch, E. P., Falta, D., et al. (2010). CCD speckle observations of binary stars with the WIYN telescope. VI. Measures during 2007-2008. *AJ*, 139.

Horch, E. P., Howell, S. B., Everett, M. E., and Ciardi, D. R. (2012). Observations of binary stars with the differential speckle survey instrument. IV. Observation of *Kepler* , *CoRoT* , and *Hipparcos* stars from the Gemini north telescope. *AJ*, 144:165.

Horch, E. P., Howell, S. B., Everett, M. E., and Ciardi, D. R. (2014). Most sub-arcsecond companions of Kepler exoplanet candidate host stars are gravitationally bound. *ApJ*, 795:60.

Horch, E. P., Veillette, D. R., et al. (2009). Observations of Binary Stars with the Differential Speckle Survey Instrument. *AJ*, 137:5057–5067.

Howell, S. B. (2000). *Handbook of CCD astronomy*. Cambrige University Press.

Howell, S. B., Everett, M. E., Sherry, W., Horch, E., and Ciardi, D. R. (2011). Speckle camera observations for the NASA *Kepler* mission follow-up program. *AJ*, 142:19.

Howell, S. B., Sobeck, C., et al. (2014). The K2 Mission: Characterization and early results. *PASP*, 126:398–408.

Jordi, K., Grebel, E. K., and Ammon, K. (2006). Empirical color transformations between SDSS photometry and other photometric systems. *AAP*, 460:339–347.

Kraus, A. L., Ireland, M. J., Huber, D., Mann, A. W., and Dupuy, T. J. (2016). The impact of stellar multiplicity on planetary systems. *AJ*, 152:8.

Labadie, L., Rebolo, R., et al. (2010). High spatial resolution and high contrast optical speckle imaging with FASTCAM at the ORM. *arXiv*, page 77350X.

Matson, R. A., Howell, S. B., Horch, E. P., and Everett, M. E. (2018). Stellar companions of exoplanet host stars in K2. *AJ*, 156:31.

Natali, F., Natali, G., Pompei, E., and Pedichini, F. (1994). The use of the (B-I) color index and applications of the (B-I) versus (B-V) relationship I. Open clusters. *AAP*, 289:756–762.

Raghavan, D., McAlister, H. A., et al. (2010). A Survey of Stellar Families: Multiplicity of Solar-type Stars. *ApJ*, 190:1–42.

Scott, N. J., Howell, S. B., Horch, E. P., and Everett, M. E. (2018). The NN-explore exoplanet stellar epeckle imager: Instrument description and preliminary results. *PASP*, 130:054502.

Siegel, A. F. (2016). *Practical Business Statistics (Seventh Edition)*. Academic Press.

Teske, J. K., Ciardi, D. R., Howell, S. B., Hirsch, L. A., and Johnson, R. A. (2018). The effects of stellar companions on exoplanet radius Distributions. *AJ*, 156.

Winters, J. G., Henry, T. J., et al. (2019). The solar neighborhood XLV. the stellar multiplicity rate of m dwarfs within 25 pc. *AJ*, 157:216.

Ziegler, C., Tokovinin, A., et al. (2020). Soar tess survey. i: Sculpting of tess planetary systems by stellar companions. *AAS*, page 55.

Appendices

A More plots

In this appendix I show additional plots.

The first Figures 21, 22, 23 and 24, are the last plots related to the physical separation. They show the physical separation as a function of the mass ratio between the system components and the primary mass, respectively. In both plots the distribution is quite spread out, but also localized to a certain region; there are empty regions to the left and right explained by the limitations of the speckle observation technique: Systems with large physical separation correspond to large angular separation. Most points are at physical separation less than 500 AU and the mass ratio ranges from roughly 0.3 to 0.9. While the primary mass goes from roughly 0.4 to 1.8 solar masses. Moreover, the shape of the distribution is similar in both sets of plots. Most of the systems consist of a brighter and more massive primary and a smaller secondary, with a few exception where the mass ratio is almost one. The distribution of points from the different filters follow the same shape.

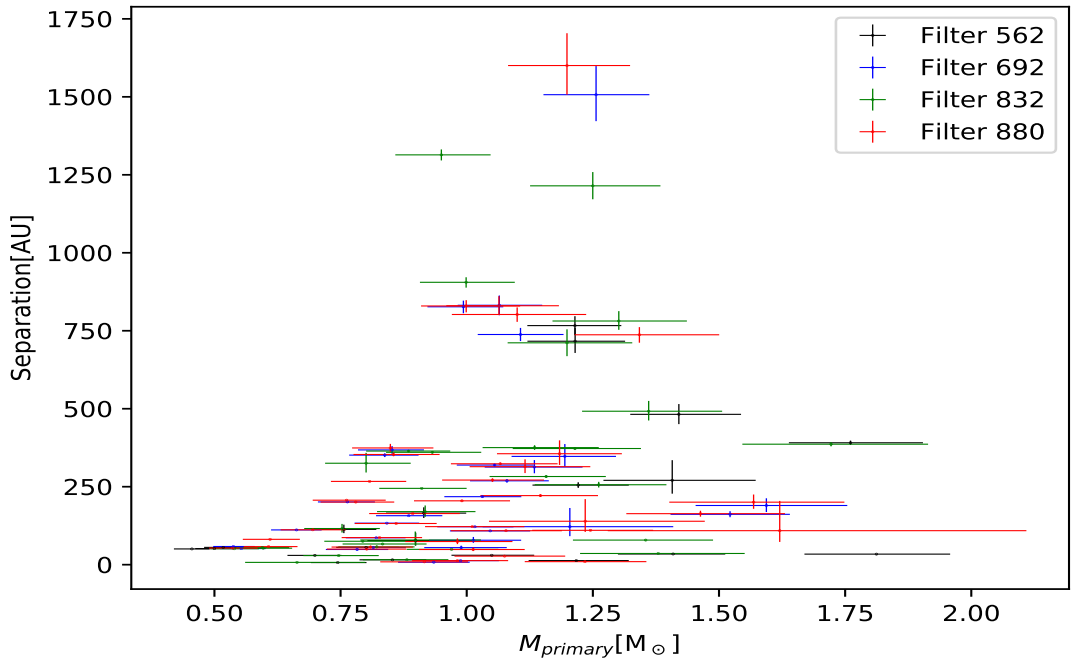

Figure 21: The physical separation as a function of the mass of the primary star in the binary.

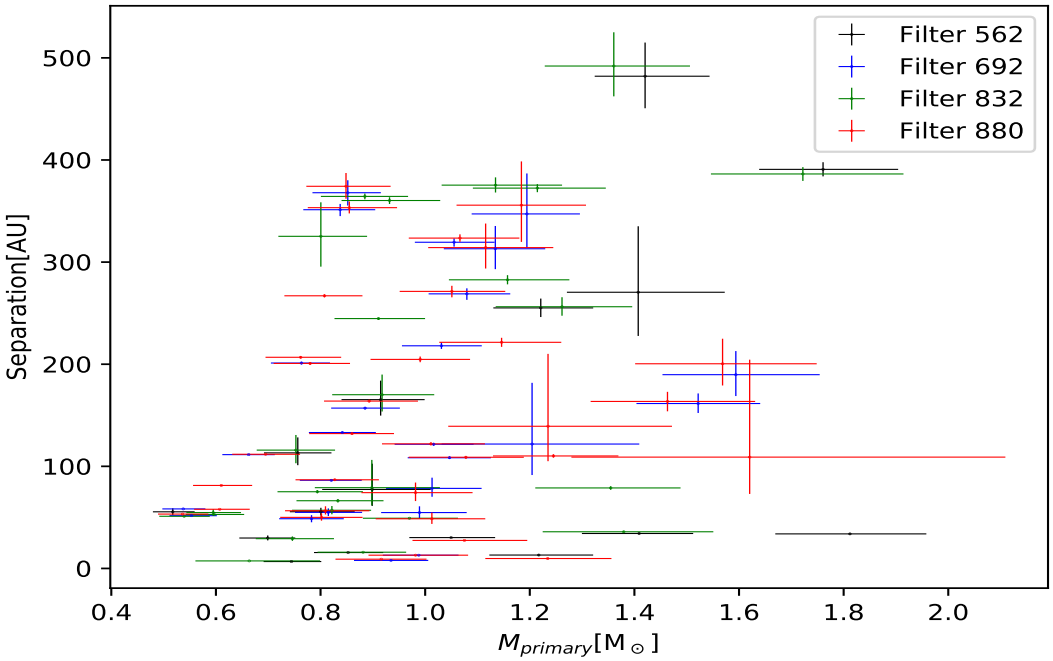

Figure 22: The physical separation as a function of the mass of the primary star in the binary. Giving an idea of how far away from each other stars in a system with certain primary mass are. This plot is a zoomed in version of the same one above, in order to see the clump at smaller physical separation better.

Lastly, looking at these plots we can see a general trend; that is small mass primaries come in combination with larger mass ratio and smaller physical separation, which is also shown in Winters et al. (2019).

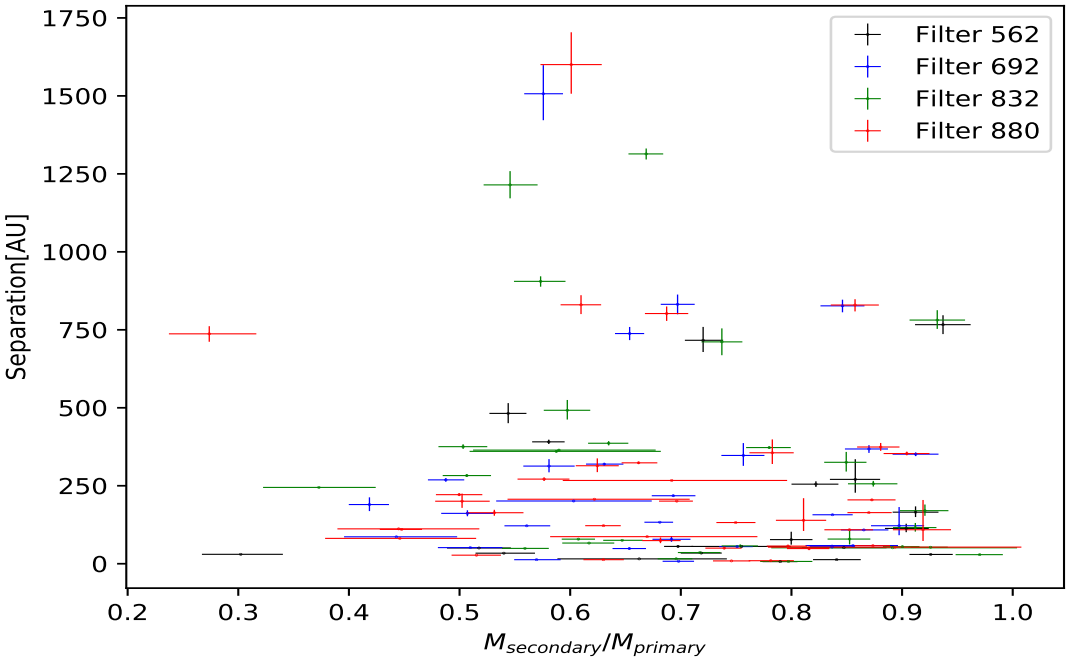

Figure 23: The physical separation as a function of the mass ratio. It gives an idea of how far away from each other stars in a system with certain mass ratio are.

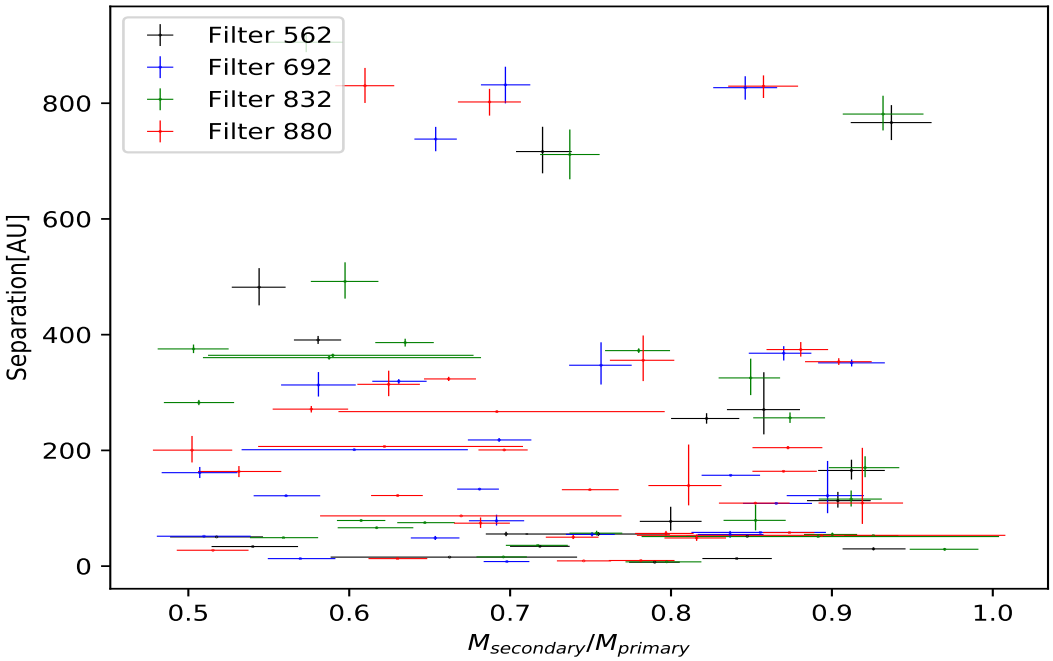

Figure 24: The physical separation as a function of the massratio, but here it is zoomed in to give a better view of the clump of points at shorter physical separation.

Figure 25 shows the magnitude difference as a function of the physical separation in

units of AU.

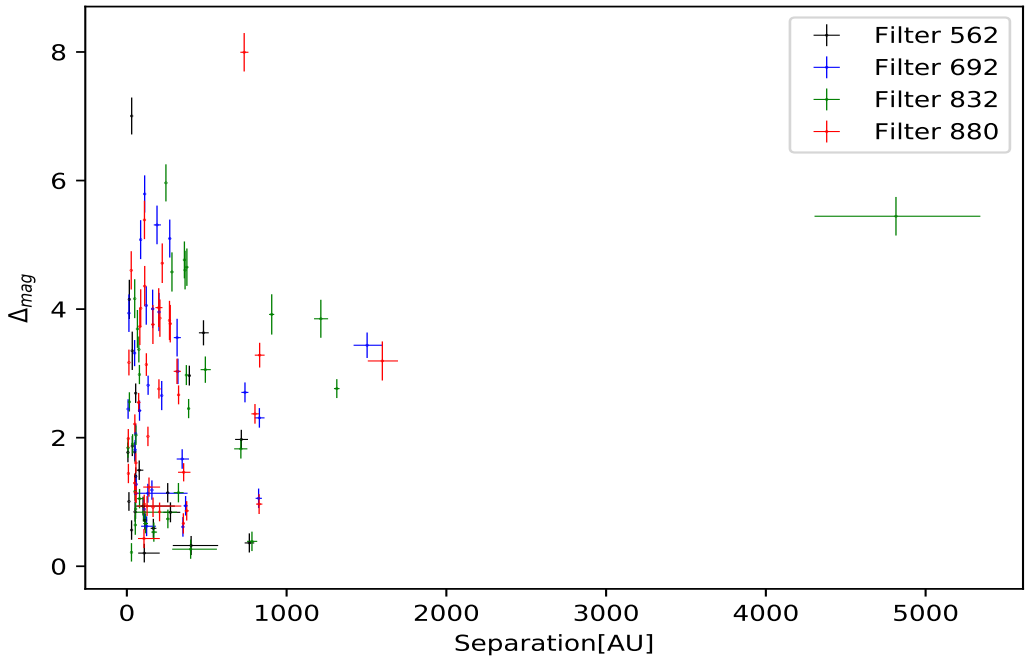

Figure 25: The magnitude difference as a function of the physical separation in units of AU.

The two Figures 26 and 27, show histograms of the physical separation, where the first shows a subplot for each filter to better visualize each filter's distribution. While the second shows the overall distribution for this property without indicating the filter.

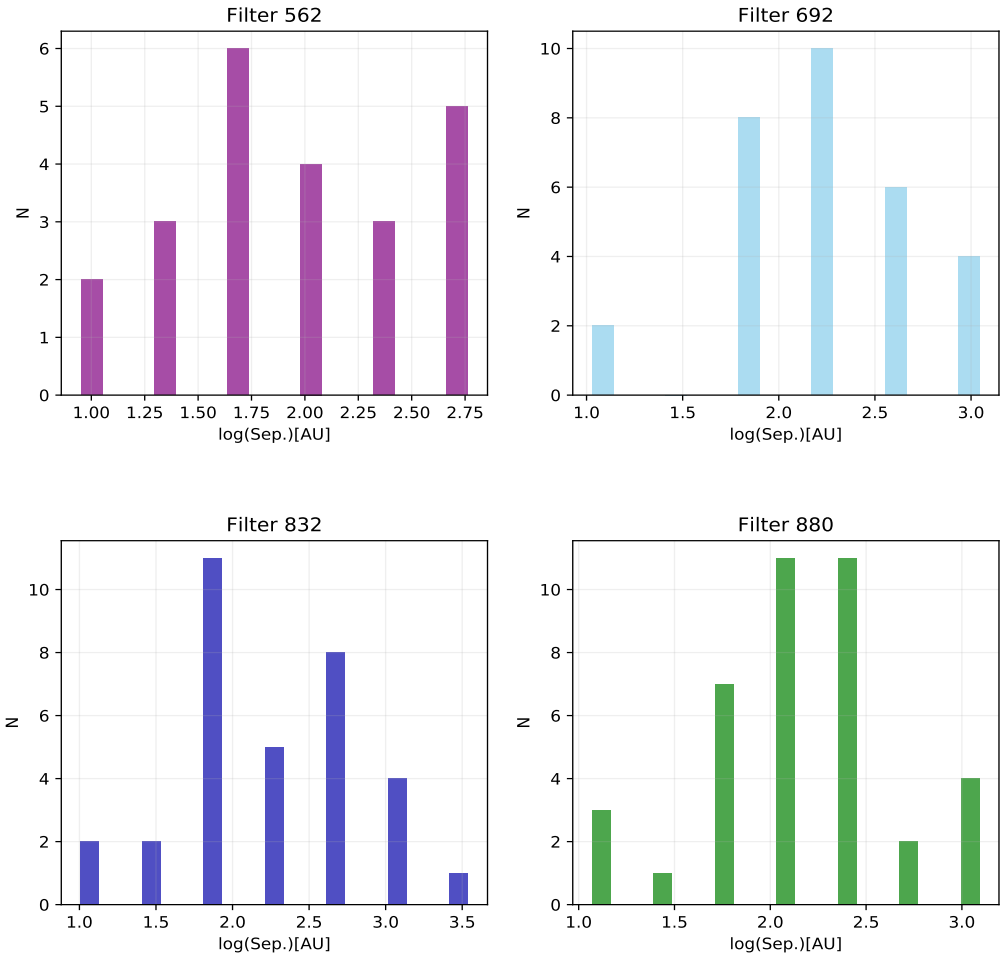

Figure 26: The physical separation as a function of the number of systems where filters are separated into subplots to better demonstrate the distribution of the data from each filter.

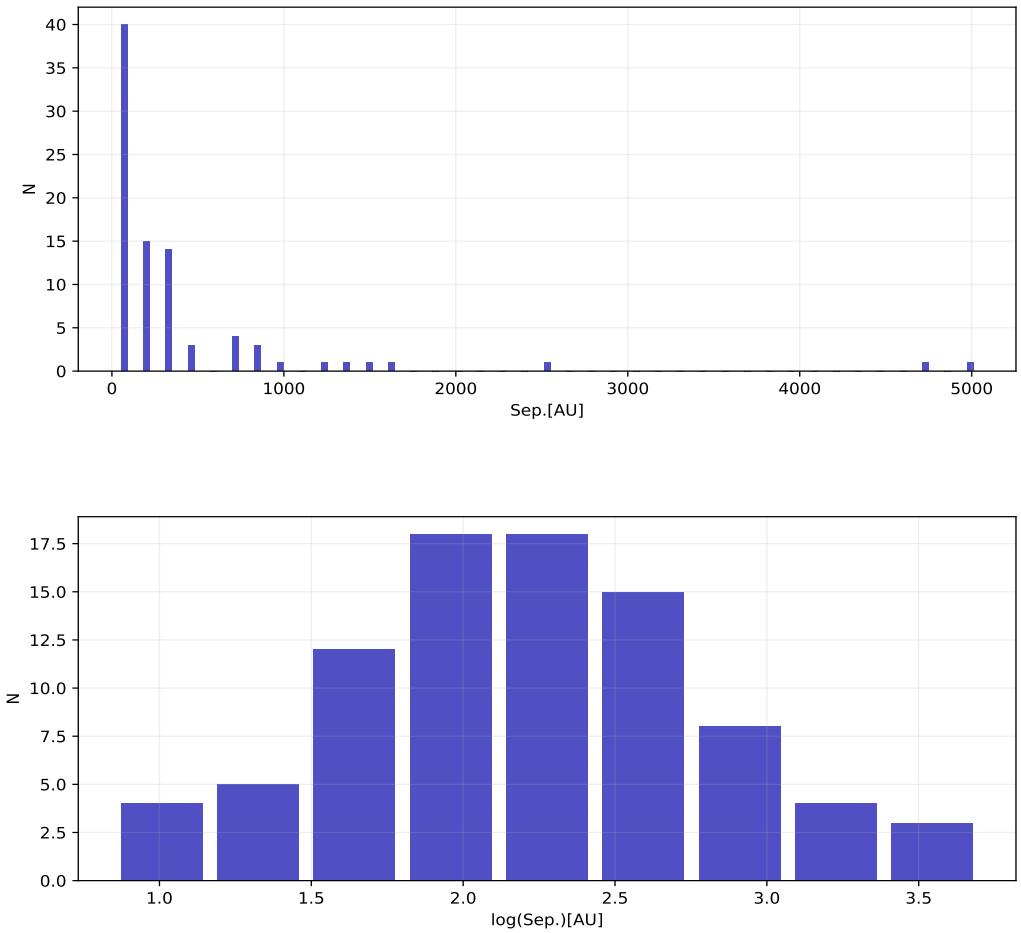

Figure 27: The physical separation as a function of the number of systems, where filters are not given.

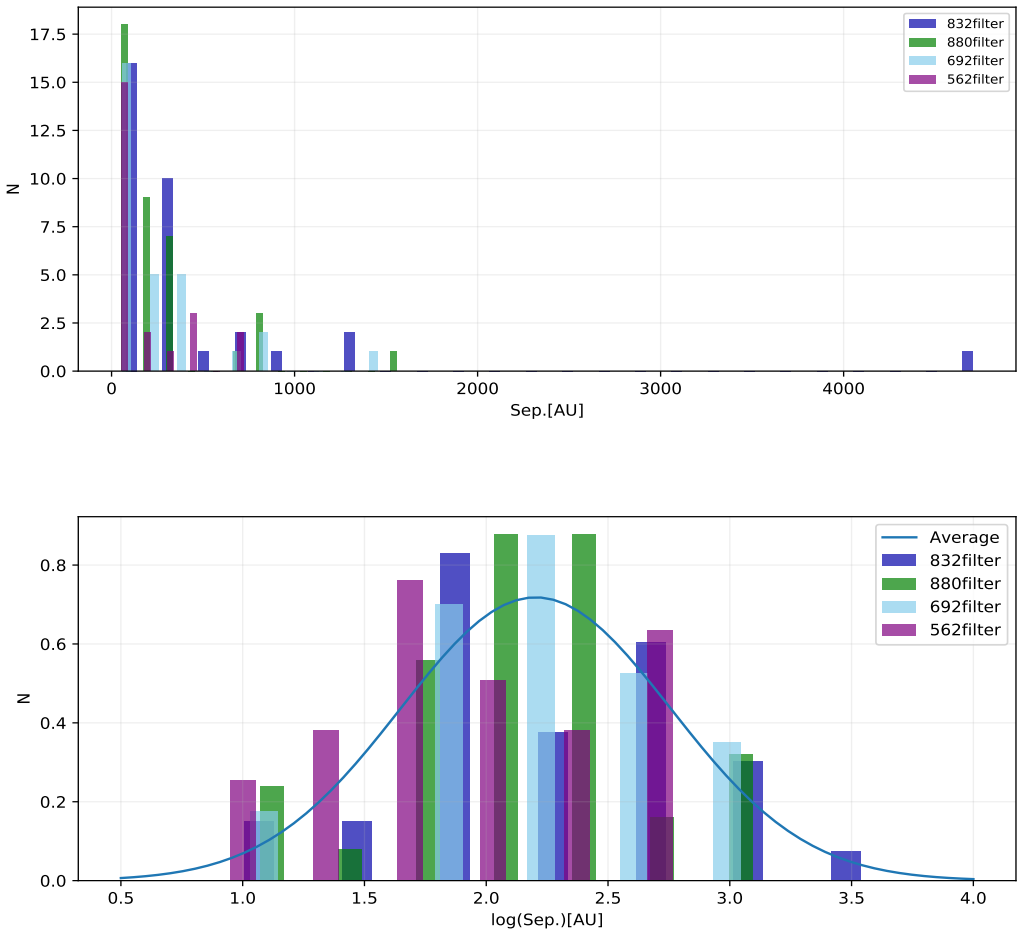

Figure 28: The physical separation as a function of the number of systems, where filters are colour coded as shown in the legend. Note that this plot also shows the fitted Gaussian to be compared to the paper Raghavan et al. (2010), for the method used here to find the fit, the data must be normalized.

The two first figures below (Figures 29 and 30) show the distribution of the primary and the secondary mass in a histogram. These are not important to discuss in Section 5, since nothing new can be said from them, the mass ratio plots are more useful. Nonetheless, these could be interesting to just have a look at.

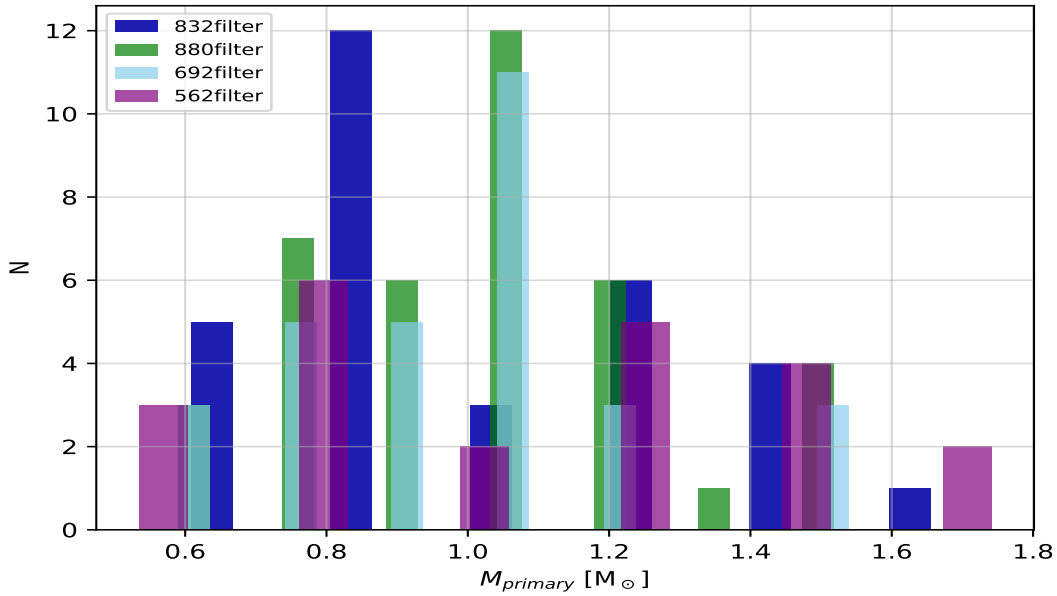

Figure 29: A histogram of the mass of the primary stars in the systems. It is a way of displaying how the primary mass is spread out in the sample.

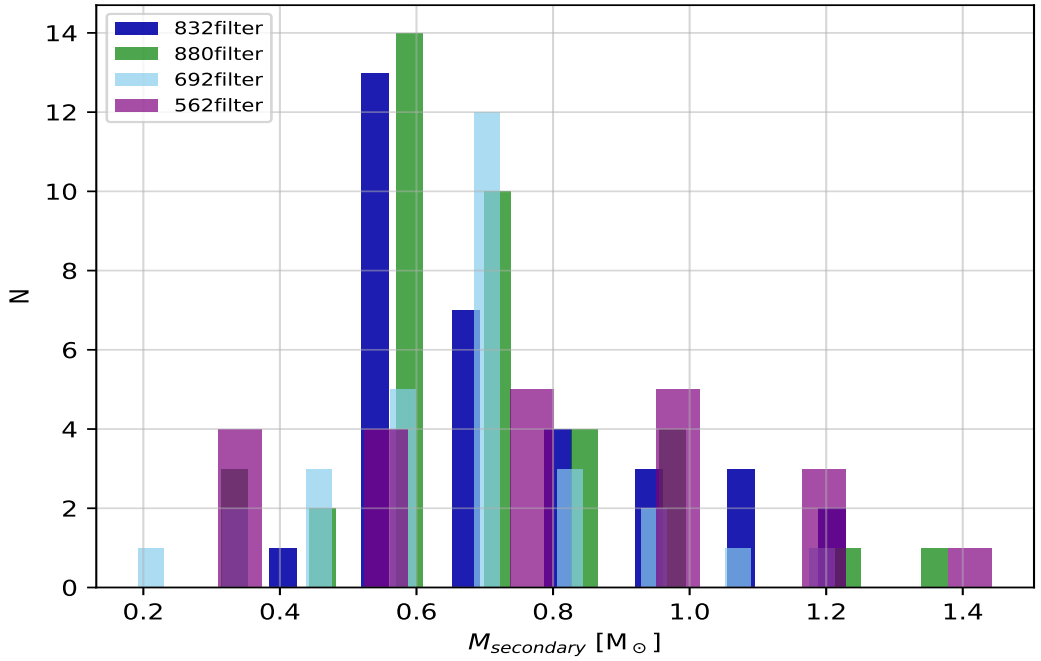

Figure 30: A histogram of the mass of the secondary star in the systems, showing which ranges are more represented.

Figure 32, shows the mass ratio histogram for each filter separately into subplots. This is included here to show clearer how the shape looks like for respective filter, a plot with

all filters in one is shown in Figure 31, where the overall trend is easier to visualize. Even here it is visible that the frequency increases with mass ratio, with the filter 832 being an exception from this (it has a peak at mass ratio of 0.6), possibly due to an outlier in the measurements which is most likely due to worse observing conditions. The number of stars at the peak differs by one compared to the number of stars at ratio of one.

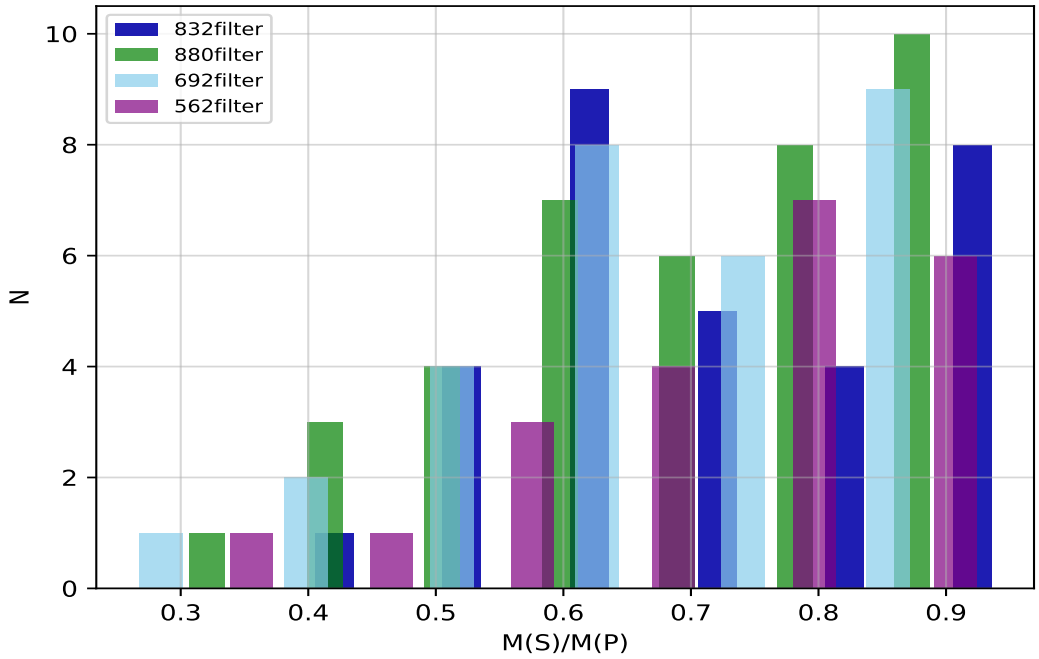

Figure 31: A Mass ratio histogram where the filters are colour coded, see legend. It is a way of displaying how the mass ratio is spread out in the sample across the filters.

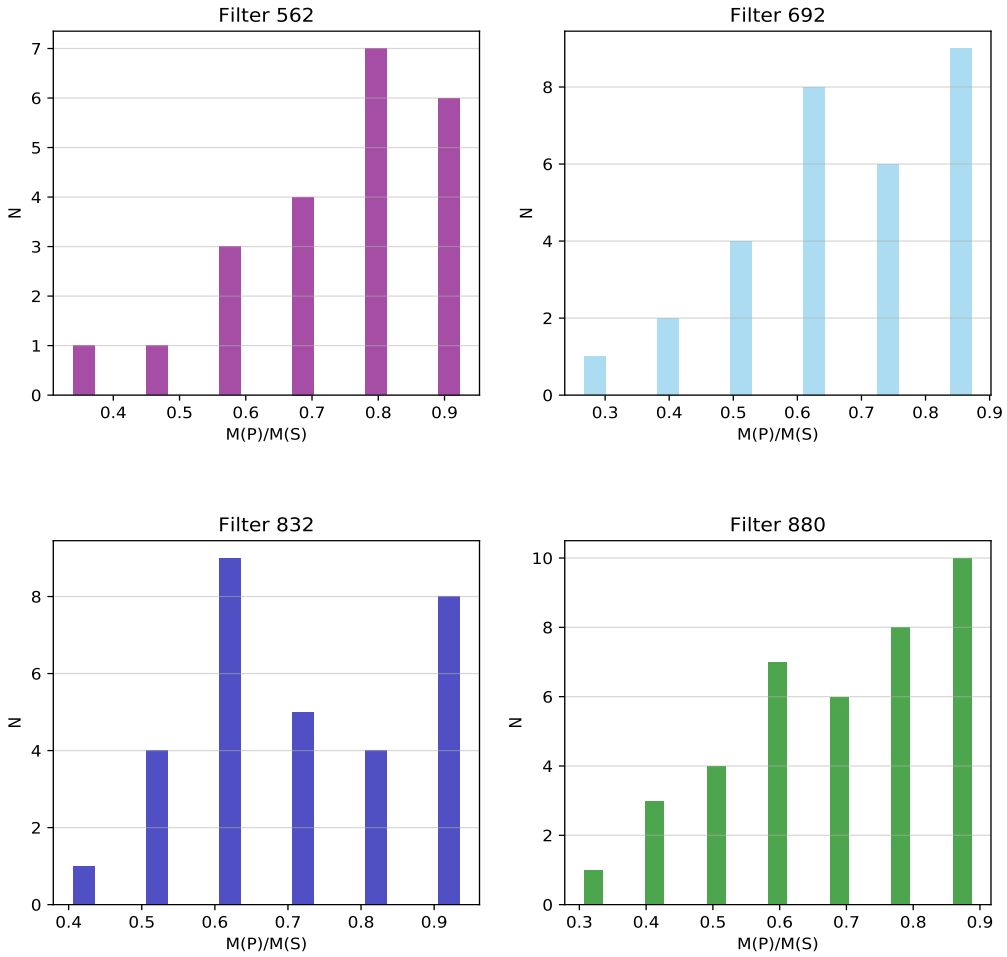

Figure 32: A histogram of the mass ratio filter wise separated to show distribution in each filter clearly.

Figure 33, displays the histogram of the orbital period in units of years. Same figure was shown in the result section but in units of days in order to be directly compared to Raghavan et al. (2010). The two plots (in each unit) are otherwise not different in anyway and they give the same peak.

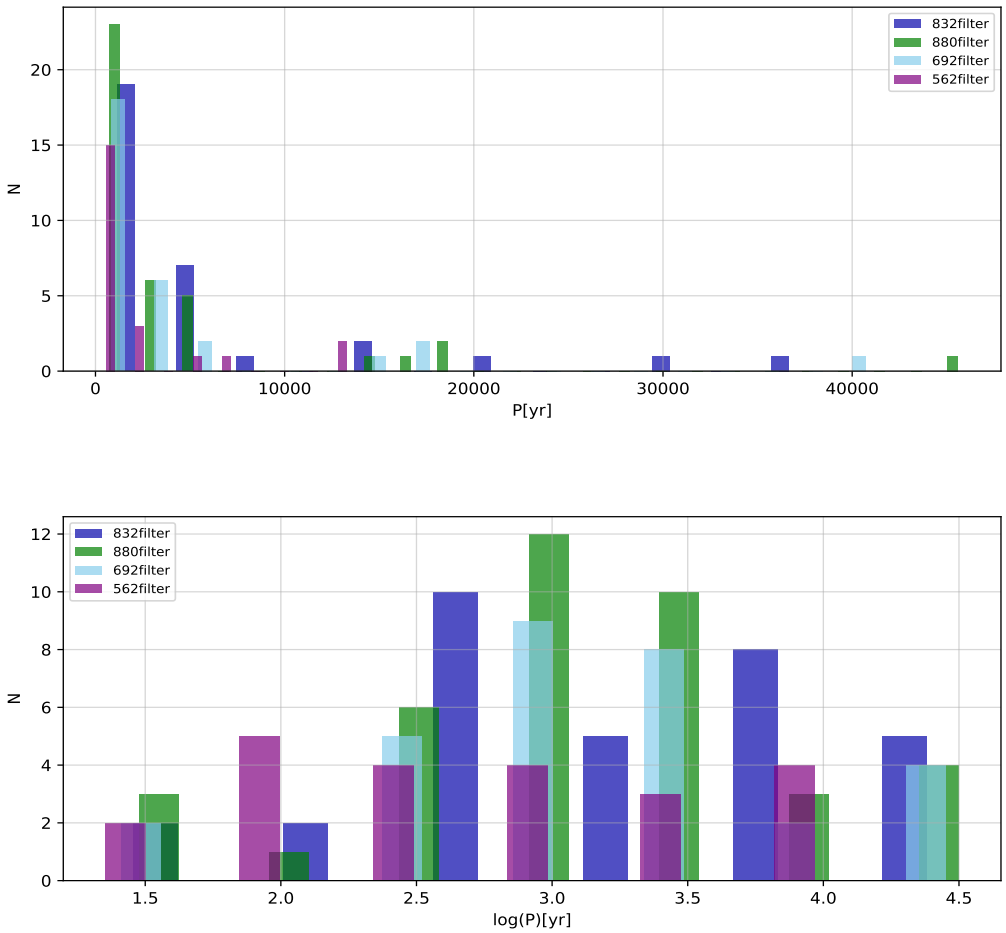

Figure 33: A plot of the orbital period and its logarithm as a histogram. The logarithm plot better displays all the values, in a compact manner. This is orbital period in units of years.

The last figure, shows the orbital period histogram in units of days, same as Figure 16 in Section 4, but here the logarithmic plot has been normalized to be able to fit a Gaussian in the same way as was done in Raghavan et al. (2010).

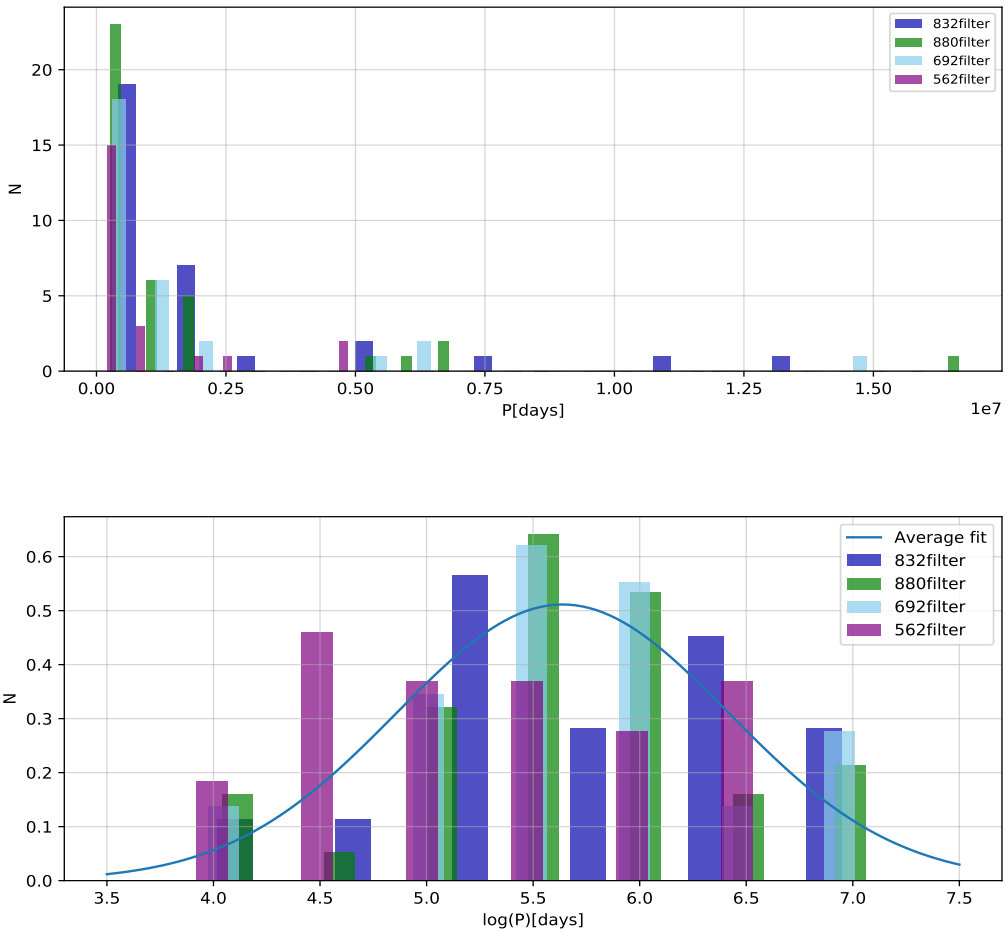

Figure 34: A histogram of the orbital period in units of days and its logarithm, where an average Gaussian fit was applied.

B Collected data from ExoFOP

In this appendix there are tables with information from ExoFOP for each filter (562, 692, 832, 880 and K-band). This is the initial information from the already reduced and processed images from observations with instruments DSSI and NESSI during the years 2016-2018.

Table 2: This table has all the information found on ExoFOP for the 562 filter.

Epicname	Δ_{mag}	V_{sum}	Angular separation["]
212703473	0.93 ± 0.15	10.973 ± 0.096	0.20900
212679181	0.84 ±0.15	12.992 ± 0.040	1.20400
214889247	7.01 ±0.3	10.118 ± 0.037	0.27000
218711655	1.01 ±0.15	11.520 ± 0.147	0.03500
216050437	0.20 ±0.15	12.432 ± 0.040	0.08600
220492184	3.36 ±0.3	8.044 ± 0.014	0.19600
220555384	0.57 ± 0.15	12.880 ± 0.010	0.20300
246356223	0.59 ± 0.15	11.417 ± 0.138	0.96700
247611242	1.76 ± 0.15	10.575 ±0.065	0.12300
247452471	1.87 ± 0.15	10.285 ± 0.045	0.12300
246070458	0.84 ± 0.15	11.083 ± 0.095	0.60500
220666988	1.11 ± 0.15	8.931 ± 0.016	2.28600
220666988	1.18 ± 0.15	8.931 ± 0.016	2.28400
212138198	2.69 ± 0.15	13.205 ± 0.032	0.25300
211428897	1.71 ± 0.15	14.094 ± 0.060	1.04300
211428897	1.84 ± 0.15	14.094 ± 0.060	1.07900
211432167	2.89 ± 0.15	8.235 ± 0.015	2.21100
211432167	3.05 ± 0.15	8.235 ± 0.015	2.20700
211439059	1.49 ± 0.15	13.292 ± 0.050	0.21900
211439059	1.50 ± 0.15	13.292 ± 0.050	0.23100
249928278	1.97 ± 0.15	12.897 ± 0.040	1.13000
248637525	0.72 ± 0.15	13.037 ± 0.032	0.56500
246163416	1.39 ± 0.15	14.285 ± 0.040	0.65700
211719484	3.64 ± 0.2	12.668 ±0.030	0.59600
211941472	0.37 ± 0.15	11.949 ± 0.020	0.20300
211941472	0.28 ±0.15	11.949 ±0.020	0.20300
247002634	4.15 ± 0.3	9.563 ± 0.036	0.32400
247384685	0.37 ±0.15	12.963 ± 0.060	0.95800

Table 3: This table has all the information found on ExoFOP for the 692 filter.

Epicname	Δ_{mag}	r_{sum}	i_{sum}	Separation["]
212703473	1.14 ± 0.15	10.652 ± 0.030	10.520 ± 0.070	0.24800
212679181	1.07 ± 0.15	12.432 ± 0.010	11.240 ± 0.040	1.24500
212679181	1.48 ± 0.15	12.432 ± 0.010	11.240 ± 0.040	1.47800
213563657	2.31 ± 0.15	14.245 ± 0.050	14.061 ± 0.070	0.93300
212773309	2.80 ± 0.15	11.427 ± 0.040	11.009 ± 0.060	1.00900
212773309	2.83 ± 0.15	11.427 ± 0.040	11.009 ±0.060	1.19700
213919915	0.89 ± 0.15	9.344 ± 0.110	8.973 ±0.120	1.08400
212577658	4.31 ± 0.3	11.526 ± 0.020	11.281 ± 0.040	1.81000
212577658	1.01 ± 0.15	11.526 ± 0.020	11.281 ± 0.050	-
212099230	3.948 ± 0.3	10.496 ± 0.040	10.274 ± 0.060	0.10500
212138198	2.064 ± 0.15	12.850 ± 0.041	12.584 ± 0.062	0.25000
212066407	5.315 ±0.3	12.174 ± 0.030	11.982 ± 0.050	0.20900
212315941	1.12 ±0.15	14.356 ± 0.030	14.094 ± 0.060	0.06400
211886472	4.015 ± 0.3	11.071 ± 0.010	10.998 ± 0.010	0.32300
211978865	3.436 ±0.2	14.347 ± 0.040	14.322 ± 0.010	1.06800
211987231	1.672 ± 0.15	11.653 ± 0.020	11.479 ± 0.070	0.90600
211428897	1.811 ± 0.15	13.511 ± 0.050	12.458 ± 0.180	1.08600
210958990	2.707 ± 0.15	12.541 ± 0.070	12.340 ± 0.320	1.65000
249258616	3.95 ±0.3	12.823 ± 0.050	12.392 ± 0.020	1.22100
249559552	5.07 ± 0.3	12.821 ± 0.020	12.516 ± 0.010	0.41600
249447551	1.06 ± 0.15	13.524 ± 0.010	13.226 ± 0.020	1.40400
249401470	4.60 ± 0.3	12.103 ± 0.060	11.854 ± 0.010	0.81600
249401470	3.51 ± 0.3	12.103 ± 0.060	11.854 ±0.010	0.05400
226040726	5.78 ± 0.3	13.096 ± 0.010	12.498 ±0.060	0.97000
214611894	3.03 ±0.2	11.885 ± 0.020	11.566 ± 0.060	1.11400
249644246	0.62 ± 0.15	13.264 ± 0.042	12.864 ± 0.020	1.05400
249780361	3.55 ± 0.3	12.378 ± 0.041	12.201 ± 0.061	0.72300
236344753	1.18 ± 0.15	10.266 ± 0.040	9.922 ± 0.060	1.67300
229039390	5.08 ± 0.3	12.721 ± 0.020	12.592 ± 0.020	0.61400
218131080	2.42 ± 0.15	12.649 ± 0.020	12.589 ± 0.020	0.20800
212303338	2.45 ±0.15	9.779 ± 0.010	9.663 ± 0.010	0.09800
212534729	0.63 ± 0.15	13.043 ± 0.020	12.817 ± 0.090	0.15100
228741710	0.95 ± 0.15	13.463 ± 0.010	13.1889 ± 0.020	1.00000
229002550	3.32 ± 0.2	14.197 ± 0.040	13.747 ±0.060	0.14400

Table 4: This table has all the information found on ExoFOP for the 832 filter.

Epicname	Δ_{mag}	r_{sum}	i_{sum}	Separation["]
212703473	0.84 ± 0.15	10.652 ± 0.030	10.520 ± 0.070	0.21700
212679181	0.64 ± 0.15	12.432 ± 0.010	11.240 ± 0.040	1.23400
220192485	4.60 ± 0.3	11.718 ± 0.010	11.487 ± 0.020	2.28200
220555384	0.21 ± 0.15	12.343 ± 0.020	11.894 ± 0.050	0.19800
220643470	5.43 ± 0.3	10.817 ± 0.010	10.427 ± 0.030	2.20900
220725183	2.98 ± 0.15	11.502 ± 0.060	11.324 ± 0.010	0.16900
220619415	3.85 ± 0.3	13.116 ± 0.042	12.929 ± 0.063	1.49500
220601894	3.91 ± 0.3	13.714 ± 0.010	13.469 ± 0.050	1.60700
246356223	0.53 ± 0.15	11.071 ± 0.040	10.915 ± 0.060	0.99200
247611242	1.85 ± 0.15	10.223 ± 0.030	10.752 ± 0.900	0.13400
247452471	1.90 ± 0.15	10.103 ± 0.060	9.943 ± 0.240	0.12900
245946030	4.57 ± 0.3	11.687 ± 0.010	11.545 ± 0.020	0.82200
220650843	2.97 ± 0.15	13.982 ± 0.010	13.533 ± 0.040	0.96800
220666988	0.72 ± 0.15	9.251 ± 0.040	8.384 ± 0.060	2.29800
220666988	0.76 ± 0.15	9.251 ± 0.040	8.384 ± 0.060	2.29700
212138198	2.04 ± 0.15	12.850 ± 0.041	12.584 ± 0.062	0.26000
211428897	1.14 ± 0.15	13.511 ± 0.050	12.458 ± 0.180	1.06900
211428897	1.19 ± 0.15	13.511 ± 0.050	12.458 ± 0.180	1.07900
211432167	2.44 ± 0.15	8.901 ± 0.020	8.057 ± 0.040	2.18500
211432167	2.47 ± 0.15	8.901± 0.020	8.057 ± 0.040	2.18100
211439059	1.04 ± 0.15	12.986 ± 0.020	12.776 ± 0.020	0.22700
211439059	1.07 ± 0.15	12.986 ± 0.020	12.776 ± 0.020	0.23200
201392505	3.68 ± 0.3	13.390 ± 0.070	13.084 ± 0.060	0.24200
201390927	1.14 ± 0.15	14.159 ± 0.020	13.714 ± 0.100	0.88300
201352100	3.37 ± 0.2	12.693 ± 0.070	12.565 ± 0.190	0.38700
249928278	1.83 ± 0.15	12.663 ± 0.010	12.483 ± 0.060	1.12200
248637525	0.66 ± 0.15	12.749 ± 0.040	12.586 ± 0.050	0.57700
248767140	4.79 ± 0.3	13.141 ± 0.050	12.719 ± 0.110	1.14000
246163416	0.89 ± 0.15	13.725 ± 0.020	12.783 ± 0.030	0.64800
212661144	2.76 ± 0.15	12.797 ± 0.050	13.344 ± 0.030	2.48700
211719484	3.07 ± 0.2	12.540 ± 0.050	12.416 ± 0.030	0.61100
211941472	0.32 ± 0.15	11.789 ± 0.040	11.594 ± 0.080	0.20300
211941472	0.21 ± 0.15	11.789 ± 0.040	11.594 ± 0.080	0.20100
246920193	4.17 ± 0.3	10.876 ± 0.010	10.682 ± 0.010	0.34300
247002634	2.56 ± 0.15	9.609 ± 0.040	8.948 ± 0.030	0.33100
247047370	5.96 ± 0.3	10.850 ± 0.030	10.588 ± 0.050	2.16100
247321442	4.65 ± 0.3	12.317 ± 0.040	12.009 ± 0.061	0.92700
247384685	0.39 ± 0.15	12.595 ± 0.020	12.219 ± 0.040	0.98000
212619190	5.38 ± 0.3	12.797 ± 0.05	12.572 ± 0.080	-

Table 5: This table has all the information found on ExoFOP for the 880 filter.

Epicname	Δ_{mag}	r_{sum}	i_{sum}	Separation["]
212703473	0.94 ± 0.15	10.652 ± 0.030	10.520 ± 0.070	0.24500
212679181	1.12 ± 0.15	12.432 ± 0.010	11.240 ± 0.040	1.25000
212679181	1.15 ± 0.15	12.432 ± 0.010	11.240 ± 0.040	1.45700
214889247	4.60 ± 0.3	9.623 ± 0.090	9.498 ± 0.060	0.24500
213563657	3.28 ± 0.2	14.245 ± 0.050	14.061 ± 0.070	0.93300
212773309	1.99 ± 0.15	11.427 ± 0.040	11.009 ± 0.060	1.00900
212773309	2.04 ± 0.15	11.427 ± 0.040	11.009 ± 0.060	1.18000
212628098	3.82 ± 0.3	13.325 ± 0.020	12.789 ± 0.060	1.25400
213919915	0.96 ± 0.15	9.344 ± 0.110	8.973 ± 0.120	1.09000
218711655	1.44 ± 0.15	11.348 ± 0.040	11.149 ± 0.010	0.02600
216050437	0.44 ± 0.15	12.328 ±0.040	12.184 ± 0.060	0.08500
212577658	0.85 ± 0.15	11.526 ± 0.020	11.281 ± 0.040	0.85000
212099230	3.141 ± 0.2	10.496 ± 0.040	10.274 ± 0.060	0.10500
212099230	3.191± 0.2	10.496 ± 0.040	10.274 ± 0.060	0.10500
212138198	1.613 ± 0.15	12.850 ± 0.041	12.584 ± 0.062	0.25800
212066407	3.998 ± 0.3	12.174 ± 0.030	11.982 ± 0.050	0.21900
212066407	4.060 ± 0.3	12.174 ± 0.030	11.982 ± 0.050	0.22200
212315941	1.29 ± 0.15	14.356 ± 0.030	14.094 ± 0.060	0.05700
211886472	3.767 ± 0.3	11.071 ± 0.010	10.998 ± 0.010	0.32600
211978865	3.196 ± 0.3	14.347 ± 0.040	14.322 ± 0.010	1.13700
211987231	1.458 ± 0.15	11.653 ±0.020	11.479 ± 0.070	0.92400
211428897	1.151 ± 0.15	13.511 ± 0.050	12.458 ± 0.180	1.11900
211147528	7.990 ± 0.3	11.793 ± 0.040	11.700 ± 0.060	1.33800
210958990	2.375 ± 0.15	12.541 ±0.070	12.340 ± 0.320	1.79300
249258616	2.76 ± 0.15	12.823 ±0.050	12.392 ± 0.020	1.21900
249344978	3.73 ± 0.3	15.018 ± 0.030	14.044 ± 0.040	0.58300
249559552	4.01 ± 0.3	12.821 ± 0.020	12.516 ± 0.010	0.41800
249447551	0.97 ±0.15	13.524 ± 0.010	13.226 ± 0.020	1.40800
249401470	3.56 ± 0.2	12.103 ± 0.060	11.854 ± 0.010	0.81900
249401470	2.71 ± 0.15	12.103 ± 0.060	11.854 ± 0.010	0.05400
226040726	4.37 ± 0.3	13.096 ± 0.010	12.498 ± 0.060	0.97300
214611894	2.67 ± 0.15	11.885 ± 0.020	11.566 ± 0.060	1.12800
249644246	0.67 ± 0.15	13.264 ± 0.042	12.864 ± 0.020	1.06100
249624646	5.40 ± 0.3	10.784 ± 0.030	10.614 ± 0.020	0.40400
249780361	3.04 ± 0.2	12.378 ± 0.041	12.201 ±0.061	0.72300
236344753	0.92 ± 0.15	10.266 ± 0.040	9.922 ±0.060	1.74600
249173930	3.86± 0.3	13.278 ± 0.010	12.718 ± 0.010	1.21100
229039390	3.77 ± 0.3	12.721 ± 0.020	12.592 ± 0.020	0.62000
218131080	2.55 ± 0.15	12.649 ± 0.020	12.589 ± 0.020	0.19600
212303338	1.99 ± 0.15	9.779 ± 0.010	9.663 ± 0.010	0.11300
212534729	1.23 ± 0.15	13.043 ± 0.020	12.817 ± 0.090	0.17100
228741710	0.87 ± 0.15	13.463 ± 0.010	13.1889 ± 0.020	1.01900
229002550	2.22 ± 0.15	14.197 ± 0.040	13.747 ± 0.060	0.14800
228920801	4.72 ± 0.3	13.157 ± 0.060	12.935 ± 0.080	0.35800

Table 6: This table has all the information found on ExoFOP for the K-band.

Epicname	K_{sum}
212679798	12 ± 0.032
212703473	9.3 ± 0.021
214889247	8.3 ± 0
212628098	11 ± 0.026
218711655	9.9 ± 0.026
216050437	11 ± 0.019
220492184	7.2 ± 0.021
220555384	9.7 ± 0.021
220643470	8.2± 0.018
220725183	10 ± 0.021
229024057	12 ± 0.021
245946030	10 ± 0.025
212577658	9.9 ± 0.027
220666988	7.0 ± 0.020
212138198	11 ± 0.019
212066407	11 ± 0.019
211886472	10 ± 0.023
211432167	7.1 ± 0.024
211439059	11 ± 0.019
211147528	11 ± 0.021
210958990	11± 0.021
210401157	9.0 ± 0.017
201352100	11 ± 0.021
245944983	10 ± 0.062
213951550	11 ± 0.021
214611894	10 ± 0.023
211941472	10 ± 0.019
211978865	13 ± 0.035
211987231	10 ± 0.023
211428897	9.6 ± 0.023
213920015	7.8± 0.016
218131080	11 ± 0.023
212619190	11 ± 0.024
220187552	9.9 ± 0.025
228731258	12 ± 0.026
249833762	9.5 ± 0.021

C Aperture Photometry

In order to compare the results of speckle imaging data, aperture photometry on AO images was done in a simple manner. All the images were either plotted in Python or displayed in SAOImageDS9 in order to manually find a center for each light source in pixel coordinates. However, this was not possible for all the images, in many cases the secondary was too faint and not seen on the images. A way to work around that would be to use the position angle and the angular separation from speckle imaging observations to calculate where the secondary would be on the AO images and guess a center. However, this was outside the scoop of this project, this extra part was not intended to be of more importance for this thesis, only a quick way to check the mass-results from calculations with speckle imaging data to another method.

The goal of this aperture photometry was to find the magnitude difference in K-band and use it to find the mass of each star in the system. For this the photutils Python package was used, which provides tools for performing aperture photometry on any astronomical image in either pixel coordinates (as done here) or sky coordinates. The main idea behind it is to define an aperture object (circular was used in my project) that encircles the light source of which the intensity is to be measured. To set the circular apertures one needs to define the light sources, which was done manually by finding a guess for the center of each source using SAOImageDS9 or a Python plot of the image. Then these guesses were given to the sub-package centroids, to get a better estimate of the center at the given position. A centroid, also called the geometric center, refers to the mean of all the pixels, or points in the image, in all directions. The radius of the circular apertures was chosen so that enough light from the source was enclosed and avoiding overlap with light from the other light source in the image. As for any image photometry one also needs to find the background noise and subtract it. The same package was used but with a different type of aperture called circular annulus aperture. This aperture is two circles with two different radii but closely spaced (the radii were kept the same at 4 and 6 pixels). The mean of the background noise was subtracted from the intensity found inside the circular apertures enclosing the light sources. The corrected intensity was then used to find the magnitude difference using Equation (21) (see all the information on center coordinates

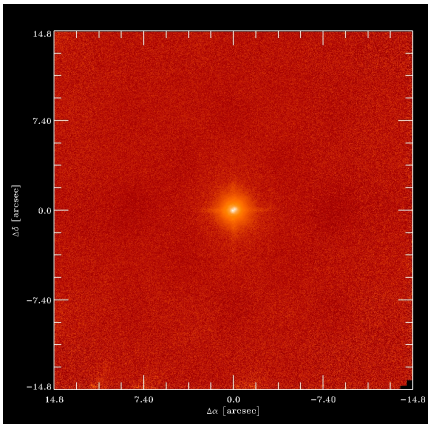

Figure 35: An image from AO observations of the target with epicname 212703473 conducted at Palomar telescope. Source: ExoFOP database.

in Appendix C).

In order to find the mass of each star the magnitude difference was inserted in Equation (8) to get the absolute magnitude (in K-band), which was then inserted in one of the MLR equations, see Equations (5) through (7), in order to get the masses.

$$m = -2.5\log(I) + C_T \rightarrow \Delta m = 2.5\log(I_P) - 2.5\log(I_S) \tag{21}$$

Where m is the apparent magnitude, I is the intensity or in other words the total photon count within the aperture corrected for background noise and C_T is a telescope constant, Howell (2000).

C.1 Aperture photometry information

In this appendix information used to perform aperture photometry is presented. Note that the radius of the circular aperture was small so that it could be kept unchanged for consistent results. A few have a radius of 1 instead of 1.5 as the rest, because the stars were so close that light from the other overlapped if the radius was set to be larger than 1.

Table 7: This table shows the information needed to repeat the aperture photometry and get the same results.

Epicname	x-position	y-position	background-x	background-y	r	
201352100	409.469	408.469	400	200	1.5	Primary
201352100	422.625	420.562	400	200	1.5	Secondary
210401157	778.125	778.438	400	200	1.5	Primary
210401157	761.5	734	400	200	1.5	Secondary
210958990	780.5	780.406	400	200	1.5	Primary
210958990	937.719	687.531	400	200	1.5	Secondary
211147528	773	779.49	400	200	1	Primary
211147528	778.61	773.49	400	200	1	Secondary
211428897	709	712.5	400	200	1.5	Primary
211428897	636	793	400	200	1.5	Secondary
211432167	650.5	649.5	400	200	1.5	Primary
211432167	737.375	655.188	400	200	1.5	Secondary
211432167	555.5	556.469	400	200	1.5	Primary
211432167	642.125	561.469	400	200	1.5	Secondary
211432167	567.5	567.438	400	200	1.5	Primary
211432167	654.438	571.5	400	200	1.5	Secondary
211439059	657.938	661.031	400	200	1.5	Primary
211439059	662.5	651.531	400	200	1.5	Secondary

Table 7 continued from previous page

Epicname	x-position	y-position	background-x	background-y	r	
211439059	662.469	667.469	400	200	1.5	Primary
211439059	667.531	658.375	400	200	1.5	Secondary
211439059	661.031	666.969	400	200	1.5	Primary
211439059	665.5	658.156	400	200	1.5	Secondary
211941472	611.906	616.062	400	200	1.5	Primary
211941472	619.562	611.344	400	200	1.5	Secondary
211941472	648.438	655.031	400	200	1.5	Primary
211941472	657.438	650.406	400	200	1.5	Secondary
211941472	652.469	655.469	400	200	1.5	Primary
211941472	660.469	651.469	400	200	1.5	Secondary
211978865	661.125	661.75	400	200	1.5	Primary
211978865	680.25	699.875	400	200	1.5	Secondary
211987231	732	735.5	400	200	1.5	Primary
211987231	809	687.25	400	200	1.5	Secondary
212138198	709.25	709.062	400	200	1.5	Primary
212138198	695.5	730.469	400	200	1.5	Secondary
212577658	647.047	647.219	400	200	1.5	Primary
212577658	660.25	702.125	400	200	1.5	Secondary
212628098	410.375	411.438	400	200	1.5	Primary
212628098	379.438	491.188	400	200	1.5	Secondary
212703473	595.438	590.906	400	200	1.5	Primary
212703473	588.406	597.406	400	200	1.5	Secondary
213920015	394.469	394.484	400	200	1.5	Primary
213920015	377.912	440.562	400	200	1.5	Secondary
213951550	408.5	408.312	400	200	1.5	Primary
213951550	401.375	413.312	400	200	1.5	Secondary
214611894	410.562	411.312	400	200	1.5	Primary
214611894	458.812	393	400	200	1.5	Secondary
214889247	407.562	407.562	400	200	1.5	Primary
214889247	273.485	512.495	400	200	1.5	Secondary
216050437	405	406	400	200	1	Primary
216050437	400.310	399.5	400	200	1	Secondary
218131080	403.312	403.438	400	200	1.5	Primary
218131080	405.188	392	400	200	1.5	Secondary
218711655	400	402.5	400	200	1.5	Primary
218711655	564	508	400	200	1.5	Secondary

Table 7 continued from previous page

Epicname	x-position	y-position	background-x	background-y	r	
218711655	400	402.5	400	200	1.5	Primary
218711655	581.75	618.75	400	200	1.5	Secondary
220187552	783.375	784.125	400	200	1.5	Primary
220187552	790.75	756.375	400	200	1.5	Secondary
220492184	796.469	794.531	400	200	1.5	Primary
220492184	799.594	776.25	400	200	1.5	Secondary
220555384	408.531	410.531	400	200	1.5	Primary
220555384	418.938	411.906	400	200	1.5	Secondary
220666988	732.34	733.34	400	200	1.5	Primary
220666988	773.867	960.07	400	200	1.5	Secondary
228731258	267.119	265.333	400	200	1.5	Primary
228731258	257.13	270.098	400	200	1.5	Secondary
245944983	781.126	781.042	400	200	1.5	Primary
245944983	1122.04	618.674	400	200	1.5	Secondary
245946030	273.498	274.419	400	200	1.5	Primary
245946030	238.333	259.683	400	200	1.5	Secondary

D Tabulated results

In this fourth appendix all the result tables are available. The order of the tables is as follows; the physical separation, the masses and the mass ratio, the masses and the mass ratio and the magnitude difference from aperture photometry in K-band and lastly the orbital period.

Table 8: This table shows the median of the physical separation in astronomical units and the corresponding asymmetric errors.

Epicname	Physical separation[au]	"Lower"-error	"Upper"-error
201352100	75	1.5	1.6
201390927	326	33.1	33
201392505	66	1.7	1.6
203868608	19	0.9	0.85
210401157	128	7	8
210401157	123	7	8
210958990	802	23	22
210958990	738	19	21
211147528	735	25	26
211428897	51	0.27	0.27
211428897	53	0.27	0.28
211428897	52	0.28	0.29
211428897	50	0.28	0.27
211432167	387	7.2	6.8
211432167	391	7.0	7.2
211439059	77	17	26
211439059	78	16	25
211719484	483	31	33
211719484	493	28	34
211886472	163	9	10
211886472	161	9	10
211941472	399	113	161
211941472	401	111	157
211978865	1599	96	104.54
211978865	1505	82	89.31
211987231	347	33	38.58
211987231	356	36	39.49
212066407	189	20	24.49
212066407	200	23	23.48

Table 8 continued from previous page

212099230	13	0.27	0.2
212099230	13	0.3	0.2
212138198	55	3.8	4.0
212138198	57	3.7	4
212138198	57	3.7	4
212138198	55	3.7	3.9
212303338	8	0.18	0.17
212303338	9	0.2	0.1
212315941	55	5.5	6.7
212315941	49	5.3	5.8
212534729	139	37	66
212534729	124	32	61
212577658	436	5.0	5.8
212577658	205	2.8	2.6
212619190	-	-	-
212628098	267	1.7	1.4
212651213	192	73	129
212661144	1315	17	16
212679181	58	0.3	0.28
212679181	58	0.31	0.30
212679181	53	0.26	0.27
212679181	52	0.28	0.26
212679798	52	1.5	1.53
212703473	124	56	227
212703473	123	54	230
212703473	101	51	199
212703473	105	50	202
212773309	132	1.2	1.3
212773309	133	1.2	1.0
213563657	859	30.7	31
213563657	830	31	33
213919915	109	1.4	1.2
213919915	108	1.3	1.4
213920015	104	1.6	1.7
213951550	28	0.95	1.0
214611894	323	3.9	4
214611894	319	3.8	3.76

Table 8 continued from previous page

214889247	27	0.4	0.3
214889247	30	0.4	0.3
216050437	106	37	104
216050437	104	36	99
218131080	74	8.	10
218131080	79	8	10
218711655	13	0.7	0.8
218711655	10	0.79	0.8
220192485	364	3.0	2.9
220492184	35	0.9	1.0
220555384	30	2.3	2.5
220555384	29	2.3	2.2
220601894	906	16	17
220619415	1216	44	47
220643470	4774	476	537
220650843	221	2.3	2.4
220666988	255	9	8.9
220666988	257	9.3	8.9
220725183	79	1.8	1.79
221780098	1603	727	1149
223492687	51	4.6	5.0
224567794	524	240	960
226040726	111	0.47	0.45
226040726	112	0.48	0.47
228741710	369	12	12.2
228741710	375	12.28	12.29
228920801	222	4.8	4.6
228964773	262	8.2	8.8
229002550	50	3.4	3.9
229024057	144	4.8	4.7
229039390	269	5.9	5.4
229039390	271	5.2	5.5
231275397	2565	170	237
233471802	45	1.1	1.13
235941351	955	440	690
236176880	5183	3193	4944
236344753	157	1.3	1.0

Table 8 continued from previous page

236344753	164	1.3	1.2
240362400	154	16	18
245944983	105	0.48	0.5
245946030	283	4.6	4.2
246070458	271	44	60
246163416	56	3.34	3.5
246163416	55	3.35	3.1
246356223	171	16.9	17
246356223	165	17	19
246920193	49	0.45	0.5
247002634	16	0.27	0.3
247002634	16	0.27	0.3
247047370	245	1.4	1
247321442	376	7.6	7
247384685	767	29	30
247384685	782	29	32
247452471	34	0.9	0.8
247452471	36	0.9	1.0
247611242	7.4	0.1	0.1
247611242	6.8	0.1	0.1
248637525	113	11	17
248637525	113	13	16
248767140	360	3.5	3.4
249173930	207	1.1	1.0
249258616	201	1.4	1.5
249258616	201	1.4	1.3
249344978	81	0.7	0.6
249401470	15	0.6	0.7
249401470	229	2.3	2.3
249447551	827	21	21
249447551	829	19	18
249559552	87	1.0	0.9
249559552	86	0.9	0.8
249624646	110	1.8	1.6
249644246	351	5.8	5.9
249644246	354	6.5	5.8
249780361	315	22	21

Table 8 continued from previous page

249780361	316	23	21
249928278	711	43	45
249928278	717	43	42

Table 9: In this table the median of the primary mass, referred to as M_P, the secondary mass, referred to as M_S and the mass ratio, referred to as Ratio, together with their asymmetric errors referred to as "upper" and "lower" is shown for the 562 filter.

Epicname	M_P[$M_\odot$]	Lower	Upper	M_S[$M_\odot$]	Lower	Upper	Ratio	Lower	Upper
211428897	0.46	0.03	0.04	0.23	0.01	0.02	0.51	0.03	0.01
211432167	1.76	0.13	0.14	1.02	0.08	0.07	0.58	0.02	0.01
211439059	0.90	0.10	0.12	0.71	0.07	0.09	0.80	0.01	0.02
211719484	1.42	0.12	0.11	0.77	0.06	0.07	0.54	0.02	0.03
211941472	-	-	-	-	-		-	-	-
212138198	0.80	0.06	0.05	0.56	0.05	0.04	0.70	0.01	0.02
212679181	0.50	0.04	0.05	0.42	0.03	0.04	0.85	0.03	0.04
214889247	1.05	0.07	0.08	0.31	0.04	0.03	0.30	0.03	0.04
216050437	-	-	-	-	-	-	-0	-	-
218711655	1.23	0.10	0.09	1.03	0.09	0.08	0.84	0.02	0.03
220492184	1.81	0.14	0.15	0.98	0.09	0.08	0.54	0.03	0.02
220555384	0.70	0.06	0.05	0.64	0.05	0.06	0.93	0.02	0.01
220666988	1.23	0.10	0.09	1.00	0.08	0.07	0.82	0.03	0.02
246070458	1.41	0.14	0.16	1.21	0.12	0.15	0.86	0.01	0.02
246163416	0.52	0.04	0.05	0.39	0.04	0.05	0.75	0.04	0.05
246356223	0.91	0.07	0.08	0.83	0.08	0.07	0.91	0.03	0.02
247002634	0.85	0.07	0.06	0.56	0.07	0.09	0.66	0.07	0.08
247384685	1.21	0.10	0.09	1.14	0.09	0.08	0.94	0.03	0.02
247452471	1.40	0.10	0.11	1.01	0.07	0.08	0.72	0.02	0.03
247611242	0.74	0.05	0.06	0.59	0.04	0.03	0.79	0.01	0.02
248637525	0.75	0.06	0.07	0.68	0.06	0.05	0.90	0.02	0.02
249928278	1.22	0.09	0.10	0.88	0.07	0.08	0.72	0.02	0.02

Table 10: In this table the median of the primary mass, M_P, the secondary mass, M_S and the mass ratio, "Ratio", together with their asymmetric errors referred to as "upper" and "lower" are shown for the 692 filter.

Epicname	$M_P[M_\odot]$	Lower	Upper	$M_S[M_\odot]$	Lower	Upper	Ratio	Lower	Upper
210958990	1.11	0.09	0.08	0.73	0.06	0.05	0.66	0.02	0.01
211428897	0.55	0.04	0.05	0.28	0.033	0.03	0.51	0.03	0.033
211886472	1.53	0.12	0.13	0.77	0.06	0.08	0.51	0.02	0.021
211978865	1.26	0.10	0.11	0.72	0.05	0.07	0.58	0.02	0.021
211987231	1.20	0.10	0.11	0.91	0.08	0.084	0.76	0.02	0.01
212066407	1.60	0.14	0.15	0.67	0.06	0.062	0.42	0.02	0.03
212099230	0.98	0.07	0.08	0.56	0.04	0.05	0.57	0.01	0.02
212138198	0.81	0.06	0.07	0.61	0.05	0.04	0.75	0.02	0.01
212303338	0.94	0.07	0.08	0.65	0.05	0.04	0.70	0.02	0.01
212315941	0.99	0.07	0.09	0.83	0.06	0.07	0.84	0.02	0.03
212534729	-	-	-		-	-	-	-	-
212577658	1.03	0.08	0.09	0.71	0.06	0.05	0.7	0.02	0.024
212679181	0.54	0.04	0.05	0.46	0.04	0.05	0.86	0.04	0.03
212703473	-	-	-	-	-	-	-	-	-
212773309	0.85	0.07	0.06	0.57	0.03	0.04	0.68	0.01	0.02
213563657	1.06	0.09	0.10	0.74	0.05	0.06	0.70	0.01	0.02
213919915	1.05	0.08	0.09	0.90	0.08	0.07	0.86	0.024	0.02
214611894	1.06	0.08	0.10	0.67	0.06	0.05	0.63	0.01	0.02
218131080	1.02	0.09	0.08	0.70	0.05	0.06	0.69	0.01	0.02
226040726	0.66	0.05	0.06	-	-	-	-	-	-
228741710	0.85	0.07	0.06	0.74	0.06	0.05	0.87	0.04	0.02
229002550	0.78	0.07	0.06	0.51	0.04	0.03	0.65	0.03	0.02
229039390	1.08	0.08	0.09	0.53	0.05	0.04	0.49	0.02	0.01
236344753	0.89	0.06	0.07	0.75	0.05	0.06	0.84	0.02	0.03
249258616	0.76	0.06	0.05	0.46	0.06	0.07	0.61	0.06	0.07
249401470	1.02	0.07	0.08	0.58	0.04	0.05	0.56	0.02	0.01
249447551	0.99	0.07	0.08	0.84	0.07	0.06	0.84	0.02	0.023
249559552	0.82	0.05	0.06	0.36	0.05	0.06	0.44	0.05	0.06
249644246	0.83	0.06	0.07	0.76	0.05	0.07	0.91	0.02	0.01
249780361	1.13	0.09	0.10	0.66	0.06	0.06	0.58	0.03	0.02

Table 11: In this table the median of the primary mass, M_P, the secondary mass, M_S and the mass ratio, "Ratio", together with their asymmetric errors referred to as "upper" and "lower" are shown for the 832 filter.

Epicname	$M_P[M_\odot]$	Lower	Upper	$M_S[M_\odot]$	Lower	Upper	Ratio	Lower	Upper
201352100	0.80	0.08	0.09	0.51	0.06	0.05	0.65	0.02	0.02
201390927	0.81	0.08	0.07	0.69	0.08	0.07	0.85	0.02	0.01
201392505	0.83	0.08	0.07	0.51	0.05	0.05	0.62	0.02	0.02
211428897	0.54	0.05	0.06	0.48	0.08	0.09	0.89	0.11	0.10
211432167	1.72	0.19	0.20	1.09	0.11	0.12	0.63	0.03	0.02
211439059	0.90	0.11	0.13	0.76	0.09	0.11	0.85	0.02	0.02
211719484	1.36	0.13	0.15	0.81	0.08	0.09	0.60	0.01	0.02
211941472	-	-	-	-	-	-	-	-	-
212138198	0.82	0.08	0.09	0.62	0.06	0.06	0.75	0.02	0.02
212619190	-	-	-	-	-	-	-	-	-
212661144	0.96	0.09	0.10	0.64	0.06	0.05	0.67	0.02	0.01
212679181	0.60	0.05	0.06	0.55	0.05	0.05	0.92	0.03	0.02
212703473	-	-	-	-	-	-	-	-	-
220192485	0.89	0.08	0.09	0.53	0.10	0.10	0.59	0.07	0.08
220555384	0.75	0.07	0.08	0.73	0.06	0.07	0.97	0.02	0.02
220601894	1.00	0.11	0.09	0.57	0.05	0.06	0.57	0.01	0.02
220619415	1.26	0.12	0.14	0.69	0.07	0.07	0.54	0.02	0.03
220643470	-	-	-	1.11	0.13	0.13	-	-	-
220650843	1.21	0.12	0.13	0.99	0.09	0.12	0.78	0.02	0.01
220666988	1.27	0.12	0.14	1.11	0.10	0.11	0.87	0.02	0.01
220725183	1.35	0.14	0.13	0.82	0.08	0.07	0.61	0.02	0.03
245946030	1.15	0.11	0.12	0.58	0.05	0.06	0.51	0.02	0.02
246163416	0.60	0.05	0.06	0.54	0.05	0.04	0.90	0.02	0.01
246356223	0.92	0.09	0.10	0.85	0.09	0.08	0.92	0.02	0.02
246920193	0.97	0.09	0.10	0.54	0.05	0.06	0.56	0.02	0.02
247002634	0.88	0.09	0.08	0.62	0.06	0.05	0.70	0.02	0.01
247047370	0.91	0.08	0.10	0.34	0.07	0.06	0.37	0.05	0.05
247321442	1.15	0.12	0.11	0.57	0.05	0.06	0.50	0.02	0.01
247384685	1.29	0.12	0.13	1.21	0.12	0.13	0.93	0.03	0.04
247452471	1.38	0.16	0.17	0.99	0.11	0.12	0.72	0.02	0.01
247611242	0.67	0.10	0.14	0.53	0.07	0.10	0.80	0.03	0.02
248637525	0.76	0.08	0.09	0.69	0.07	0.08	0.91	0.02	0.03
248767140	0.93	0.08	0.09	0.55	0.10	0.12	0.59	0.08	0.09
249928278	1.20	0.13	0.14	0.89	0.09	0.10	0.74	0.02	0.03

Table 12: In this table the median of the primary mass, M_P, the secondary mass, M_S and the mass ratio, "Ratio", together with their asymmetric errors referred to as "upper" and "lower" are shown for the 880 filter.

Epicname	$M_P[M_\odot]$	Lower	Upper	$M_S[M_\odot]$	Lower	Upper	Ratio	Lower	Upper
210958990	1.10	0.13	0.14	0.75	0.08	0.09	0.69	0.02	0.01
211147528	1.35	0.14	0.15	0.37	0.07	0.08	0.27	0.03	0.04
211428897	0.54	0.05	0.05	0.48	0.08	0.10	0.90	0.11	0.10
211886472	1.47	0.14	0.16	0.78	0.08	0.09	0.53	0.03	0.02
211978865	1.20	0.13	0.13	0.72	0.07	0.08	0.60	0.01	0.03
211987231	1.16	0.12	0.14	0.91	0.09	0.11	0.78	0.02	0.02
212066407	1.57	0.18	0.20	0.79	0.08	0.09	0.50	0.03	0.02
212099230	0.98	0.09	0.10	0.62	0.06	0.07	0.63	0.02	0.03
212138198	0.81	0.08	0.08	0.65	0.05	0.06	0.80	0.01	0.02
212303338	0.91	0.08	0.09	0.68	0.06	0.07	0.75	0.02	0.03
212315941	1.00	0.11	0.11	0.81	0.08	0.09	0.81	0.02	0.02
212534729	1.24	0.20	0.24	1.00	0.15	0.18	0.81	0.01	0.02
212577658	0.99	0.09	0.10	0.86	0.08	0.09	0.87	0.02	0.03
212628098	0.81	0.08	0.07	0.56	0.11	0.11	0.69	0.10	0.10
212679181	0.61	0.05	0.05	0.53	0.05	0.05	0.87	0.02	0.02
212703473	-	-	-	-	-	-	-	-	-
212773309	0.86	0.08	0.09	0.64	0.06	0.07	0.75	0.02	0.03
213563657	1.07	0.10	0.11	0.65	0.06	0.06	0.61	0.02	0.01
213919915	1.08	0.11	0.11	0.92	0.09	0.10	0.85	0.02	0.03
214611894	1.07	0.10	0.11	0.71	0.06	0.06	0.66	0.02	0.03
214889247	1.08	0.10	0.11	0.56	0.05	0.05	0.52	0.02	0.01
216050437	-	-	-	-	-	-	-	-	-
218131080	0.98	0.10	0.10	0.67	0.06	0.06	0.68	0.01	0.02
218711655	1.24	0.12	0.12	0.97	0.10	0.09	0.78	0.02	0.01
226040726	0.69	0.06	0.07	0.31	0.05	0.07	0.45	0.06	0.05
228741710	0.85	0.08	0.09	0.75	0.07	0.08	0.88	0.01	0.02
228920801	1.14	0.11	0.12	0.57	0.05	0.06	0.50	0.03	0.02
229002550	0.80	0.07	0.08	0.59	0.05	0.05	0.74	0.02	0.01
229039390	1.05	0.10	0.10	0.60	0.06	0.07	0.57	0.02	0.02
236344753	0.89	0.08	0.09	0.78	0.07	0.08	0.87	0.02	0.01
249173930	0.76	0.06	0.07	0.48	0.09	0.10	0.62	0.08	0.09
249258616	0.79	0.08	0.07	0.55	0.06	0.05	0.70	0.02	0.01
249344978	0.60	0.05	0.06	0.27	0.06	0.06	0.44	0.06	0.07
249401470	1.01	0.09	0.10	0.64	0.06	0.07	0.64	0.02	0.01
249447551	1.01	0.10	0.10	0.87	0.08	0.09	0.86	0.02	0.02
249559552	0.83	0.07	0.08	0.55	0.10	0.12	0.67	0.08	0.09
249624646	1.24	0.12	0.13	0.56	0.06	0.05	0.45	0.03	0.02
249644246	0.86	0.08	0.09	0.78	0.07	0.08	0.90	0.01	0.02
249780361	1.12	0.10	0.11	0.70	0.07	0.07	0.62	0.02	0.03

Table 13: In this table the median of the primary mass, M_P, the secondary mass, M_S and the mass ratio, "Ratio", together with their asymmetric errors referred to as "upper" and "lower" are shown for the K-band. When ever there were more than one image the results from each image were averaged to one value.

Epicname	$M_P[M_\odot]$	Lower	Upper	$M_S[M_\odot]$	Lower	Upper	Ratio	Lower	Upper
201352100	0.73	0.05	0.05	0.31	0.02	0.03	0.43	0.01	0.01
210958990	0.85	0.06	0.07	0.56	0.04	0.05	0.66	0.00	0.01
211147528	0.57	0.05	0.04	0.56	0.04	0.05	1.00	0.01	0.01
211428897	-	-	-	0.85	0.08	0.07	-	-	-
211439059	0.99	0.07	0.08	0.93	0.07	0.06	0.94	0.015	0.012
211439059	0.14	0.02	0.01	0.12	0.01	0.02	0.90	0.01	0.005
211886472	0.22	0.01	0.02	0.22	0.02	0.03	1.00	0.001	0.003
211941472	0.18	0.015	0.01	0.17	0.02	0.01	0.92	0.01	0.004
211978865	0.23	0.01	0.02	0.15	0.02	0.01	0.66	0.01	0.01
211987231	0.71	0.06	0.05	0.58	0.04	0.03	0.82	0.002	0.003
212066407	0.58	0.04	0.05	0.58	0.04	0.05	1.00	-	-
212138198	0.62	0.04	0.05	0.50	0.04	0.03	0.80	0.01	0.01
212577658	-	-	-	0.97	0.14	0.19	0.00	0.002	0.003
212619190	0.75	0.11	0.12	0.75	0.11	0.12	1.00	0.002	0.003
212628098	0.93	0.14	0.16	0.71	0.11	0.12	0.76	0.003	0.004
212679798	0.57	0.08	0.10	0.57	0.08	0.10	1.00	0.005	0.007
213951550	0.90	0.07	0.07	0.66	0.05	0.05	0.73	0.01	0.02
214611894	-	-	-	0.90	0.07	0.07	0-	-	-
220187552	-	-	-	0.46	0.04	0.05	-	-	-
228731258	0.19	0.01	0.02	0.16	0.02	0.01	0.83	0.014	0.01
229024057	0.30	0.022	0.02	0.30	0.03	0.02	1.00	0.01	0.014
245944983	0.53	0.04	0.04	0.51	0.05	0.04	0.97	0.012	0.006
245946030	0.86	0.07	0.08	0.26	0.02	0.03	0.30	0.02	0.03
249833762	0.90	0.09	0.08	0.90	0.09	0.08	1.00	0.01	0.015

Table 14: This table shows the results from photometry. Here are the values of the magnitude difference and the corresponding standard deviation.

Epicname	Magnitude difference	standard deviation
201352100	2.35	0.0076
210401157	1.62	0.0012
210958990	1.73	0.0019
211147528	0.01	0.0014
211428897	0.80	0.0011
211432167	1.48	0.0004
211432167	1.56	0.0008
211432167	1.59	0.0004
211439059	0.19	0.0003
211439059	0.26	0.0004
211439059	0.28	0.0007
211941472	0.19	0.0002
211941472	0.18	0.0002
211941472	0.31	0.0008
211978865	0.87	0.0029
211987231	0.85	0.0009
212138198	0.93	0.0026
212577658	0.40	0.0004
212628098	1.11	0.0039
212703473	0.54	0.0005
213920015	0.10	0.0017
214611894	1.31	0.0005
214611894	1.79	0.0042
214889247	0.64	0.0020
216050437	0.22	0.0039
218131080	1.48	0.0078
218711655	4.26	0.0369
220492184	2.49	0.0045
220555384	0.35	0.0015
220666988	0.45	0.0005
228731258	0.43	0.0052
245944983	0.14	0.0003
245946030	3.37	0.0152

Table 15: This table shows the values of the orbital period and the corresponding asymmetric errors for all of the systems.

201352100	568.39	30.24	32.11
201390927	4805	669	837
201392505	466	29	28
210958990	16823	1042	945
210958990	14761	987	1058
211147528	15207	1186	1310
211428897	385	27	24
211428897	362	23	22
211428897	406	18	17
211428897	432	17	17
211432167	4630	209	206
211432167	4523	254	268
211439059	536	157	262
211439059	552	164	264
211719484	7151	740	761
211719484	7478	801	806
211886472	1389	126	143
211886472	1348	117	136
211941472	5814	2302	3664
211978865	45721	4176	4594
211978865	42181	3800	4643
211987231	4482	707	843
211987231	4673	746	859
212066407	1683	267	352
212066407	1810	293	377
212099230	37	2.2	2
212099230	38	2	2.2
212138198	339	33	38
212138198	359	37	48
212138198	356	37	41
212138198	354	36	38
212303338	17	1	0.98
212303338	22	1.09	1.04
212315941	296	44	57
212315941	248	37	45

Table 15 continued from previous page

212534729	1123	412	857
212577658	6672	346	357
212577658	2292	97	99
212628098	3724	228	235
212661144	37667	1802	1951
212679181	386	15	14
212679181	449	17	16
212679181	358	17	15
212679181	414	19	18
212773309	1297	51	48
212773309	1240	61	59
213563657	19242	1341	1471
213563657	17884	1188	1229
213919915	816	34	33.9
213919915	799	43	42.6
214611894	4361	222	230
214611894	4355	188	175
214889247	122	5	5.2
214889247	130	6	6.4
216050437	610	294	946
218131080	484	76	106
218131080	544	91	109
218711655	31	2.9	3
218711655	20	2.7	2.6
220192485	5857	373	406
220492184	124	6.8	7.1
220555384	134	16.9	17.3
220555384	135	16	18
220601894	21739	1243	1201
220619415	30460	2038	2280
220650843	2944	134	136
220666988	2736	164	161
220666988	2686	180	186
220725183	476	29	29
226040726	1447	53	50
226040726	1175	64	71
228741710	5567	375	402

Table 15 continued from previous page

228741710	5727	361	384
228920801	2522	156	148
229002550	302.44	34	35
229039390	3430	202	193
229039390	3528	159	164
236344753	1520	75	72
236344753	1638	64.7	65
245946030	3596	198	173
246070458	2746	660	989
246163416	434	41	43
246163416	381	35	39
246356223	1683	255	294
246356223	1612	240	294
246920193	281	13	14
247002634	53	2.7	2.8
247002634	50	2.6	3
247047370	3431	200	179
247321442	5576	330	326
247384685	13771	926	1040
247384685	13821	1054	1071
247452471	131	9	8
247452471	139	7.4	7
247611242	18	1.7	1.5
247611242	15	0.67	0.71
248637525	1038	174	216
248637525	1018	177	216
248767140	5611	373	389
249173930	2660	162	171
249258616	2475	117	109
249258616	2587	119	110
249344978	783	42	44
249401470	1406	57	57
249401470	1383	65	68
249447551	17578	973	882
249447551	17494	1045	1079
249559552	688	45	47
249559552	736	34	32

Table 15 continued from previous page

249624646	860	46	47
249644246	5219	273	236
249644246	5200	265	265
249780361	4140	441	476
249780361	4167	426	456
249928278	13186	1338	1301
249928278	13260	1236	1306

E Comparing filters

In this appendix tables for each property are presented, where the results are given filter wise, side by side. This is an attempt to understand if the method works well and if the filters give roughly similar results for the same system, which they should since the method of observation is the same.

Table 16: This table shows the physical separation for all the systems which have known distances to the primary star. Here one can see the results from all filters and compare to see if they match.

Epicname	Filter 562	Filter 692	Filter 832	Filter 880
212773309		$133^{1.1}_{1.2}$		$131^{1}_{1.2}$
201352100			$75^{1.3}_{1.5}$	
201390927			323^{34}_{32}	
212703473	101^{202}_{46}	122^{233}_{59}	109^{194}_{45}	120^{219}_{56}
212679181	$52^{0.27}_{0.26}$	$58^{0.3}_{0.29}$	$53^{0.29}_{0.27}$	$58^{0.30}_{0.31}$
214889247	$30^{0.3}_{0.4}$			$27^{0.3}_{0.4}$
213563657		830^{31}_{30}		$860^{32}_{32.3}$
212628098				$267^{1.5}_{1.4}$
220192485			$364^{2.8}_{2.9}$	
213919915		$108^{1.4}_{1.3}$		$109^{1.4}_{1.3}$
218711655	$13^{0.7}_{0.8}$			$10^{0.9}_{0.8}$
216050437	105^{99}_{39}			102^{103}_{36}
220492184	$34^{0.8}_{0.9}$		$35^{0.95}_{0.96}$	
220555384	$30^{2.4}_{2.2}$		$29^{2.4}_{2.2}$	
220643470			4782^{542}_{467}	
220725183			$79^{1.7}_{1.9}$	
220619415			$1213^{42.35}_{42.8}$	
220601894	$905^{15.5}_{15.4}$		$1213^{42.3}_{42.8}$	
246356223	164^{19}_{16}		169^{20}_{15}	
247611242	$7^{0.11}_{0.12}$		$7^{0.11}_{0.12}$	
247452471	$34^{0.85}_{0.87}$		$36^{0.88}_{0.91}$	
220650843			$221^{2.2}_{2.3}$	
220666988	$255^{9.08}_{9.5}$		$256^{9.7}_{9.1}$	
245946030			$282^{4.03}_{4.31}$	
246070458	272^{60}_{43}		275^{58}_{44}	
212577658		436^{5}_{6}		$205^{2.5}_{2.6}$
212099230		$13^{0.24}_{0.27}$		$13^{0.26}_{0.27}$
212138198	$56^{3.66}_{3.90}$	$55^{4.05}_{3.86}$	$57^{4.21}_{3.72}$	$57^{4.25}_{4.24}$

Table 16 continued from previous page

212066407		190^{23}_{21}		200^{25}_{21}
212315941		54^{6}_{5}		49^{6}_{5}
211886472		$162^{9.46}_{8.73}$		$164^{9.37}_{9.50}$
211978865		1506^{95}_{86}		1605^{90}_{97}
211987231		350^{42}_{36}		354^{43}_{35}
211428897	$50^{0.275}_{0.275}$	$52^{0.26}_{0.28}$	$51^{0.265}_{0.275}$	$53^{0.27}_{0.28}$
211432167	$391^{6.99}_{7.14}$		$387^{7.04}_{7.32}$	
211439059	77^{26}_{16}		78^{25}_{18}	
211147528				$737^{24.55}_{24.66}$
210958990		737^{23}_{21}		800^{25}_{21}
210401157		128^{8}_{7}		123^{8}_{6}
201392505			$66^{1.60}_{1.74}$	
249258616		$201^{1.34}_{1.49}$		$201^{1.26}_{1.44}$
249344978				$81^{0.62}_{0.69}$
249559552		$86^{0.86}_{0.94}$		$87^{0.86}_{0.96}$
249447551		826^{19}_{20}		829^{20}_{19}
249401470		$122^{1.50}_{1.41}$		$122^{1.41}_{1.34}$
226040726		$111^{0.45}_{0.48}$		$112^{0.45}_{0.44}$
213951550		$49^{3.51}_{3.33}$		$50^{3.69}_{3.63}$
214611894		$319^{3.85}_{4.33}$		$323^{3.87}_{4.03}$
249644246		351^{6}_{5}		353^{6}_{5}
249624646				$110^{1.66}_{1.64}$
236344753		$157^{1.16}_{1.29}$		$164^{1.27}_{1.25}$
249173930				$207^{1.15}_{1.13}$
249928278	716^{43}_{41}		710^{46}_{40}	
248767140			$360^{3.50}_{3.56}$	
248637525	114^{14}_{13}		115^{16}_{12}	
246163416	$55^{3.36}_{3.20}$		$55^{3.05}_{3.21}$	
212661144			1314^{18}_{17}	
229039390		269^{5}_{6}		$272^{5.31}_{5.23}$
218131080		79^{10}_{9}		74^{10}_{8}
211719484	482^{33}_{30}		495^{33}_{32}	
211941472	400^{166}_{118}		398^{166}_{169}	
212303338		$8^{0.16}_{0.20}$		$9^{0.17}_{0.19}$
212534729		125^{59}_{35}		140^{69}_{36}
228741710		368^{12}_{14}		374^{12}_{13}
229002550		49^{4}_{3}		$50^{3.69}_{3.63}$

Table 16 continued from previous page

228920801				$222^{4.25}_{4.68}$
246920193			$49^{0.45}_{0.47}$	
247047370			$245^{1.33}_{1.34}$	
247002634	$15^{0.26}_{0.28}$		$16^{0.27}_{0.30}$	
247321442			375^{8}_{7}	
247384685	766^{31}_{30}		782^{32}_{29}	
249780361		315^{21}_{24}		314^{23}_{20}

Table 17: This table shows the orbital period. Here one can see the results from all filters and compare to see if they match. Note that those that have no results is due to lack of reliable angular separation value and was not given on ExoFOP at all.

Epicname	Filter 562	Filter 692	Filter 832	Filter 880
212628098				3723^{252}_{232}
201352100			567^{32}_{29}	
201390927			4763^{751}_{594}	
212703473	-	-	-	
212679181	386^{14}_{15}	449^{16}_{17}	358^{15}_{17}	$414^{18.83}_{18.98}$
214889247	$142^{5.90}_{6.51}$			$112^{5.52}_{5.90}$
213563657		17936^{1172}_{1164}		18270^{1375}_{1151}
220192485			5834^{379}_{347}	
213919915		807^{33}_{34}		803^{47}_{42}
218711655	$31^{3.24}_{2.92}$			$20^{2.60}_{2.65}$
216050437	-			
220492184	$118^{7.09}_{6.84}$		-	
220555384	140^{17}_{15}		129^{15}_{14}	
220643470			313855^{53469}_{40837}	
220725183			476^{28}_{29}	
220619415			30441^{1988}_{2137}	
220601894	-		21691^{1168}_{1114}	
246356223	1623^{254}_{214}		1671^{258}_{234}	
247611242	$15^{0.71}_{0.67}$		$18^{1.49}_{1.66}$	
247452471	129^{6}_{7}		140^{9}_{10}	
220650843			4848^{251}_{247}	
220666988	2736^{161}_{164}		2686^{186}_{180}	
245946030			3613^{175}_{189}	
246070458	2778^{804}_{571}		-	
212577658		-		2143^{113}_{107}

Table 17 continued from previous page

212099230		$37^{2.1}_{2.04}$		$37^{1.87}_{1.60}$
212138198	354^{38}_{36}	339^{38}_{32}	359^{38}_{37}	353^{38}_{35}
212066407		1728^{281}_{248}		1854^{308}_{264}
212315941		298^{45}_{42}		251^{44}_{39}
211886472		1356^{114}_{110}		1396^{119}_{126}
211978865		41858^{3699}_{3656}		46146^{4615}_{4136}
211987231		4509^{712}_{606}		4660^{780}_{661}
211428897	432^{16}_{17}	406^{16}_{17}	362^{22}_{23}	385^{24}_{26}
211432167	4629^{206}_{209}		4523^{268}_{254}	
211439059	536^{262}_{157}		552^{263}_{164}	
211147528				15325^{1075}_{1079}
210958990		14805^{794}_{736}		16730^{1146}_{1163}
210401157		-		-
201392505			465^{27}_{25}	
249258616		2577^{110}_{117}		$2476_{124}0^{121}$
249344978				782^{43}_{40}
249559552		736^{30}_{34}		684^{46}_{43}
249447551		17492^{906}_{913}		17501^{975}_{1047}
249401470		1406^{57}_{56}		1383^{68}_{65}
226040726		1445^{52}_{51}		1174^{69}_{67}
229002550		300^{35}_{31}		301^{35}_{32}
214611894		4344^{186}_{174}		4367^{234}_{220}
249644246		5216^{221}_{231}		5185^{264}_{262}
249624646				860^{43}_{44}
236344753		1540^{56}_{65}		1627^{81}_{78}
249173930				2668^{169}_{161}
249928278	13327^{1072}_{1054}		13187^{1268}_{1167}	
248767140			5628^{372}_{366}	
248637525	1001^{200}_{147}		1039^{204}_{159}	
246163416	432^{35}_{34}		380^{38}_{33}	
212661144			37817^{1741}_{2003}	
229039390		3479^{162}_{174}		3471^{300}_{178}
218131080		535^{97}_{77}		495^{93}_{76}
211719484	7110^{691}_{608}		7419^{769}_{707}	
211941472	-		-	
212303338		$17^{0.5}_{1}$		22^{2}_{1}
212534729		955^{592}_{358}		1116^{712}_{363}

Table 17 continued from previous page

228741710		5630^{333}_{348}		5724^{415}_{350}
213951550		-		-
228920801				2520^{152}_{135}
246920193			280^{14}_{12}	
247047370			3430^{204}_{202}	
247002634	52^{3}_{2}		52^{3}_{3}	
247321442			5551^{323}_{291}	
247384685	13851^{873}_{952}		13860^{944}_{989}	
249780361		4165^{427}_{389}		4143^{432}_{386}
212773309		1296^{48}_{51}		1240^{59}_{61}

Table 18: This table shows the mass of the primary, where it is easy to see the results from each filter and conclude how similar they are. In the same table there is a column with the results from aperture photometry in K-band.

Epicname	Filter 562	Filter 692	Filter 832	Filter 880	K-band
211428897	$0.45^{0.04}_{0.03}$	$0.55^{0.05}_{0.04}$	$0.54^{0.05}_{0.05}$	$0.54^{0.05}_{0.05}$	
211432167	$1.77^{0.13}_{0.13}$		$1.72^{0.20}_{0.17}$		
211439059	$0.90^{0.11}_{0.10}$		$0.91^{0.12}_{0.11}$		$0.99^{0.04}_{0.03}$
211719484	$1.42^{0.12}_{0.10}$		$1.36^{0.15}_{0.14}$		
211941472	-		-		$0.19^{0.01}_{0.01}$
212138198	$0.80^{0.06}_{0.06}$	$0.81^{0.06}_{0.06}$	$0.82^{0.08}_{0.08}$	$0.62^{0.05}_{0.04}$	
212679181	$0.50^{0.04}_{0.04}$	$0.54^{0.04}_{0.04}$	$0.60^{0.06}_{0.05}$	$0.61^{0.06}_{0.05}$	
212703473	-	-	-	-	
214889247	$1.05^{0.08}_{0.08}$			$1.08^{0.11}_{0.11}$	
216050437	-			-	
218711655	$1.22^{0.10}_{0.10}$			$1.23^{0.13}_{0.12}$	
220492184	$1.81^{0.14}_{0.13}$				
220555384	$0.70^{0.05}_{0.05}$		$0.75^{0.07}_{0.07}$		
220666988	$1.22^{0.09}_{0.09}$		$1.27^{0.14}_{0.13}$		
246070458	$1.41^{0.14}_{0.14}$				
246163416	$0.52^{0.04}_{0.04}$		$0.59^{0.06}_{0.05}$		
246356223	$0.91^{0.08}_{0.08}$		$0.92^{0.09}_{0.09}$		
247002634	$0.85^{0.07}_{0.06}$		$0.89^{0.09}_{0.08}$		
247384685	$1.22^{0.10}_{0.10}$		$1.30^{0.13}_{0.12}$		
247452471	$1.40^{0.11}_{0.10}$		$1.38^{0.17}_{0.15}$		
247611242	$0.74^{0.06}_{0.06}$		$0.66^{0.14}_{0.11}$		
248637525	$0.76^{0.07}_{0.06}$		$0.75^{0.08}_{0.07}$		

Table 18 continued from previous page

Epicname	Filter 562	Filter 692	Filter 832	Filter 880	K-band
249928278	$1.21^{0.09}_{0.09}$		$1.20^{0.14}_{0.13}$		
210958990		$1.10^{0.09}_{0.07}$		$1.09^{0.14}_{0.11}$	$0.85^{0.07}_{0.06}$
211886472		$1.53^{0.12}_{0.12}$		$1.47^{0.15}_{0.15}$	$0.22^{0.01}_{0.01}$
211978865		$1.25^{0.09}_{0.09}$		$1.20^{0.13}_{0.12}$	$0.23^{0.02}_{0.02}$
211987231		$1.20^{0.11}_{0.10}$		$1.18^{0.14}_{0.12}$	$0.71^{0.05}_{0.06}$
212066407		$1.60^{0.15}_{0.14}$		$1.56^{0.18}_{0.17}$	$0.58^{0.05}_{0.04}$
212099230		$0.99^{0.07}_{0.07}$		$0.98^{0.10}_{0.09}$	
212303338		$0.93^{0.08}_{0.07}$		$0.92^{0.09}_{0.08}$	
212315941		$1.00^{0.09}_{0.09}$		$1.00^{0.11}_{0.10}$	
220619415			$1.26^{0.13}_{0.13}$		
212534729		$1.21^{0.22}_{0.17}$		$1.23^{0.23}_{0.19}$	
212577658		$1.03^{0.07}_{0.08}$		$0.99^{0.10}_{0.10}$	
212773309		$0.84^{0.07}_{0.06}$		$0.85^{0.09}_{0.08}$	
213563657		$1.06^{0.08}_{0.08}$		$1.06^{0.11}_{0.11}$	
213919915		$1.05^{0.08}_{0.08}$		$1.07^{0.11}_{0.11}$	
214611894		$1.06^{0.08}_{0.08}$		$1.07^{0.10}_{0.10}$	
218131080		$1.02^{0.10}_{0.09}$		$0.98^{0.11}_{0.10}$	
226040726		$0.66^{0.05}_{0.05}$		$0.70^{0.06}_{0.06}$	
228741710		$0.85^{0.07}_{0.06}$		$0.85^{0.08}_{0.08}$	
229002550		$0.78^{0.06}_{0.06}$		$0.80^{0.07}_{0.07}$	
229039390		$1.08^{0.09}_{0.08}$		$1.05^{0.11}_{0.10}$	
236344753		$0.89^{0.06}_{0.07}$		$0.90^{0.08}_{0.09}$	
249258616		$0.76^{0.06}_{0.06}$		$0.78^{0.07}_{0.08}$	
249401470		$1.01^{0.08}_{0.08}$		$1.01^{0.10}_{0.10}$	
249447551		$0.99^{0.08}_{0.07}$		$0.99^{0.10}_{0.09}$	
249559552		$0.82^{0.07}_{0.06}$		$0.83^{0.08}_{0.07}$	
249644246		$0.84^{0.06}_{0.06}$		$0.86^{0.08}_{0.08}$	
249780361		$1.13^{0.09}_{0.09}$		$1.12^{0.11}_{0.11}$	
201352100			$0.80^{0.08}_{0.08}$		$0.73^{0.05}_{0.05}$
201390927			$0.80^{0.08}_{0.08}$		
201392505			$0.83^{0.08}_{0.08}$		
212619190			-		$0.75^{0.12}_{0.11}$
212661144			$0.95^{0.10}_{0.09}$		
220192485			$0.89^{0.08}_{0.08}$		
220601894		$1.00^{0.08}_{0.10}$			
220643470			-		

Table 18 continued from previous page

Epicname	Filter 562	Filter 692	Filter 832	Filter 880	K-band
220650843			$1.21^{0.12}_{0.13}$		
220725183			$1.34^{0.12}_{0.14}$		
245946030			$1.16^{0.12}_{0.12}$		$0.86^{0.08}_{0.07}$
246920193			$0.97^{0.10}_{0.09}$		
247047370			$0.91^{0.09}_{0.08}$		
247321442			$1.14^{0.12}_{0.12}$		
248767140			$0.94^{0.09}_{0.09}$		
211147528				$1.35^{0.14}_{0.14}$	$0.57^{0.04}_{0.04}$
212628098				$0.81^{0.07}_{0.07}$	$0.93^{0.16}_{0.14}$
228920801				$1.13^{0.12}_{0.11}$	
249173930				$0.76^{0.08}_{0.07}$	
249344978				$0.61^{0.06}_{0.05}$	
249624646				$1.25^{0.13}_{0.13}$	

Table 19: This table shows the mass of the secondary, where it is easy to see the results from each filter used in speckle imaging and the aperture photometry results in K-band, to conclude how similar they are.

Epicname	Filter 562	Filter 692	Filter 832	Filter 880	K-band
211428897	$0.23^{0.05}_{0.05}$	$0.28^{0.03}_{0.02}$	$0.48^{0.09}_{0.09}$	$0.49^{0.09}_{0.09}$	$0.85^{0.07}_{0.07}$
211432167	$1.02^{0.08}_{0.08}$		$1.09^{0.13}_{0.10}$		
211439059	$0.72^{0.09}_{0.08}$		$0.77^{0.10}_{0.09}$		$0.93^{0.03}_{0.03}$
211719484	$0.77^{0.07}_{0.06}$		$0.81^{0.09}_{0.08}$		
211941472	-		$0.99^{0.20}_{0.18}$		$0.17^{0.01}_{0.01}$
212138198	$0.56^{0.05}_{0.04}$	$0.61^{0.05}_{0.05}$	$0.61^{0.06}_{0.05}$	$0.65^{0.06}_{0.06}$	$0.50^{0.04}_{0.04}$
212679181	$0.43^{0.04}_{0.03}$	$0.46^{0.04}_{0.04}$	$0.55^{0.05}_{0.05}$	$0.53^{0.05}_{0.05}$	
212703473	-	-	-	-	
214889247	$0.32^{0.04}_{0.04}$			$0.56^{0.06}_{0.05}$	
216050437	-			-	
218711655	$1.02^{0.09}_{0.08}$			$0.96^{0.10}_{0.09}$	$0.93^{0.08}_{0.07}$
220492184	$0.98^{0.09}_{0.09}$				
220555384	$0.64^{0.05}_{0.05}$		$0.72^{0.07}_{0.07}$		
220666988	$1.00^{0.08}_{0.07}$		$1.11^{0.11}_{0.11}$		
246070458	$1.21^{0.13}_{0.11}$				
246163416	$0.39^{0.04}_{0.04}$		$0.53^{0.05}_{0.04}$		
246356223	$0.83^{0.07}_{0.07}$		$0.85^{0.07}_{0.09}$		
247002634	$0.56^{0.08}_{0.07}$		$0.62^{0.06}_{0.06}$		

Table 19 continued from previous page

Epicname	Filter 562	Filter 692	Filter 832	Filter 880	K-band
247384685	$1.15^{0.09}_{0.09}$		$1.21^{0.12}_{0.11}$		
247452471	$1.01^{0.08}_{0.07}$		$0.99^{0.11}_{0.10}$		
247611242	$0.59^{0.05}_{0.04}$		$0.53^{0.09}_{0.07}$		
248637525	$0.69^{0.06}_{0.06}$		$0.68^{0.07}_{0.06}$		
249928278	$0.87^{0.07}_{0.07}$		$0.89^{0.10}_{0.09}$		
210958990		$0.72^{0.06}_{0.05}$		$0.75^{0.08}_{0.07}$	$0.56^{0.04}_{0.04}$
211886472		$0.77^{0.06}_{0.06}$		$0.78^{0.08}_{0.08}$	$0.22^{0.01}_{0.01}$
211978865		$0.72^{0.06}_{0.06}$		$0.72^{0.07}_{0.07}$	$0.15^{0.01}_{0.01}$
211987231		$0.91^{0.08}_{0.08}$		$0.92^{0.10}_{0.09}$	$0.58^{0.04}_{0.04}$
212066407		$0.67^{0.06}_{0.06}$		$0.78^{0.09}_{0.08}$	$0.58^{0.05}_{0.04}$
212099230		$0.57^{0.04}_{0.04}$		$0.62^{0.06}_{0.06}$	
212303338		$0.65^{0.05}_{0.05}$		$0.68^{0.06}_{0.06}$	
212315941		$0.84^{0.07}_{0.07}$		$0.82^{0.09}_{0.08}$	
220619415			$0.69^{0.07}_{0.07}$		
212534729		$1.08^{0.19}_{0.15}$		$1.00^{0.18}_{0.15}$	
212577658		$0.71^{0.05}_{0.06}$		$0.86^{0.08}_{0.08}$	$0.97^{0.19}_{0.14}$
212773309		$0.57^{0.05}_{0.04}$		$0.64^{0.07}_{0.05}$	
213563657		$0.74^{0.06}_{0.06}$		$0.65^{0.06}_{0.07}$	
213919915		$0.90^{0.07}_{0.06}$		$0.91^{0.09}_{0.09}$	
214611894		$0.67^{0.05}_{0.05}$		$0.72^{0.06}_{0.06}$	$0.90^{0.07}_{0.07}$
218131080		$0.70^{0.06}_{0.06}$		$0.67^{0.07}_{0.07}$	
226040726		-		$0.31^{0.07}_{0.05}$	
228741710		$0.74^{0.06}_{0.06}$		$0.75^{0.07}_{0.07}$	
229002550		$0.51^{0.04}_{0.04}$		$0.59^{0.05}_{0.05}$	
229039390		$0.53^{0.05}_{0.04}$		$0.60^{0.06}_{0.05}$	
236344753		$0.75^{0.05}_{0.06}$		$0.78^{0.07}_{0.07}$	
249258616		$0.46^{0.07}_{0.06}$		$0.54^{0.05}_{0.05}$	
249401470		$0.57^{0.05}_{0.04}$		$0.64^{0.06}_{0.06}$	
249447551		$0.84^{0.07}_{0.06}$		$0.85^{0.09}_{0.08}$	
249559552		$0.36^{0.05}_{0.05}$		$0.55^{0.11}_{0.10}$	
249644246		$0.77^{0.06}_{0.05}$		$0.78^{0.08}_{0.07}$	
249780361		$0.66^{0.06}_{0.06}$		$0.70^{0.07}_{0.07}$	
201352100			$0.52^{0.05}_{0.05}$		$0.31^{0.03}_{0.02}$
201390927			$0.68^{0.07}_{0.06}$		
201392505			$0.51^{0.05}_{0.05}$		
212619190			-		$0.75^{0.12}_{0.11}$

Table 19 continued from previous page

Epicname	Filter 562	Filter 692	Filter 832	Filter 880	K-band
212661144			$0.64^{0.06}_{0.06}$		
220192485			$0.53^{0.10}_{0.10}$		
220601894		$0.57^{0.05}_{0.06}$			
220643470			$1.11^{0.13}_{0.12}$		
220650843			$0.89^{0.10}_{0.09}$		
220725183			$0.81^{0.07}_{0.08}$		
245946030			$0.59^{0.06}_{0.06}$		$0.26^{0.03}_{0.03}$
246920193			$0.54^{0.05}_{0.05}$		
247047370			$0.34^{0.07}_{0.06}$		
247321442			$0.57^{0.06}_{0.05}$		
248767140			$0.55^{0.12}_{0.10}$		
211147528				$0.37^{0.08}_{0.07}$	$0.56^{0.04}_{0.04}$
212628098				$0.56^{0.12}_{0.10}$	$0.71^{0.12}_{0.11}$
228920801				$0.57^{0.06}_{0.05}$	
249173930				$0.48^{0.10}_{0.08}$	
249344978				$0.27^{0.05}_{0.05}$	
249624646				$0.56^{0.06}_{0.05}$	

Table 20: This table shows the mass ratio, where it is easy to see the results from each filter used in speckle imaging. The results from the performed aperture photometry are also included, in order to compare all the filters side by side.

Epicname	Filter 562	Filter 692	Filter 832	Filter 880	K-band
211428897	$0.52^{0.03}_{0.03}$	$0.51^{0.03}_{0.03}$	$0.90^{0.11}_{0.11}$	$0.90^{0.11}_{0.11}$	
211432167	$0.58^{0.01}_{0.02}$		$0.63^{0.02}_{0.02}$		
211439059	$0.80^{0.02}_{0.02}$		$0.85^{0.02}_{0.02}$		$0.92^{0.00}_{0.00}$
211719484	$0.54^{0.02}_{0.02}$		$0.60^{0.02}_{0.02}$		
211941472	0.00		0.00		$0.91^{0.01}_{0.01}$
212138198	$0.70^{0.01}_{0.01}$	$0.75^{0.01}_{0.01}$	$0.75^{0.02}_{0.02}$	$0.80^{0.02}_{0.02}$	$0.80^{0.01}_{0.01}$
212679181	$0.85^{0.04}_{0.04}$	$0.86^{0.04}_{0.04}$	$0.93^{0.02}_{0.02}$	$0.87^{0.02}_{0.02}$	
212703473	-	-	-	-	
214889247	$0.30^{0.04}_{0.03}$			$0.52^{0.02}_{0.02}$	
216050437	-			-	
218711655	$0.84^{0.02}_{0.02}$			$0.78^{0.02}_{0.02}$	
220492184	$0.54^{0.03}_{0.03}$				
220555384	$0.93^{0.02}_{0.02}$		$0.97^{0.02}_{0.02}$		
220666988	$0.82^{0.02}_{0.02}$		$0.87^{0.02}_{0.02}$		

Table 20 continued from previous page

Epicname	Filter 562	Filter 692	Filter 832	Filter 880	K-band
246070458	$0.86^{0.02}_{0.02}$				
246163416	$0.75^{0.04}_{0.05}$		$0.90^{0.02}_{0.02}$		
246356223	$0.91^{0.02}_{0.02}$		$0.92^{0.02}_{0.02}$		
247002634	$0.66^{0.08}_{0.07}$		$0.70^{0.02}_{0.02}$		
247384685	$0.94^{0.02}_{0.02}$		$0.93^{0.03}_{0.03}$		
247452471	$0.72^{0.02}_{0.02}$		$0.72^{0.02}_{0.02}$		
247611242	$0.79^{0.01}_{0.02}$		$0.80^{0.02}_{0.02}$		
248637525	$0.90^{0.02}_{0.02}$		$0.91^{0.02}_{0.02}$		
249928278	$0.72^{0.02}_{0.02}$		$0.74^{0.02}_{0.02}$		
210958990		$0.65^{0.01}_{0.02}$		$0.69^{0.02}_{0.02}$	$0.66^{0.01}_{0.01}$
211886472		$0.51^{0.02}_{0.02}$		$0.53^{0.02}_{0.03}$	$1.00^{0.01}_{0.01}$
211978865		$0.58^{0.02}_{0.02}$		$0.60^{0.03}_{0.03}$	$0.66^{0.01}_{0.01}$
211987231		$0.76^{0.02}_{0.02}$		$0.78^{0.02}_{0.02}$	$0.82^{0.00}_{0.00}$
212066407		$0.42^{0.02}_{0.02}$		$0.50^{0.03}_{0.03}$	$1.00^{0.01}_{0.01}$
212099230		$0.57^{0.02}_{0.02}$		$0.63^{0.02}_{0.02}$	
212303338		$0.70^{0.01}_{0.01}$		$0.75^{0.02}_{0.02}$	
212315941		$0.84^{0.02}_{0.02}$		$0.82^{0.02}_{0.02}$	
220619415			$0.55^{0.02}_{0.02}$		
212534729		$0.90^{0.02}_{0.02}$		$0.81^{0.02}_{0.02}$	
212577658		$0.69^{0.02}_{0.02}$		$0.87^{0.02}_{0.02}$	
212773309		$0.68^{0.01}_{0.01}$		$0.75^{0.02}_{0.02}$	
213563657		$0.70^{0.02}_{0.02}$		$0.61^{0.02}_{0.02}$	
213919915		$0.87^{0.02}_{0.02}$		$0.85^{0.02}_{0.02}$	
214611894		$0.63^{0.02}_{0.02}$		$0.66^{0.02}_{0.02}$	
218131080		$0.69^{0.02}_{0.02}$		$0.68^{0.02}_{0.02}$	
226040726		-		$0.44^{0.07}_{0.06}$	
228741710		$0.87^{0.02}_{0.02}$		$0.88^{0.02}_{0.02}$	
229002550		$0.65^{0.01}_{0.02}$		$0.74^{0.02}_{0.02}$	
229039390		$0.49^{0.02}_{0.02}$		$0.57^{0.02}_{0.02}$	
236344753		$0.84^{0.02}_{0.02}$		$0.87^{0.02}_{0.02}$	
249258616		$0.60^{0.07}_{0.06}$		$0.70^{0.02}_{0.02}$	
249401470		$0.56^{0.02}_{0.02}$		$0.63^{0.02}_{0.02}$	
249447551		$0.84^{0.02}_{0.02}$		$0.86^{0.02}_{0.02}$	
249559552		$0.45^{0.05}_{0.05}$		$0.66^{0.10}_{0.09}$	
249644246		$0.91^{0.02}_{0.02}$		$0.90^{0.02}_{0.02}$	
249780361		$0.58^{0.03}_{0.02}$		$0.62^{0.02}_{0.02}$	

Table 20 continued from previous page

Epicname	Filter 562	Filter 692	Filter 832	Filter 880	K-band
201352100			$0.65^{0.02}_{0.02}$		$0.43^{0.01}_{0.01}$
201390927			$0.85^{0.02}_{0.02}$		
201392505			$0.62^{0.02}_{0.02}$		
212619190			-		$1.00^{0.00}_{0.00}$
212661144			$0.67^{0.02}_{0.02}$		
220192485			$0.59^{0.08}_{0.08}$		
220601894		$0.57^{0.02}_{0.02}$			
220643470			-		
220650843			$0.78^{0.02}_{0.02}$		
220725183			$0.61^{0.02}_{0.02}$		
245946030			$0.51^{0.02}_{0.02}$		$0.30^{0.02}_{0.02}$
246920193			$0.56^{0.02}_{0.02}$		
247047370			$0.37^{0.05}_{0.05}$		
247321442			$0.50^{0.02}_{0.02}$		
248767140			$0.59^{0.08}_{0.08}$		
211147528				$0.28^{0.04}_{0.04}$	$1.00^{0.00}_{0.00}$
212628098				$0.69^{0.10}_{0.09}$	$0.76^{0.00}_{0.00}$
228920801				$0.50^{0.02}_{0.02}$	
249173930				$0.63^{0.09}_{0.09}$	
249344978				$0.45^{0.07}_{0.07}$	
249624646				$0.45^{0.02}_{0.02}$	